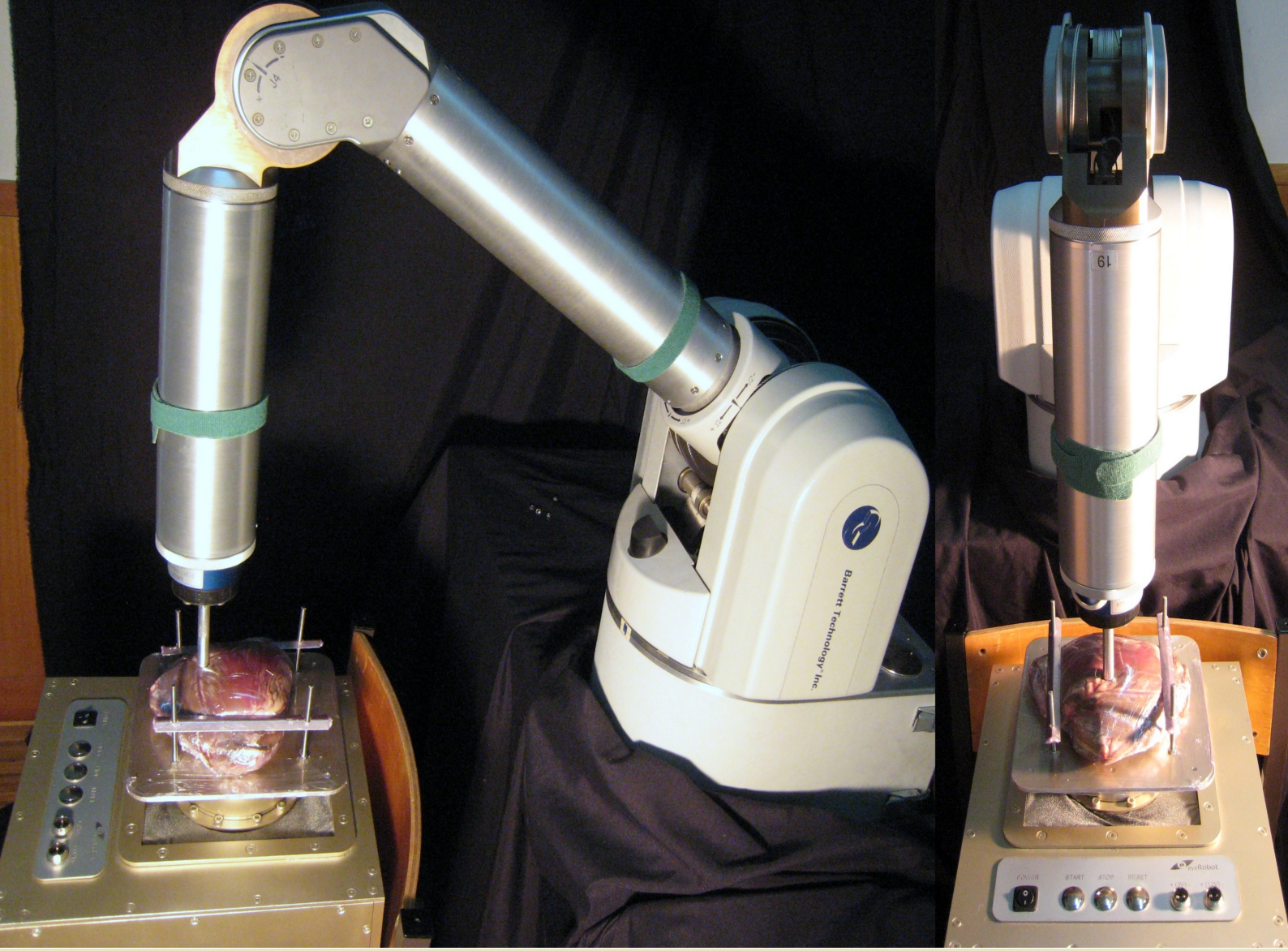

Michel Olivier Dominici

CONTROL ARCHITECTURES FOR ROBOTIC ASSISTANCE IN BEATING HEART SURGERY

Tese de doutoramento em Engenharia Electrotécnica e de Computadores, Ramo de Especialização em Automação e Robótica, orientada pelo Senhor Professor Doutor Rui Pedro Duarte Cortesão e apresentada ao Departamento de Engenharia Electrotécnica e de Computadores da Faculdade de Ciências e Tecnologia da Universidade de Coimbra

Fevereiro de 2016

· U C ·

Universidade de Coimbra

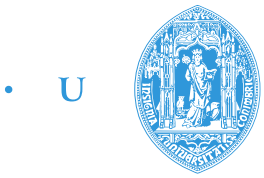

University of Coimbra

Control Architectures for Robotic Assistance in Beating Heart Surgery

Ph.D. Thesis

Michel Olivier Dominici

Fevereiro 2016

Advisor: Prof. Rui Pedro Duarte Cortesão, University of Coimbra

Control Architectures for Robotic Assistance in Beating Heart Surgery

Michel Olivier Dominici

Fevereiro 2016

Abstract

Cardiovascular diseases are the first cause of mortality in the world. More than 17 million people die every year, representing 29% of all global deaths. Among these, coronary heart diseases are the most critical ones, reaching up to 7.2 million deaths. To reduce the risk of death the coronary artery bypass grafting (CABG) is the most common surgical intervention. Currently, the procedure involves a median sternotomy, an incision in the thorax allowing a direct access to the heart, and a cardiopulmonary bypass (CPB), where heart and lung functionalities are performed by an extracorporeal machine. Unfortunately the heart-lung machine is the greatest source of complications and post-operatory mortality for patients. Problems involved have motivated beating heart surgery that circumvent CPB procedure. Heartbeats and respiration represent the two main sources of disturbances during off-pump surgery. Mechanical stabilizers have been conceived for locally decreasing the heart motion. Placed around a region of interest (e.g., coronary artery), these stabilizers constrain the motion by suction or pressure. Despite many improvements done over the years, considerable residual motions still remain and the surgeon has to manually compensate them. Robotic assistance has the potential to offer significant improvements to the medical practice in terms of precision, safety and comfort. The *da Vinci* surgical system is the most popular and sophisticated. Although it has considerably improved dexterity, precision and safety, no solution for restoring tactile feedback to the surgeon exists and physiological motions still need to be manually canceled by the surgeon.

The work presented in this thesis focus on robotic assistance for beating heart surgery. Based on force feedback, we designed new control architectures providing an autonomous physiological motion compensation functionality. Experimental assessments have been performed through a realistic scenario. A Heartbox robot equipped with an *ex vivo* heart reproduces the heart motion and a robot arm generates desired surgical forces on the moving heart. Interaction forces provide the haptic feedback for the surgeon. Merging autonomous motion compensation techniques with force control and haptic feedback is a major scientific challenge that we tackle in this work.

Resumo

Doenças cardiovasculares são a primeira causa de morte no mundo. Todos os anos mais de 17 milhões de pessoas morrem, representando 29% do número total de mortes. As doenças coronárias são as mais críticas, atingindo mais de 7.2 milhões de mortes. Para reduzir o risco de morte, o "bypass" coronário é a intervenção cirúrgica mais comum. Atualmente este procedimento envolve uma esternotomia mediana e um "bypass" cardiopulmonar, permitindo que uma máquina externa implemente as funções de oxigenação e bombeamento de sangue. Contudo, esta máquina externa é fonte de muitas complicações pós-operatórias, incluindo a morte de pacientes. Estes problemas motivam o estudo e desenvolvimento de técnicas cirúrgicas sem parar o funcionamento do coração. Nestes casos, os batimentos cardíacos e a respiração representam as principais fontes de perturbação. Foram desenvolvidos estabilizadores mecânicos para diminuir localmente o movimento cardíaco. Colocado numa região de específica (por exemplo, na artéria coronária), estes estabilizadores limitam o movimento por pressão e sucção. Apesar dos melhoramentos feitos ao longo dos anos, ainda existe um movimento residual considerável, e o cirurgião tem que os compensar manualmente. Torna-se então natural incluir dispositivos robóticos para ajudar na prática médica, melhorando a precisão, segurançae conforto de tarefas cirúrgicas. O sistema cirúrgico *da Vinci* é atualmente o sistema robótico mais avançado para a prática médica, com elevado desempenho em tarefas de destreza, precisão e segurança, apesar de não fornecer soluções de realimentação táctil, nem de compensação automática de movimentos fisiológicos. O trabalho desta tese é na área da robótica para cirurgias cardíacas com o coração a bater. Baseada na realimentação da força, esta tese explora novas arquiteturas de controlo com compensação automática dos movimentos cardíacos. São feitos testes experimentais em cenários muito realistas, sem utilizar seres vivos. Um robô denominado "Heartbox" equipado com um coração real reproduz movimentos cardíacos, enquanto que outro robô manipulador aplica forças cirúrgicas nesse coração com batimento artificial. As forças de interação fornecem realimentação de contacto ao cirurgião. O principal desafio científico deste trabalho é a ligação de técnicas de compensação autónoma de movimentos fisiológicos com

controlo de força e realimentação haptica.

Je dédicace cette thèse à mon père et ma mère qui m'ont toujours soutenu, même dans les periodes les plus difficiles de ma vie.
Ces périodes que j'aimerai oublier mais qui resteront à jamais gravées dans ma mémoire.
Merci à vous deux, je vous aime :-)

Remerciements

Je remercie, en tous premier lieu, Rui Pedro Duarte Cortesão pour la confiance qu'il m'a accordée en me permettant de venir faire cette thèse au Portugal ; mais aussi pour son soutient et les conseils avisés tant au niveau professionnel qu'au niveau personnel. Sa bonne humeur permanente et son optimisme à toute épreuve en font une personne extraordinaire avec qui travailler. «Merci Rui de m'avoir donné cette opportunité, merci du fond du cœur.»

Ability is nothing without opportunity

Napoleon Bonaparte

Je remercie ensuite Cristóvão Jorge Silva Duarte Sousa qui m'a accueilli chez lui et énorment aidé, non seulement pendant les premiers mois de ma vie étudiante portugaise mais aussi durant ces quatre années, pour remplir quantité de documents et effectuer nombre de démarches administratives. «Merci Cristóvão sans toi je serai encore perdu dans ce labyrinthe qu'est l'administration.» :-)

Fernanda, Luis et encore Cristóvão mes compagnons de galère. Toujours là pour rendre nos longues heures au labo plus agréables, merci à vous. «Luis, ça y est je suis rentré mais ne t'inquiète pas je repars dans 10 jours !» ;-)

Pour vous mes potos, les grumeaux en tête, suivi de près par Patou, Damien, Yoyo et JPeg : «Hé oui ça y est les gars elle est finie ! \o/ Qui en a douté, hein ? Merci à vous d'y avoir cru pendant toutes ces années, merci pour vos blagues pourries, vos interrogations sur l'utilité de continuer. Voilà sans vous je l'aurais jamais fini >< ... ou pas en fait» :-)

En limant on fait d'une poutre une aiguille.

Unknown

Nico le p'tit frère : dire que maintenant on est vraiment de la même famille :-). Merci pour le dépaysement et le changement d'air apportés lors de ces semaines à travailler avec toi sur nos/tes chantiers, bien que fatiguant physiquement ça a été ressourçant. «Allez Nico, sur la façade, on les ouvre ces fenêtres !»

Gros biensûr, l'ami à 17000 [km] qui vient pour mon mariage avec sa femme et s'occupe de tout, si c'est pas une preuve d'amour ça ! «Pourquoi t'es si loin, poto !»

Une profonde et triste pensée pour une personne que j'ai perdu durant la dernière année. Une personne avec qui j'aurais aimé fêter ça et bien d'autre choses. «Tu m'as manques Mélouille.» :'(

Joan, Le Grand Frère ! Saïda La Grande Sœur ! Bien que différents toujours bienveillants. Vous serez toujours dans mon cœur. «Je vous aime !» :-)

Avant la fin, je remercie Moa. Hé oui quand même c'est Moa qui ai finalement réussi cet exploit. Malgré un choix plus que discutable il y a 5 ans, j'ai percévéré dans cette décision , bravé les difficultés qui se sont présentées et finalement remporté cette bataille. Après ce que j'en ferai, bah on verra ça dans le prochain épisode.

A force de taper sur le clou, on finit par l'enfoncer.

Unknown

Et biensûr on garde toujours la meilleure pour la fin : Camille ma femme qui ne l'est devenue que récement d'ailleur. Je te remercie d'avoir rendu mes journées plus douces et bien plus agréables à vivre. Presque tout les jours je me rends compte de la chance que j'ai de t'avoir près de moi. Et particulièrement ces dernières semaines avec Petinou dans ton ventre. «Viens vite, on t'attends !» <3

Deux années riches en évènement : mariage, doctorat et Petinou !

Moa

Dominici-Verdier Michel Olivier
Février 2016

Acknowledgements

This work was supported in part by the Portuguese Science and Technology Foundation project PTDC/EEA-CRO/110008/2009 (grant number SFRH/BD/74278/2010).
This work was also supported by project "A Surgery and Diagnosis Assisted by Computer Using Images" (SCT/2011/02/027/4824) funded by the QREN programme "Mais Centro" with financing from FEDER.

Contents

List of Figures

List of Tables

Chapter 1

Introduction

Contents

Now this is not the end. It is not even the beginning of the end. But it is, perhaps, the end of the beginning.

Winston Churchill

Cardiovascular diseases (CVD) are the first cause of mortality in the world. More than 17 million people die every year, representing 30% of all global deaths. Among these, coronary heart diseases (CHD) are the most critical ones, reaching up to 7.4 million deaths. In European Union CVD causes over 1.9 million deaths each year, representing 40% of all deaths and CHD is the single most common cause of death, accounting for over $681,000$ deaths each year [WHO, 2009]. Coronary artery bypass grafting (CABG) is the most common surgical intervention on the heart to reduce the risk of death.

This chapter will give a brief overview of the classical surgical procedure and recent developments are briefly exposed. Potential benefits of robotic assistance for providing surgeons with superior visualization, enhanced dexterity, precise movements and ergonomic comfort are discussed. Finally, an overview of the current technical challenges in the field of robotized cardiac surgery is presented.

1.1 Motivation

In European Union, the coronary artery bypass grafting is one of the most common type of heart surgical intervention for adult patients. It is a mature technique, with a considerable number of related studies and statistics [Eagle and Guyton, 2004]. Basically, the procedure consists in bypassing an occlusion point on the coronary artery for reestablishing irrigation (see Fig. 1.1). Grafts may be taken from the saphenous vein or the internal mammary artery [Naik et al., 2003]. Currently, the reference CABG procedure involves a median sternotomy, a $16 - 20$ [cm] incision in the thorax allowing a direct access to the heart (see Fig. 1.2(a)), and a cardiopulmonary bypass (CPB), where heart and lung functionalities are performed by an extracorporeal machine.

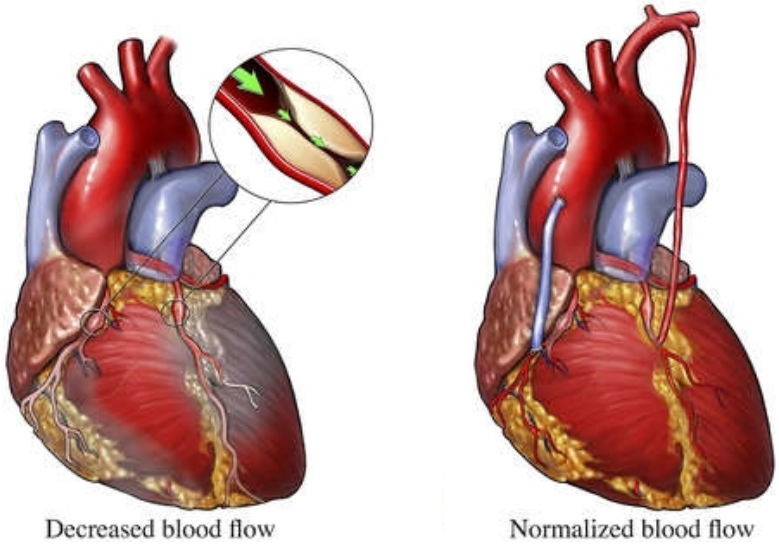

Figure 1.1: Coronary artery bypass grafting. Two grafts have been used for bypassing occluded arteries and reestablishing blood irrigation (source: www.images.com).

Although a direct access to the heart through a sternotomy privileges the surgeon's dexterity and quick access to the target intervention area, open-chest surgery presents serious downsides to the patient: significant trauma and infection risks due to the long duration of the procedure [Newman et al., 1991], [Klesius et al., 2004]. Whenever possible, less invasive solutions such as a mini-thoracotomy ($8 - 10$ [cm] incision between the ribs) are adopted (see Fig. 1.2(b)), but they are limited to procedures on the frontal side of the heart.

CPB is performed due mostly to the difficulty or impossibility of operating on the beating heart. Blood circulation and oxygenation are maintained by means of an extracorporeal circulation machine (also known as the heart-lung machine). This procedure is the greatest source of complications and post-operatory mortality for patients. Problems such as inflammatory blood response to the heart-lung machine, the risk of microemboli, kidney dysfunctions and neurological complications such as stroke during the clamping of the aorta have motivated new solutions that circumvent the use of extracorporeal circulation [Eagle and Guyton, 2004].

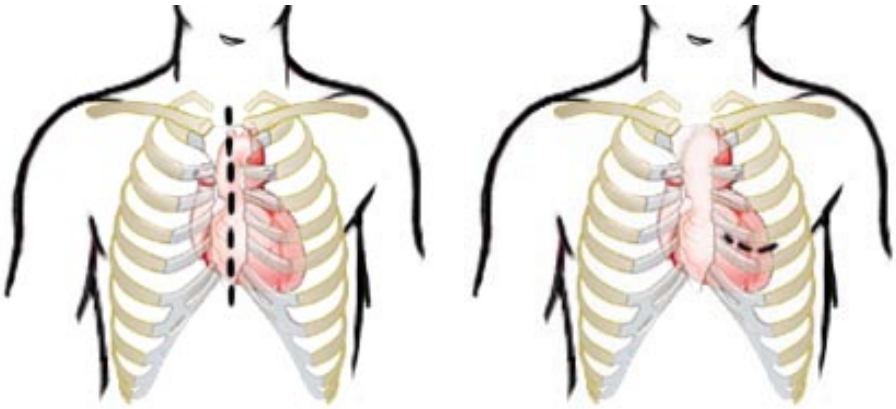

(a) (b)

Figure 1.2: Median sternotomy and mini-thoracotomy. The dashed line indicates the incision performed for a median sternotomy (a) and a mini-thoracotomy (b) (source: http://my.clevelandclinic.org/).

1.2 Problem definition

Even though open-chest on-pump cardiac surgery is the standard for CABG procedures and high success rates are observed nowadays, the downsides of the extracorporeal circulation are not negligible. Since the CPB is performed mostly due to the difficulty of operating on a moving organ, passive mechanical stabilizers have been conceived for locally decreasing the heart motion, allowing direct surgical procedures on the beating heart (see Fig. 1.3). Placed around a region of interest (e.g., coronary artery, see Fig.1.3(c)), these stabilizers constrain the motion by suction or pressure. Statistical studies reveal a slighter decrease in the complications rate with respect to the on-pump scenario, suggesting fewer neurological complications [Patel et al., 2002], smaller risk of myocardial infarction [Berdat et al., 2004], less convalescence time and less costs [Boyd et al., 1999]. For instance, off-pump CABG procedures have a death and/or complication risk of about 1% to 2% in a low-risk patient [Shekar, 2006]. Although many improvements have been done over the years, performance studies of such stabilizers reveal a considerable residual heart motion due to insufficient immobilization, which ranges from $1 - 1.5$ [mm] approximately [Lemma et al., 2005]. This is due specially to the greater flexibility of the narrow tools and the greater distance between mounting point and worksite [Riviere et al., 2006]. Another fact that must be taken into consideration is the physical impact of mechanical stabilizers. The intense pressure or vacuum pressure necessary to cancel out the heart motion may inflict severe tissue damage. Finally, interventions on the posterior part of the heart remain problematic, since the heart in these cases is considerably constrained while stabilized, reducing blood pressure which may cause epicardial damage [Dzwonczyk et al., 2005].

(a) (b) (c)

Figure 1.3: Passive mechanical heart stabilizers. The Octopus heart stabilizer based on suction (a) (source: www.medtronic.com). Solutions proposed by Guidant based on suction (b) and pressure (c) (source: www.bostonscientific.com).

1.3 Objectives

In the abdomen and thorax the respiration yields large cyclic displacements of several organs. At the same time the heartbeat motion involves high acceleration displacements. The sum of these two motions involves important disturbances for a surgeon performing a surgical task on the heart. Especially for surgical procedures requiring good precision (*e.g.*, needle insertion, suturing). Indeed, the gesture accuracy strongly depends on his/her ability to compensate these motions. Manual tracking of the complex heartbeat motion cannot be achieved by a human without phase and amplitude errors [Falk, 2002] and [Jacobs et al., 2003].

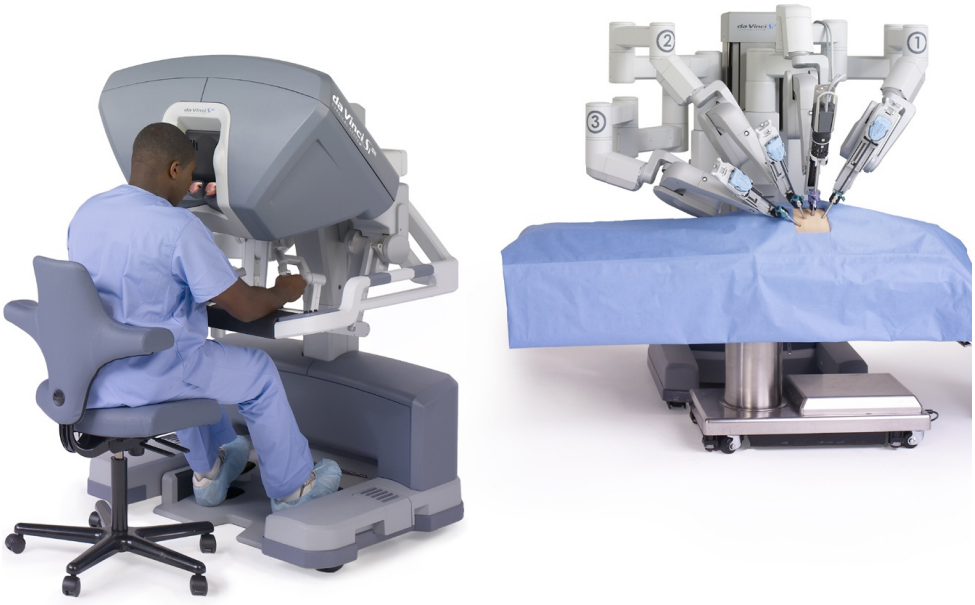

Figure 1.4: The *da Vinci* surgical platform from Intuitive Surgical Inc.. A master console transmits the surgeon's gestures to the slave platform composed of robotic surgical tools and endoscope arms (source: www.intuitivesurgical.com).

Robotic assistance has the potential to offer significant improvements to the medical practice in terms of precision, safety and comfort. The *da Vinci* surgical system, from Intuitive Surgical Inc., is nowadays the most popular and sophisticated teleoperated surgical platform. A master console transmits the surgeon's gestures to the slave platform, which is the robot that holds the surgical tools and endoscope. Such platforms provide surgeons with superior visualization, enhanced dexterity, precise movements and ergonomic comfort, making it possible for complex surgical procedures to be performed in a minimally invasive fashion (Fig. 1.4). Although the *da Vinci* surgical platform has considerably

improved the ergonomics and mobility issues related to the minimally invasive procedure, no solution for restoring tactile feedback to the surgeon exists and physiological motions still need to be manually compensate by the surgeon. Miniature versions of mechanical stabilizers are available for performing off-pump interventions but the residual motion due to insufficient immobilization is still important. Statistics presented in [Kappert et al., 2001] show that 3% of surgeries using the *da Vinci* robot and mechanical stabilization are converted in a median sternotomy and 33% are converted in a mini-thoracotomy. This is due specially to the difficulty of performing delicate tasks such as suturing in the presence of physiological motions.

Through sensory data (e.g., vision and/or force), providing tactile feedback and active motion compensation should enhance surgical dexterity and precision leading to make the surgical act more intuitive for surgeons. The work presented in this thesis focuses on these improvements to strengthen robotic assistance in beating heart surgeries. The main goal is to develop a force control architecture which is able to compensate 3D disturbances due to cardiac and breathing motions, while tracking time varying surgical force references. The challenge is to use no *a priori* information about these disturbances, relying the control actions on measured forces and on a generic/ simple contact model. To accomplish this, four control architectures based on model predictive control (MPC) and active observer (AOB) techniques are investigated. An experimental platform is used to assess each controller. It is composed of two robots. An Heartbox robot equipped with an *ex vivo* heart reproducing the heart motion and a WAM robot arm (tool holder) generating desired surgical forces on the moving heart. The Heartbox robot motion generates force disturbances on the tool holder robot, which should be compensated by the control architecture. Therefore, the goal is to achieve high quality beating heart motion compensation based on force feedback, without knowing in advance the cardiac motion, guaranteeing also surgical force tracking with high performance.

1.4 Contributions

The major contributions of this work are:

- Two new control architectures, based on MPC and AOB techniques, have been developed to cope with 3D heart motion compensation without *a priori* information on heart motion data.
- High quality 3D surgical force tracking in the presence of heart motion.
- High quality 3D heart motion compensation without knowing in advance heart motion and contact stiffness.
- Controllers are robust to stiffness mismatches and performances are similar for a stiffness range within the surgical environment.
- Experimental results outperform what has been done in this area, even in the presence of stiffness mismatches.

1.5 Thesis structure

This thesis is organized as follows:

- the next chapter analyzes robotic approaches which propose a solution for motion compensations. Solutions proposed in the literature and grouped according to the data feedback used (vision based architecture, force information and other sensor system) are presented and discussed.

- the third chapter firstly presents several classical force control architectures. Then a comparative study of two advanced force control architectures based on computed torque techniques, stochastic design and predictive approach is done. In the context of beating heart surgery, simulations are performed to assess controller performances in terms of precision, stability, robustness and rejection capacity. Results are regrouped and presented along a discussion to highlight strong and weak points of these advanced control architectures.

- the fourth chapter presents our two cascade control architectures. The first one is based on active observer techniques and the second merges MPC and AOB techniques. The overall architectures are detailed and realistic experimental results are presented.

- the last part concludes the thesis by summarizing the contribution done. Work perspectives and additional possibilities for further research are discussed.

Le hasard ne favorise que les esprits préparés.

Louis Pasteur

1.6 Publications / Award

This work was published in major robotic conferences and also in a reference journal in the area of applied control. Additionally, an award has been given for force control achievements in the area of heart motion compensation.

International conferences

- M. Dominici, P. Poignet and E. Dombre, Compensation of Physiological Motion using Linear Predictive Force Control, *Proc. of the IEEE Int. Conf. on Intelligent Robots and Systems (IROS'08)*, Nice, France, September 2008.
  [Dominici et al., 2008]

- M. Dominici, P. Poignet, R. Cortesão, E. Dombre and O. Tempier, Compensation for 3D Physiological Motion in Robotic-Assisted Surgery Using a Predictive Force Controller: Experimental Results, *Proc. of the IEEE Int. Conf. on Intelligent Robots and Systems (IROS'09)*, St Louis, MO, USA, October 2009.
  [Dominici et al., 2009]

- M. Dominici, R. Cortesão and C. Sousa, Heart Motion Compensation for Robotic-Assisted Surgery Predictive Approach vs. Active Observer, *Proc. of the IEEE Int. Conf. on Robotics and Automation (ICRA'11)*, Shanghai, China, May 2011.
  [Dominici et al., 2011]

- M. Dominici, R. Cortesão, Model Predictive Control Architectures with Force Feedback for Robotic-Assisted Beating Heart Surgery, *Proc. of the IEEE Int. Conf. on Robotics and Automation (ICRA'14)*, Hong Kong, China, May 2014.
  [Dominici and Cortesão, 2014b]

- M. Dominici, R. Cortesão, Cascade Robot Force Control Architecture for Autonomous Beating Heart Motion Compensation with Model Predictive Control and Active Observer, *Proc. of the IEEE RAS/EMBS Int. Conf. on Biomedical Robotics and Biomechatronics (BioRob'14)*, São Paulo, Brazil, August 2014.
  [Dominici and Cortesão, 2014a]

Journal

- M. Dominici, R. Cortesão, Cascade Force Control for Autonomous Beating Heart Motion Compensation, *Control Engineering Practice*, April 2015.
  [Dominici and Cortesão, 2015]

Award

- Best Application Paper Award Finalist, Compensation for 3D Physiological Motion in Robotic-Assisted Surgery Using a Predictive Force Controller: Experimental Results, *Proc. of the IEEE Int. Conf. on Intelligent Robots and Systems (IROS'09)*, St. Louis, MO, USA, October 2009.
  [Dominici et al., 2009]

Chapter 2

Related work

Contents

Tell me and I will forget; show me and I may remember; involve me and I will understand.

Confucius

The first use of a robotic system dedicated to surgery was in 1985 for brain biopsy [Kwoh et al., 1988]. The PUMA 560 robotic system was a tool holder allowing a precise orientation of the needle during neurosurgical biopsies under computed tomography guidance. In 1992, the ROBODOC was designed to assist surgeons (to mill out precise fittings in the femur) during total hip replacement surgeries. It became the first robotic system approved by the food and drug administration FDA[1]. The late 1990s saw a great deal of work in the area of telesurgery with the introduction of the *da Vinci* surgical system. This platform provides to the surgeon a superior workspace visualization, an enhanced dexterity, movements more precise and an ergonomic comfort. But physiological motions due to heartbeats and respiration still need to be manually compensated by the surgeon. In this chapter we give an overview of different methods proposed in the literature to deal with physiological motions. Since few groups work on the same subject[Bowthorpe and Tavakoli, 2016], solutions presented are not especially focus on beating heart surgery.

[1]The food and drug administration is a federal agency of the united states department of health and human services of the United States of America.

2.1 Vision and data fusion

[Nakamura et al., 2001] were the first to develop the concept of heartbeat synchronization. The solution consists in canceling the relative motion between the robot end-effector and a point of interest on the beating heart. Manipulating a master device the surgeon controls the relative position between the robot and the point of interest. To track the heart motion a vision system is set up. It is composed of two cameras, a color camera giving an overview of the workspace and a monochrome high-speed camera (955 [Hz]) tracking the heart surface (see Fig. 2.1). Displacement information is used to stabilize images from the camera color, giving to the surgeon a stable visual feedback of the surgical task and for the control architecture to synchronize the robot with the organ. Experimental assessments have been conducted with an artificial environment. A laser point projected on a paper is oscillating along 2 dimensions with two sinusoidal motions at 1.5 [Hz]. The vision system uses the laser as a point of interest for the tracking algorithm. No details about the master-slave controller are mentioned. The results are quite good, the maximal error is 0.5 [mm] for both dimensions. However a spectral analysis of a pig's heart motion (see Fig 4.4(a)) shows it is composed of seven frequency components: two due to respiration and five due to heartbeat motions. Even if only heartbeat frequencies are in consideration, four of them are beyond 1.5 [Hz]. To simulate the heart motion the laser should have been composed of these missing terms and not only with the main component of the heartbeat motions.

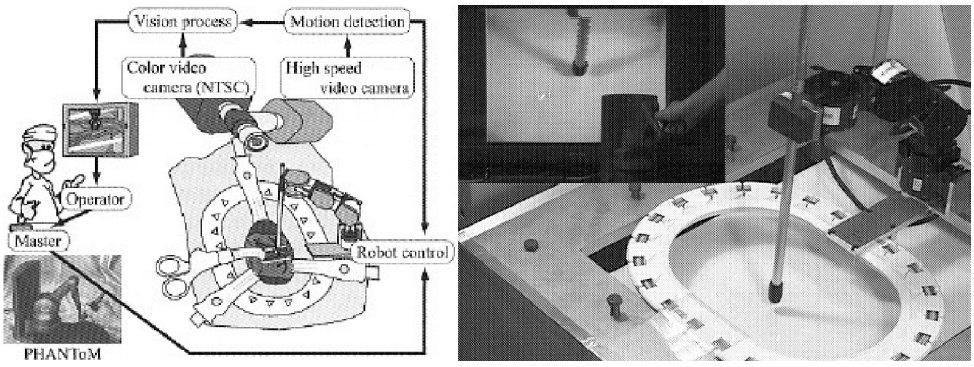

Figure 2.1: Heartbeat synchronization. Experimental setup composed of two camera and artificial markers. Images from the high-speed camera are used to cancel the relative motion between the surgical instrument and the beating heart. (source: [Nakamura et al., 2001]).

[Ginhoux et al., 2005] propose a motion canceling algorithm based on a high-speed vision system, a disturbance predictor and a generalized predictive control (GPC). Since heart motions are the combination of heartbeats and the respiration motion they used an adaptive frequency cancellation filter to separate both signals from the measured perturbation. Then assuming the periodic characteristic of both signals the disturbance predictor computes the future sample disturbance. These predicted signals feed a regular GPC which controls the end effector robot. *In vivo* experiments have been conducted along the three dimensions. Optical markers (four LEDs) attached to the pig's heart and the laser attached to the robot is tracked by the vision system. The relative position between markers and the laser dot is extracted to feed both control and prediction algorithms. A picture of the experimental setup is presented on Fig. 2.2. Experimental results present a maximal error of 2.7 [mm] for both dimensions. Results for the third dimension were not relevant because the robot used was not able to move fast enough along this axis. Since the prediction algorithm requires a cardiac rhythm constant, the cardiac frequency needs to be controlled. For these experiments this was done by drug injections.

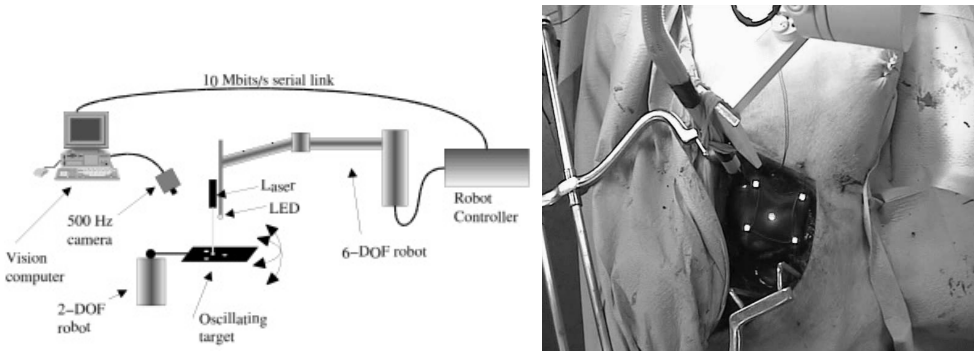

Figure 2.2: Experimental setup for motion canceling algorithm. Experimental visual servoing setup using artificial landmarks and high-speed vision system. (source: [Ginhoux et al., 2005]).

The approach proposed in [Bebek and Çavuşoğlu, 2007] is based on the fusion of the heart motion and the electrocardiogram (ECG) signal. A prediction algorithm coupled with a predictive controller is used. Physiological motions are measured by sonometric sensors: piezo-electrical crystals are sewn to the heart surface or fixed inside the pericardium. The reconstruction of the heart motion is realized off-line. Simultaneously ECG signal are recorded and an analysis is performed to found correspondences between heart motion and its electric activity. Based on the periodicity of the heart motion, previous heart cycles are used as feedforward signal to predict the future heartbeat motion. Correspondences between ECG and heart motion are used to synchronize the heartbeat cycles. A polynomial term is used to correct the offset between heartbeat motion and prediction due to the respiration [Cuvillon et al., 2005]. Experimental results have shown a maximal error larger than 4 [mm]. This method is not clinically viable as it needs an off-line analysis of the motion data and as the crystals must be sutured onto the surgical site. Fig. 2.3 is a schematic architecture representing the system: prediction, data fusion and control.

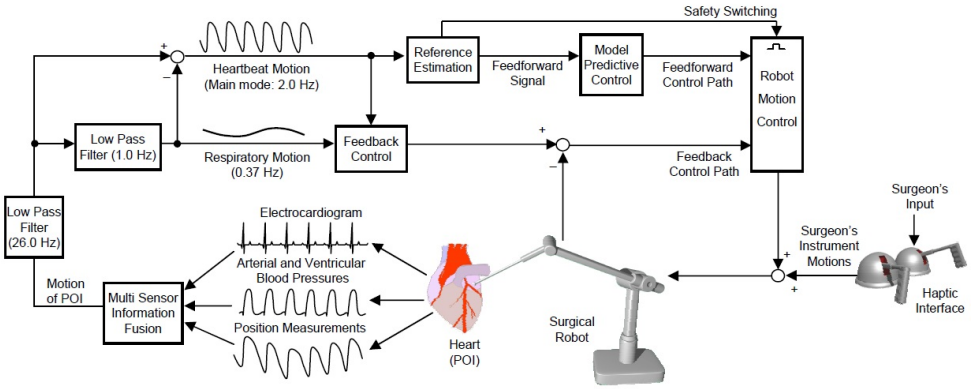

Figure 2.3: Intelligent control architecture for active relative motion canceling. Based on the periodicity of the heart motion, the control algorithm uses previous heart cycles to predict the future heartbeat motion. Correspondences between ECG and heart motion are used to synchronize the heartbeat cycles. Predictions are used by a predictive controller to compensate the heart motion. (source: [Bebek and Çavuşoğlu, 2007]).

Bachta and co-authors propose in [Bachta et al., 2011] to improve classical stabilizer solutions. These devices are mounted at the tip of a long shaft introducing a significant flexibility into the mechanical structure. Because of that, heart motions can not be totally constrained and residual motions still remain. The idea is to cancel these residual motions by controlling the position of the stabilizer along one direction. The Cardiolock prototype is illustrated in the figure 2.4. A high-speed camera system is used to track the device displacement. Position data are used by a prediction algorithm to estimate the future heart motion. Then both position data and the heart motion estimation are send to an H_∞ controller which one maintains the stabilizer position. *In vivo* experiments have been performed. The Cardiolock is a 1 DoF active stabilizer with suction capability to grip on the heart surface. It constrains the heart motion along the vertical axis. The maximal residual motion of the stabilizer is under 0.2 [mm] (on the vertical direction), what is impressive. However the residual heart motion, what is the most interesting, is not mentioned. The Cardiolock device uses vacuum pressure to grip the heart surface which may inflict tissue damages to the heart.

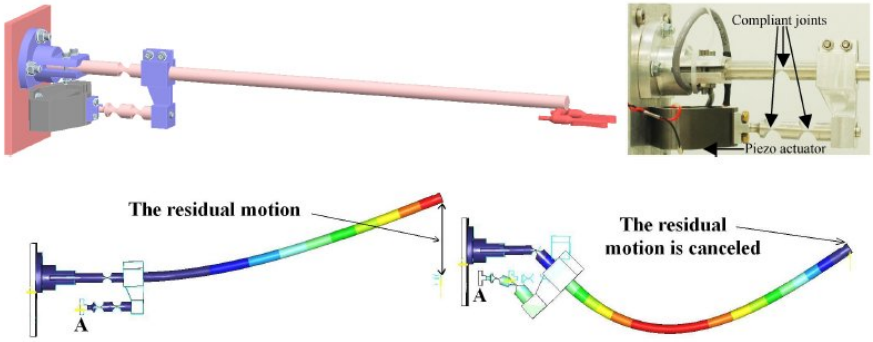

Figure 2.4: Cardiolock active heart stabilizer. The CAD model of the stabilizer and a detail of the actuation mechanism on the top. A finite element analysis of the compensation, with magnified displacements on the bottom. (source: [Bachta et al., 2011]).

Recently, in [Khoshnam and Patel, 2014] authors proposed a technique to reduce contact force variations between a catheter tip and the cardiac tissue during cardiac ablation surgical task. From camera images, the control system estimates the moving target frequency and synchronizes the catheter tip with the target motion. A small piece of artificial tissue is fixed to the top plate of a force sensor and used as target (see Fig. 2.5). Experimental evaluations have shown a real improvement of the contact force quality. Nevertheless, due to actuation mechanism, the compensation frequency has to be above 0.65 [Hz].

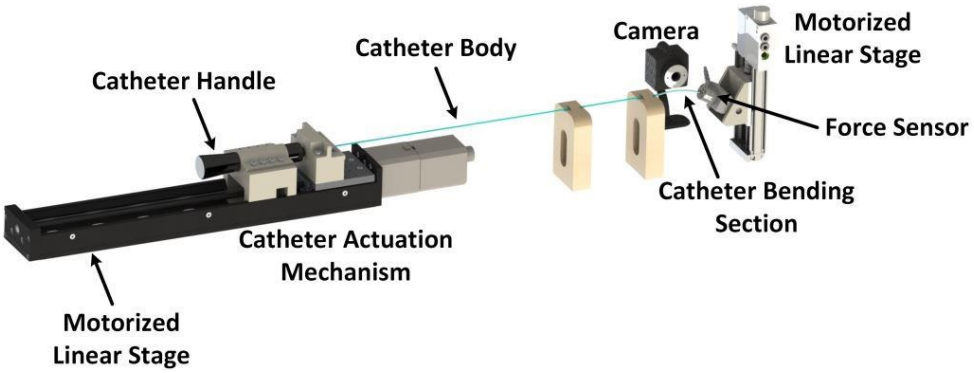

Figure 2.5: Robotic assisted catheter for cardiac ablation. (source: [Khoshnam and Patel, 2014]).

2.2 Force information feedback

As mentioned in [Richa et al., 2010] solutions only based on visual servoing present several drawbacks. Surgeries are performed in a cluttered environment where medical instruments can occlude artificial and natural landmarks. This situation entails tracking problems, disturbing motion compensation. Moreover, contact tasks (e.g., suturing, incision and ablation) locally deform soft tissues, affecting landmark calibration. Another important point is that during contact tasks, physiological motions induce disturbance forces which can hardly be compensated by vision information.

Control architectures based on force feedback do not suffer from these drawbacks. They allow to manage interaction forces between the robot end-effector and its environment. Additionally force information may be used to give an haptic feedback to the surgeon. [Kitagawa et al., 2002] have quantified the effect of force feedback on suture performances. Hand, robot and instrument ties have been analyzed, showing that force feedback would improve robot-assisted performance during knot tying. Hand ties still provide the best results due to distributed tactile sensing of human hands. Fine suturing of soft tissues, not reachable directly by hands or involving high quality and delicate forces, demand haptic augmented reality functionalities to hold knots without damaging tissues. [Okamura, 2004] has analyzed force feedback through visual and audio signals for knot tying tasks, having shown that visual information was more effective (although with less performance than hand ties). The degradation in telemanipulation performance without haptic feedback was evaluated, as well as sensory substitution, motivating the need for true force feedback. [Mayer et al., 2007] conducted experiments involving 25 heart surgeons, to examine claims of force-feedback for robot-assisted surgical procedures. Haptic feedback contributed to better performance, by preventing force-induced damage. Increasing the amplification of force feedback during knot-tying reduced applied forces significantly, not affecting time performance. With regard to fatigue, operating with haptic feedback led to a significant decrease. These results stress the importance of haptic feedback as an indispensable feature for surgical telemanipulators, in particular for operations with delicate suture material.

Cagneau and co-authors [Cagneau et al., 2007] have proposed a force feedback control scheme to compensate the periodic motion of organs. Iterative learning control (ILC) was implemented as an outer-loop to reject periodic disturbances, reducing bad transients during the learning phase (Fig 2.6). The ILC is based on the periodicity of the perturbation. Error induced by the contact motion is considered equal for each cycle. The idea is to anticipate the perturbation taking it into account to compute the command. A proportional term is applied on the previous error to modify the error decay rate. Re-introducing error signal in the system may be disturbing [Longman, 2000], a solution is to apply a low pass filter on the error signal. The solution proposed here is to filter error with a varying cut-off frequency. The algorithm requires a periodic perturbation with a known period. Since the respiration is controlled by an external ventilator device, the breathing motion may be considered as periodic. This hypothesis may however be too restrictive for the random and chaotic nature of cardiac motion [Nakamura et al., 2001]. Tests performed on an artificial moving target with a very simple periodic movement showed large errors.

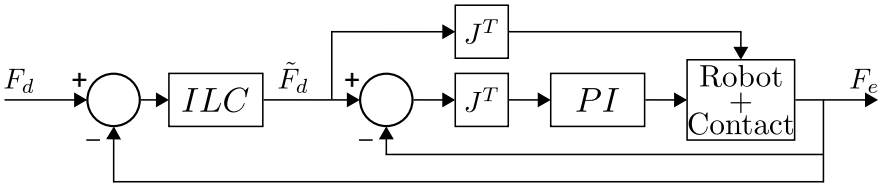

Figure 2.6: Iterative learning control architecture. The control algorithm integrates the ILC as an outer-loop to reject periodic disturbances.

In [Yuen et al., 2010] Yuen and co-authors proposed a hand-held robotic instrument developed for mitral valve repair interventions (see Fig. 2.7). They developed a feedforward force controller to compensate force disturbances induced by the mitral valve motion. Using a 3D ultrasound device, the mitral valve motion is estimated and sent to the controller. *In vivo* experiments have shown good capability to maintain in one direction a constant force on the mitral valve. The force errors were around 0.4 [N].

Figure 2.7: The hand-held robotic device for mitral valve repair surgery developed at the Harvard Biorobotics lab. (source: [Yuen et al., 2009]).

More recently, Kesner and Howe [Kesner and Howe, 2014] presented a catheter robotic system dedicated to beating heart surgery (see Fig. 2.8). A home made 1 DoF distal force sensor provides force feedback information. Additionally, a force-modulated position controller with friction and dead zone compensation was developed to apply a constant force on the mitral valve. Based on observations of previous cardiac motion cycles, a predictive auto-regressive filter estimates the desired catheter acceleration, which is added to the control loop as a feedforward term. The results showed good capability to maintain in one direction a constant force on a fast moving target, although catheter-based solutions have a limited force range.

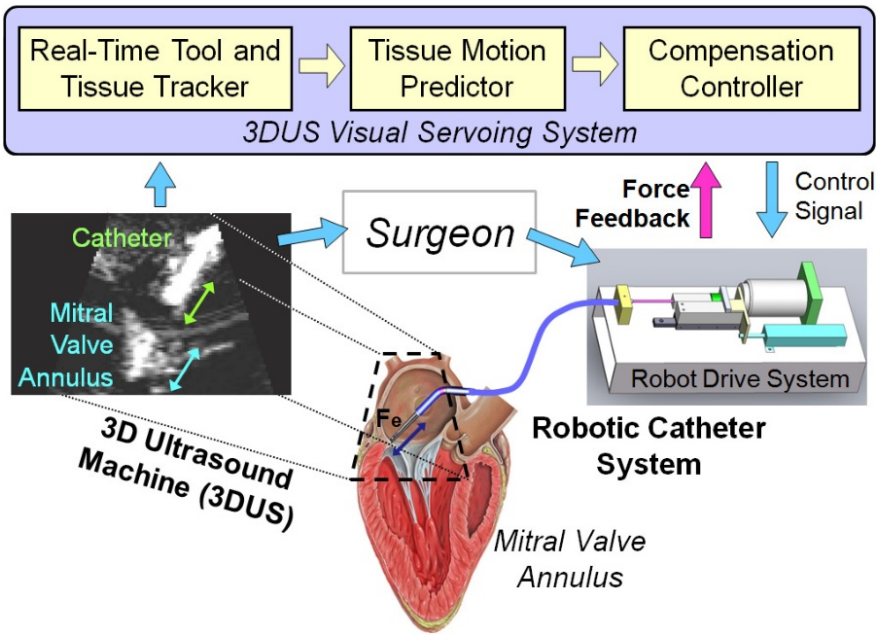

Figure 2.8: Robotic catheter system for beating heart surgery. The control system uses a 3D ultrasound visual servoing (3DUS), a force sensor and a tissue motion predictor to control a catheter and compensates the heart motion. (source: [Kesner and Howe, 2014]).

2.3 Force and vision feedback

For the treatment of a common ear disease, otitis media with effusion (OME), authors in [Liang et al., 2014] developed an office-based surgical device involving head motion compensation. This device provide automatic, precise and quick surgical treatment for OME. Its control architecture is based on force feedback and vision for head motion compensation (see Fig. 2.9. Experimental results show this controller provides better performances than a pure force feedback (see Fig. 2.10).

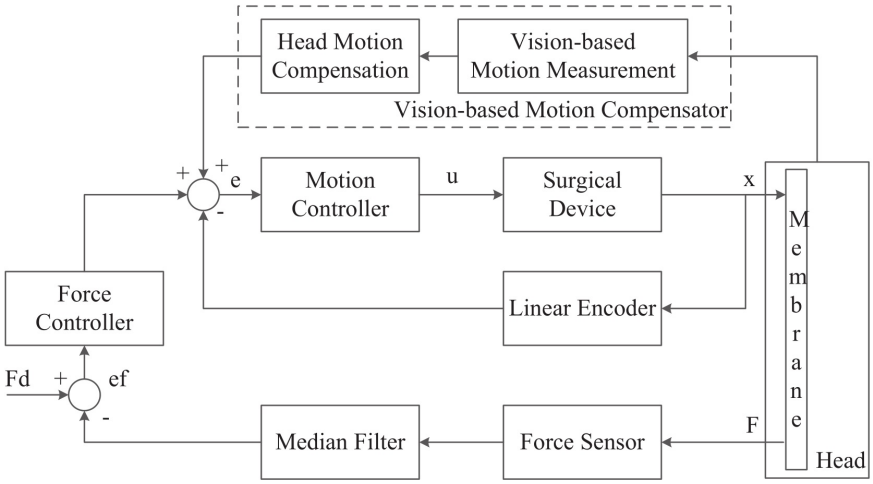

Figure 2.9: Control architecture scheme for the ear disease office-based surgical device. (source: [Liang et al., 2014]).

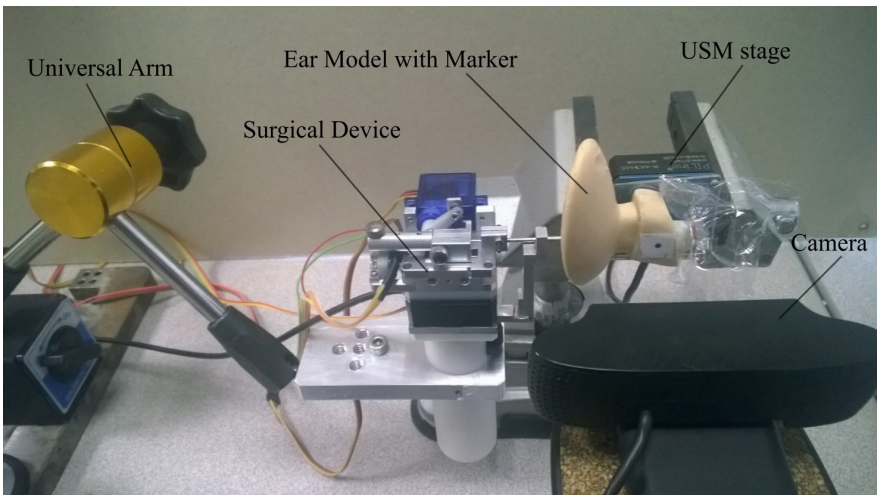

Figure 2.10: Experimental setup for the ear disease office-based surgical device. (source: [Liang et al., 2014]).

2.4 Other sensing information

In [Gagne et al., 2012], they developed a 1 DoF mechanical system coupled with a classical stabilizer based on gyroscopic actuation, accelerometer and optical sensing (see Fig. 2.11). They used an adaptive control which requires knowledge of the fundamental cardiac frequency. *In vivo* experiments have been conducted. Vertical motions of the stabilizer are compensated up to 92%. However the residual heart motion, what is the most interesting, is not mentioned. And moreover the solution does not provide a compensation for the breathing motion.

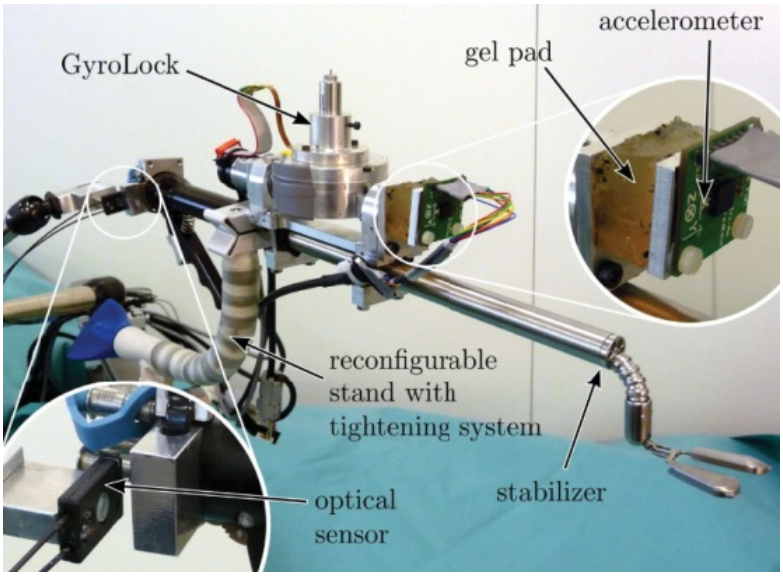

Figure 2.11: GyroLock. The experimental setup is composed of a gyroscopic system coupled with an accelerometer and an optical sensing mounted on a passive cardiac stabilizer. (source: [Gagne et al., 2012]).

In [Ruszkowski et al., 2015], they experimented heart motion compensation capabilities of a *da Vinci* patient side manipulator (PSM arm). For the experimental evaluation (see Fig. 2.12 the experimental setup) they developed an open loop controller based on spectral line decomposition of the heart motion. It was assumed for this work that the disturbance is periodic and known in advance. The heart motion perturbation signal was based on 35 samples of one period of the left ventricular midwall motion. Results demonstrated that the PSM arm is mechanically capable of achieving the dynamics required to compensate heart motions.

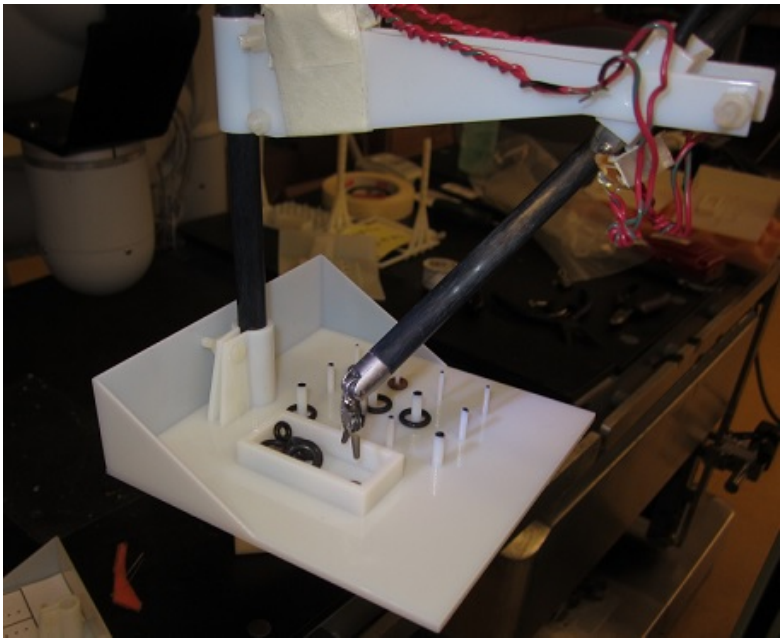

Figure 2.12: Heart motion compensation for the *da Vinci* surgical system. (source: [Ruszkowski et al., 2015]).

2.5 Workaround

A prototype robotic tools have been developed for assisting surgeons on specific interventions on the heart with reduced invasiveness. The HeartLander device, presented in [Patronik et al., 2012] consists of a miniature mobile robot designed to be introduced into the pericardial sac and adhere to the epicardial surface by suction, moving to any desired location in an inchworm-like fashion (see Fig. 2.13). The device can be used in procedures such as atrial ablation, epicardial electrode placement and myocardial injection of drugs.

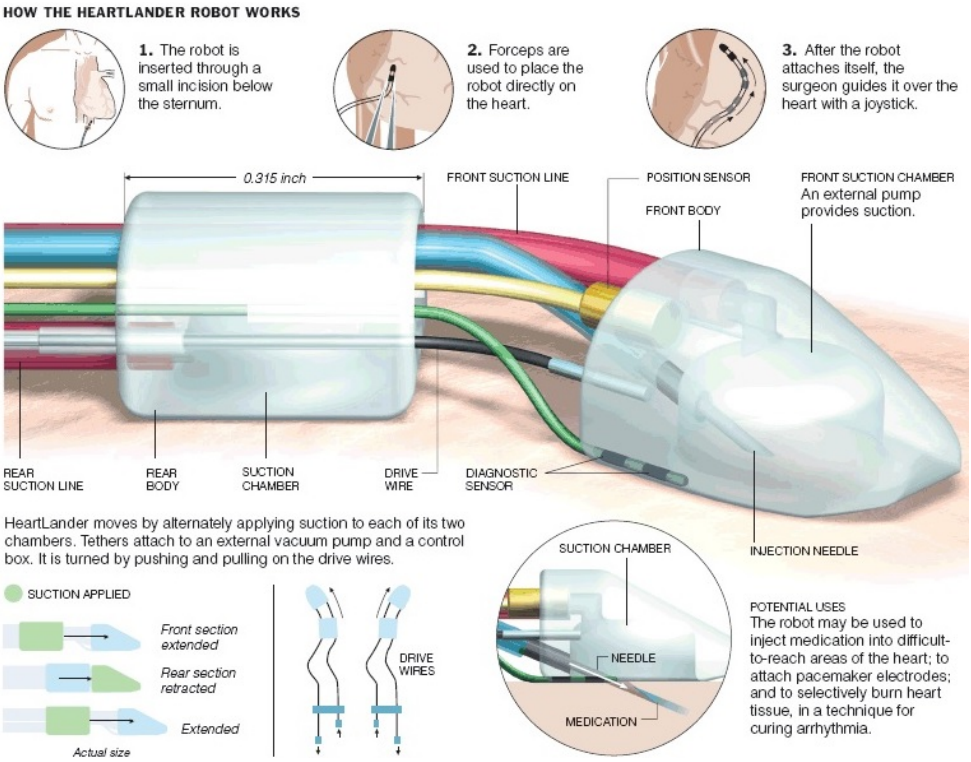

Figure 2.13: The HeartLander robot. (source: [Patronik, 2008] and www.nytimes.com).

2.6 Discussion

The related work presented in this chapter shows that two major techniques tackle heart motion compensation, relying either on vision or force data to do the job. Due to the complexity of the problem at hand, most of the techniques only present results for 1 DOF, which is clearly not enough for real heart surgeries. Additionally, force control has been little explored so far as compared to position control architectures to control robot motion. Therefore, in this thesis we have the ambition to tackle the heart motion compensation problem for a 3-DOF scenario, using explicit force control architectures, providing new research insights.

Chapter 3

Force controllers in virtual environment

Contents

Theory is when you know all and nothing works. Practice is when all works and nobody knows why. In this case we have put together theory and practice: nothing works... and nobody knows why!

Albert Einstein

Designing a controller is based on *a priori* knowledge of the physical system. A controller is chosen and its transfer function is adjusted to obtain a desired closed-loop behavior. If stability is the main constraint, other performances are expected such as: small rise-time, high precision for reference tracking, global system robustness, etc. Conception is based on an ideal model of the real physical system. In our case, the robot model is based on identification processes and it is composed of a set of physical equations. This model is an approximate representation of the real system, several deficiencies can be identified: dynamic behaviors simplified, non linearities neglected, parameters poorly identified, etc. In addition a drift of internal parts of the robot (electrical component, mechanical device, etc) can appear with time. All of these imperfections affect the global behavior of the controller, reducing performances for best cases and at worst introducing instabilities. The robustness is the capacity of a system to guarantee stability and other performances face to system drifts and model approximations. For basic or classic controller this notion is most of the time a posteriori observation. Advanced controllers take into account robustness study directly during their design phase.

We propose in this chapter an experimental comparative study of two advanced control architectures whose robustness properties have been already presented through several publications or books: model predictive control [Camacho and Bordons, 2004] and an approach by pole placement using an active observer [Cortesão, 2007]. The context of this study is cardiac surgery, especially compensation for external perturbations due to physiological motions (breathing and heartbeat). We focus our work on force control, to ensure that all efforts, due to the interaction between robot end-effector and its environment, are under control.

First an overview of classical force controller is presented in the first section. Second section is focused on techniques to identify the experimental platform and to compute its model. Next sections present investigation realized on the different control laws through two parts: first an analytic presentation followed by a performance evaluation through experimental tests.

This chapter is based on these books: [Khalil and Dombre, 1999], [Sciavicco and Siciliano, 2002], [Maciejowski, 2002] and
[Camacho and Bordons, 2004]. They cover these topics: identification, characterization, control and robustness of systems.

3.1 Classical force control architectures

Proprioceptive sensors (encoders, tacho generators, etc) coupled to a position controller are most of the time sufficient for simple or repetitive tasks. The environment is known and motionless, the system evolves 'blindly'. With a moving or misidentified environment, exteroceptive sensors are added to the position control loop. Contact sensors, proximity sensors, force sensors, etc, allow to manage basic interactions between the robot and its environment. However managing environment interactions with purely position-based systems requires a precise model of the physical system and a good knowledge of the environment (location and stiffness). Undesired contact may cause a deviation of the end-effector from the desired position, the position controller reacts to reduce it. This ultimately leads to a build-up of the contact force until the joint actuator saturation is reached or a breakage of parts in contact occurs. The higher the environment stiffness and position control accuracy are, the easier this situation can occur. A force controller allow to manage and to keep under control interactions between robot and its environment. First works developed by [Whitney, 1985] define bases and propose a classification of robot force control algorithms grouped in two parts: the implicit force control and the explicit force control. The first one achieves a force control via a position loop without either an explicit force reference or a force feedback. Second one allows to control force interactions through a desired force reference.

3.1.1 Implicit force control

Passive compliance control

The first approach proposed by [Whitney and Nevins, 1979] is a simple mechanical solution to reduce contact forces between the robot and its environment. It is based on a deformable mechanical interface, called remote center compliance (RCC) interposed between the manipulated part and the robot. The physical configuration of the mechanical device changes under the effect of contact forces, adding to the structure an elastic behavior that compensates positioning errors (Fig. 3.1). The passive compliance through a RCC device offers some advantages such as fast and accurate insertions of parts without requiring a complex strategy. The limitation is that each compliant device is for a specific task and workpiece.

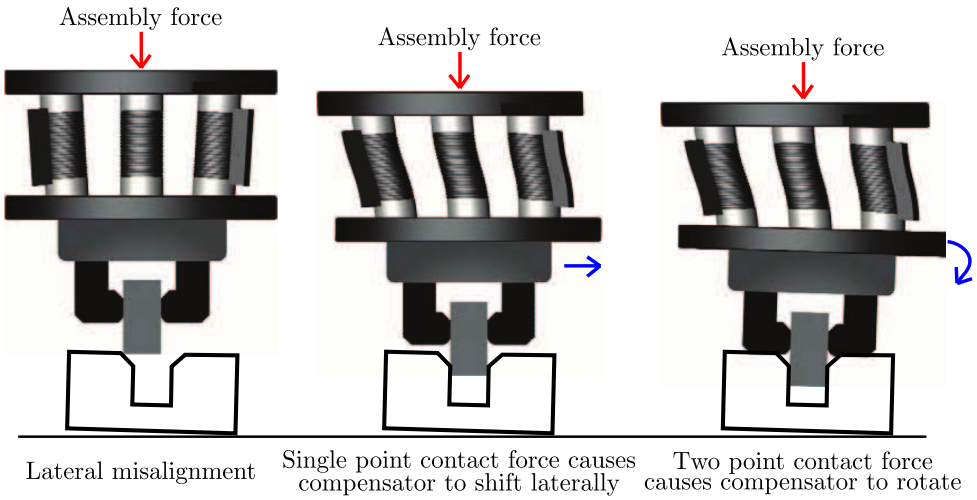

Figure 3.1: Conceptual sketch of remote center compliance (source: www.ati-ia.com).

Active stiffness control

This method actively controls the apparent stiffness of the robot end-effector and allows simultaneous a position and a force control. The user can specify the three translational and three rotational stiffnesses of a desired compliance frame. The system reacts such as a spring with a variable stiffness, reducing contact forces between the system and its environment during the interaction phase [Salisbury, 1980]. The relation between a differential displacement dX in Cartesian space and the resultant force f is given by

$$f = K_s dX \tag{3.1}$$

with K_s the desired stiffness matrix. Assuming the friction and dynamic forces are compensated or are small enough to be neglected, the relation between a force f in Cartesian space and a torque Γ in joint space is given by

$$\Gamma = J^T f. \tag{3.2}$$

A displacement in Cartesian space gives in joint space

$$dX = Jdq. \tag{3.3}$$

Combining (3.1), (3.2) and (3.3), gives

$$\Gamma = J^T K_s J dq = K_p dq. \tag{3.4}$$

K_p is computed from K_s where a high gain is assigned to directions that have to be position controlled, while a low gain is assigned to

force controlled directions. K_p called joint stiffness matrix, determines proportional gains of the control loop in the joint space. The figure 3.2 is a representation of this control architecture. K_v can be interpreted as a damping matrix. Q represents the gravity torque compensation. The active stiffness control schema is simple to implement and stiffness

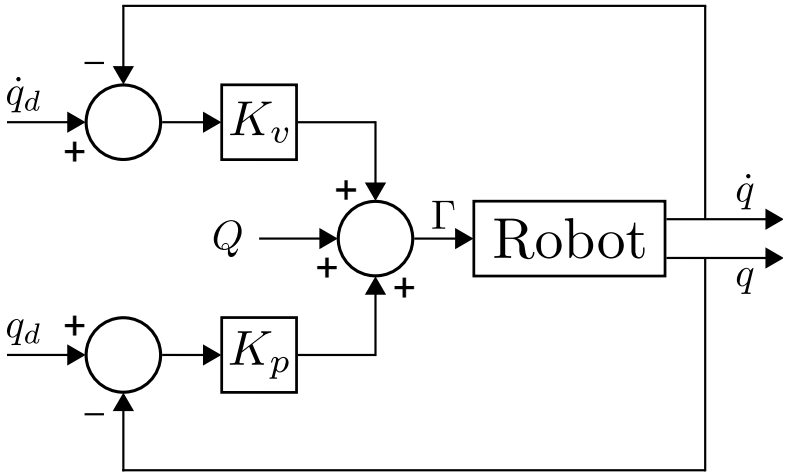

Figure 3.2: Active stiffness control architecture.

matrix can be changed on-line to adapt the robot behavior to various task constraints.

Impedance control

According to [Hogan, 1985], the basic idea of the impedance control is to consider the robot like a mechanical impedance $Z(s)$ and assign a dynamic behavior while its effector is interacting with the environment. The desired performance is specified by a dynamic impedance representing a mass-spring-damper system. This controller specifies the relation between contact forces and end-effector displacements

$$F(s) = Z(s)\,\Delta X(s), \tag{3.5}$$

$$F(s)\,Z(s)^{-1} = \Delta X(s), \tag{3.6}$$

where $\Delta X(s)$ is a displacement in Cartesian space and $F(s)$ represents the induced force. The robot should behave like a mechanical system whose impedance $Z(s)$ is variable according to different phases of the task. In general, we suppose that the robot is equivalent to a mass-spring-damper second order system, whose transfer function is

$$Z(s) = \Lambda s^2 + Bs + K \tag{3.7}$$

where Λ, B and K are respectively desired inertia, damping and stiffness matrices. Values of these matrices are chosen to obtain desired performances:

- high values are given to Λ in directions where a contact is expected, in order to limit robot dynamics;
- high values are given to B in directions where it is necessary to damp the system and dissipate the kinetic energy;
- the stiffness K affects precision of the position controller: along force controlled directions, the stiffness should be small enough to limit the contact forces; conversely, along the position controlled directions, the user should set a high stiffness to obtain an accurate positioning of the end-effector.

Two families of control architecture can be implemented depending on whether or not a force sensor is available [Lawrence, 1988]:

- first one uses the measured position to compute force 'applied' using relation (3.5) (Fig. 3.3);
- second uses a force sensor to measure interaction forces which are translate in a position feedback through relation (3.6) (Fig. 3.4).

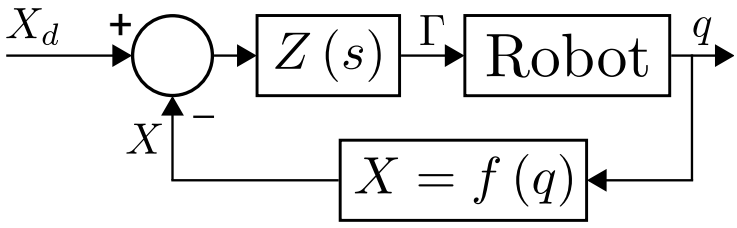

Figure 3.3: Impedance control architecture without force feedback.

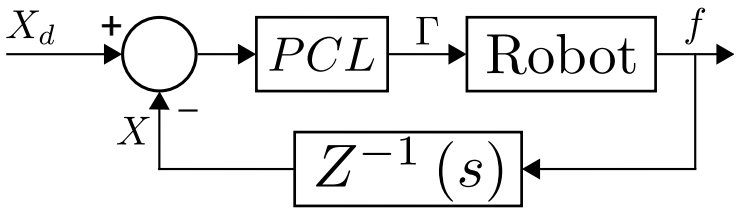

Figure 3.4: Impedance control architecture with force feedback - PCL: position control law.

Conclusion

Significant improvements of different solutions presented can be found in the literature. [Choi et al., 2001] propose to modify the remote center compliance device. The system proposed has an adjustable interface to accept workpieces with different sizes and to be efficient for several tasks. [Volpe and Khosla, 1995] proved that a second order impedance controller gives equivalent results than a simple proportional controller with explicit force feedback.

Implicit force controllers allow to adapt the robot dynamic behavior during the contact phase, but not to control the force applied on the environment. The reference used by the controller cannot be a force. In our case we need to manage all contact forces and to specify a force reference. Next section presents classical force controllers using an explicit force feedback.

3.1.2 Explicit force control

Parallel hybrid position/force control architectures

The idea developed by [Raibert and Craig, 1981] comes from this observation: same directions cannot be controlled simultaneously in force and in position. These controllers are antagonists and exclude themselves mutually. The idea is to divide the workspace in two subspaces: one for directions controlled in position and another one for directions controlled in force, satisfying simultaneously the desired position and force constraints of the task. Directions constrained in position are force controlled and those constrained in force are position controlled. Two parallel control loops, one for position and one for force, are used. Each is based on own sensory system and control law. To avoid actuator conflicts between control commands issued from each loop, a compliance selection matrix S is used. Controller outputs are added and sent to the robot control input as a global command signal G. Each joint may contribute simultaneously to the position control and to the force control. The hybrid position/force controller architecture is presented on the figure 3.5. The type of the control signal G, issued from sum of both control loops, can be

- equivalent to joint torques and it is directly the input Γ of robot actuators;

- equivalent to velocities or displacements in Cartesian space and it has to be multiplied by the robot inverse Jacobian to obtain velocities positions which are references for a joint position controller;

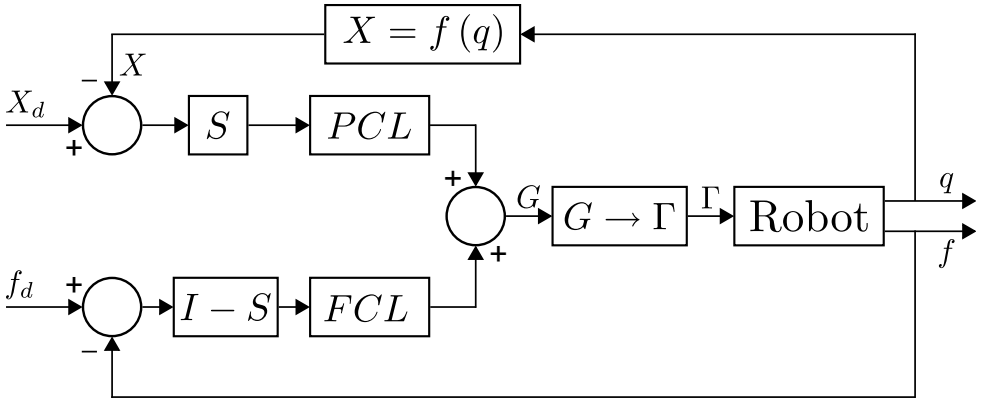

Figure 3.5: Hybrid position/force control architecture - PCL: position control law - FCL: force control law.

- equal to efforts in the operational space and it has to be multiplied by Jacobian transposed matrix.

[Fisher and Mujtaba, 1992] show that controllers using inverse Jacobian J^{-1} (G equivalent to joint torques or to velocities or displacements in Cartesian space) have an unstable behavior in several non singular configurations. This instability comes from the formulation of the inverse Jacobian J^{-1} in the position loop of the hybrid position-force schema. They propose a new stable hybrid position-force architecture (Fig. 3.6).

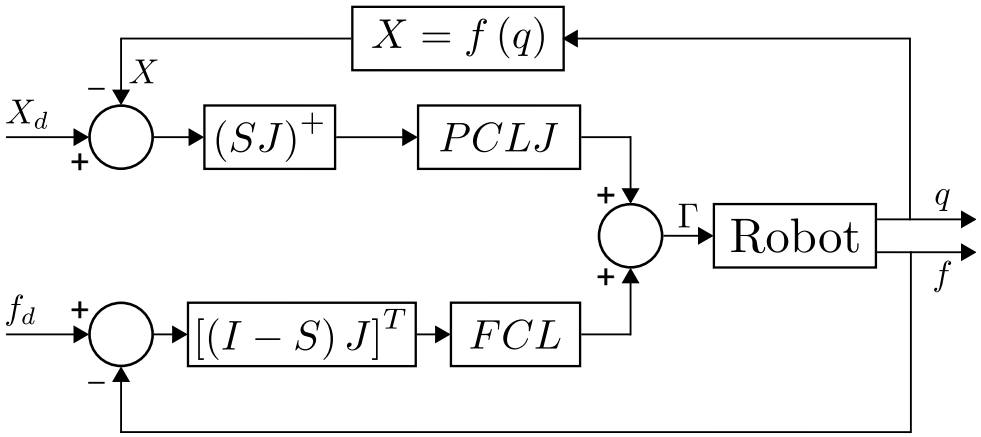

Figure 3.6: Hybrid position/force control architecture from [Fisher and Mujtaba, 1992] - PCLJ: position control law in the joint space - FCL: force control law.

Even if these position/force control architectures allow to manage positions and forces with an explicit feedback, they require an environment well known to avoid undesired contacts along directions controlled in position or free space displacement along directions controlled in force.

External hybrid control architectures

In opposition with the parallel hybrid position/force control architecture, the external hybrid controller allows to control simultaneously along a direction, end-effector positions and forces applied on the environment. Two embedded control loops are used, one external for contact forces and one internal for positions [de Schutter and van Brussel, 1988] and [Perdereau, 1991] (Fig. 3.7). The main idea of this controller is to

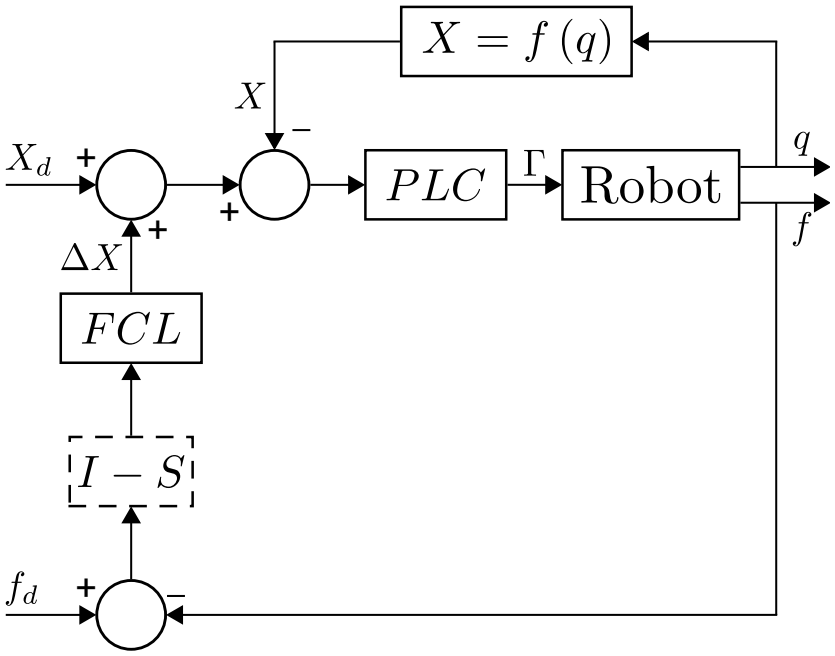

Figure 3.7: External hybrid control schema - PCL: Position Control Law - FCL: Force Control Law.

transform a desired force into a position variation ΔX which is added to the desired position. The new position reference is sent to the position controller. Resulting displacement allows to the system to apply a force on the environment. An integral term in the force control loop cancels a steady state error whatever the position desired. With this term, the force control loop is hierarchically superior to the position loop [Pujas, 1995]. Thanks to architecture and force control loop superiority, the position control law does not require any selection matrix. In a not well known environment, keeping a force reference along directions controlled in position prevents contact forces in case of undesired contact: displacements are 'watched' by the force consign. In opposite, selection matrix may be useful and necessary when task directions have to not be affected by the force measured or during a free space motion. Two other effects are introduced by the integral term. First one, a constant

force reference is transformed in a position ramp which is followed by the end-effector. After the force measured reaches the desired force, the system maintains the position. This is particularly interesting to generate straight trajectory along a direction, it needs simply to apply a force to the end-effector of the robot. Second effect, it is impossible along a direction to have a position consign creating a contact with a force consign equal to zero. The contact necessary introduces a measured force which will be transformed in an inverse displacement until the measured force equals zero. Whereupon the system will reach position consign, generating a force on the environment. Instabilities occur with a force consign closed to zero. A solution is to introduce a limit below which integral term will not affect the force control loop.

3.1.3 Conclusion for classical force controllers

Implicit force control architectures are based on a position feedback to limit contact forces. A desired force cannot be specified. Our context (assistance for beating heart surgery) requires a full control of forces applied by the robot on the environment and especially it requires to use a force as reference signal.

Parallel hybrid position/force controllers propose to merge a position and a force controller. A selection matrix is used to establish exclusively along which directions the force or the position controller is used. A perfect knowledge of the environment is needed to avoid unexpected contacts along a direction controlled in position or to prevent a contact loss along a direction controlled in force. In our context, the environment is approximately known.

The external hybrid controller proposes a control architecture using two nested loops, one in position and another in force. Thanks to integral term and a selection matrix in force control loop, directions controlled in position may be 'watched' by the force loop. This approach has a drawback: instability may occur with force consign closed to zero. Surgical tasks on the heart surface requiring high precision, such as suture and knot tying, are perform with a force consign of few Newton.

More details on developed improvements for these control architectures can be found in these books: [Sciavicco and Siciliano, 2002] and [Khalil and Dombre, 1999].

3.2 Modeling system

The work context is focused on robotic assistance for beating heart surgery and especially autonomous compensation for physiological motions. If respiration involves simple perturbations (large cyclic displacements with low dynamics), heartbeats with high acceleration displacements generate important disturbances. Compensation for these motions, during high precision surgical procedures, requires a robotic system (robot and controller) with high rejection capacities and able to do fast motion with high dynamic accuracy of interaction torques. The task requiring fast motion with high dynamic accuracy, it is necessary to improve control performances by taking into account the dynamic interaction torques: the computed torque control ensures it [Khalil, 1978]. Our experimental setup is composed of a two lightweight robots, one performing surgical gestures (WAM robot) and one simulating the surgical environment (Heartbox). WAM robot dynamic parameters have been identified and estimated, through the methodology proposed in [Sousa and Cortesão, 2014], to establish a mathematical model which will be used for computed torque techniques.

3.2.1 Computed torque techniques

The computed torque method uses inverse dynamic model to canceling the non linearities in the robot dynamics. It ensures a linearized and decoupled system with an uniform behavior whatever the configuration of the robot [Khalil, 1978]. Consequence: a non linear system coupled to the inverse dynamic control form a linearized system which one can be controlled by common linear controllers. Next sections describe this method through joint space and Cartesian space formulations.

Computed torque technique - Joint space Dynamic model is composed of a set of equations establishing relations between joint accelerations $\ddot{q}$ and joint positions q, velocities $\dot{q}$ and torques Γ. Called direct dynamic model (DDM), its expression is given by

$$\ddot{q} = A\left(q\right)^{-1}\left[\Gamma - H\left(q, \dot{q}\right)\right] \tag{3.8}$$

with $A\left(q\right)$ the inertia matrix and $H\left(q, \dot{q}\right)$ the vector of Coriolis, centrifugal and gravity torques. The DDM is usually used to perform performance assessments or to design a well adapted control architecture. It is a coupled and a non-linear system model. In opposition inverse dynamic model (IDM) is used to linearize and to decouple the system

$$\Gamma = \hat{A}\left(q\right) w\left(t\right) + \hat{H}\left(q, \dot{q}\right) \tag{3.9}$$

with $w(t)$ the command vector (computes by an external controller), $\hat{A}(q)$ the estimated inertia matrix and $\hat{H}(q, \dot{q})$ the estimated vector of Coriolis, centrifugal and gravity torques. Dynamic parameters of a real system, necessary to compute $\hat{A}(q)$ and $\hat{H}(q, \dot{q})$ matrices, are never fully known. Combining (3.9) and (3.8) which are respectively the IDM (used for linearization) and the DDM (system model) gives

$$\ddot{q} = A^{-1}\left(\hat{A}w(t) + \hat{H} - H\right). \tag{3.10}$$

In the perfect case where estimated dynamic parameters and physical system parameters are equal, $\hat{A}$, A are equal and $\hat{H}$, H are equal too. Then the new system is described by a set of equations (one by joint) given by

$$\ddot{q} = w(t). \tag{3.11}$$

Then $w(t)$ is equivalent to joint acceleration. The linearized system can be represented by n sub-systems (one per joint). Each sub-system is a double integrator with as input the command vector $w_n(t)$ and as output joint positions q_n, the figure 3.8 represents the linearized and decoupled system.

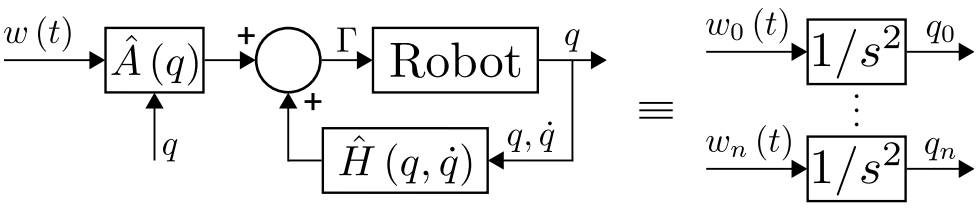

Figure 3.8: Computed torque techniques in the joint space applied to a robotic system. Each sub-system is represented by a double integrator with as input $w_n(t)$ and as output q_n.

Computed torque technique - Cartesian space This formulation allows to describe system behavior in the workspace [Khatib, 1987]. Relation between robot joint positions $q(t)$ and robot end-effector positions X is given by the direct geometric model

$$X = g(q). \tag{3.12}$$

The kinematic model gives Cartesian velocities $\dot{X}$ in terms of joint velocities $\dot{q}(t)$

$$\dot{X} = J(q)\,\dot{q} \tag{3.13}$$

where $J(q)$ is the Jacobian matrix. Differentiating the kinematic model (3.13) with respect to time gives relation between Cartesian acceleration

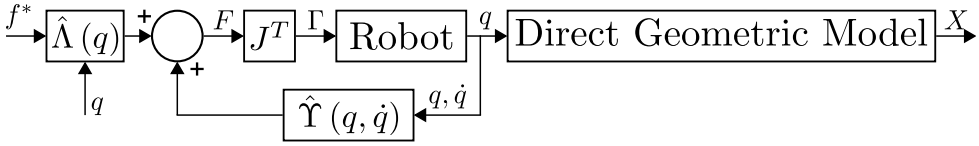

Figure 3.9: Computed torque techniques in the Cartesian space applied to a robotic system. The system command input f^* is equivalent to an Cartesian acceleration.

$\ddot{X}$ and joint acceleration $\ddot{q}(t)$

$$\ddot{X} = J\ddot{q}(t) + \dot{J}\dot{q}(t) \quad \rightarrow \quad \ddot{q}(t) = J^{-1}\left(\ddot{X} - \dot{J}\dot{q}(t)\right). \tag{3.14}$$

The torque vector Γ corresponds to the force vector F in the Cartesian space, the relation is given by

$$\Gamma = J^T F. \tag{3.15}$$

Combining (3.11), (3.14) and (3.15) with the IDM (3.9), gives the inverse dynamic model in Cartesian space

$$F = \hat{\Lambda}(q)\,\ddot{X} + \hat{\Upsilon}(q,\dot{q}) \tag{3.16}$$

where

$$\hat{\Lambda}(q) = J^{-T} A(q) J^{-1} \quad and \quad \hat{\Upsilon}(q,\dot{q}) = J^{-T} H(q,\dot{q}) - \hat{\Lambda}\dot{J}\dot{q}. \tag{3.17}$$

$\hat{\Lambda}(q)$ represents the estimated inertia matrix and $\hat{\Upsilon}(q,\dot{q})$ represents the estimated vector of Coriolis, centrifugal and gravity torques. (3.16) is now used to decouple and to linearize the system in Cartesian space. The system is a set of double integrators (one per Cartesian direction). The figure 3.9 gives a representation of the decoupled and linearized system. f^* is the command input equivalent to a Cartesian acceleration $\ddot{X}$. X is the system output representing a Cartesian position or orientation.

3.2.2 Interaction with environment - Global model

Thanks to computed torque techniques the robotic system is linearized and decoupled. It is composed of a set of individual and identical sub-systems. Each sub-system represents a direction or an orientation in the robot workspace (Cartesian space). The figure 3.9 is a schema representation of the decoupled and linearized system with as input f^* a command vector equivalent to a Cartesian acceleration and as output X a Cartesian position or orientation. To control interaction with the environment a force sensor is added to the robotic system. It allows to

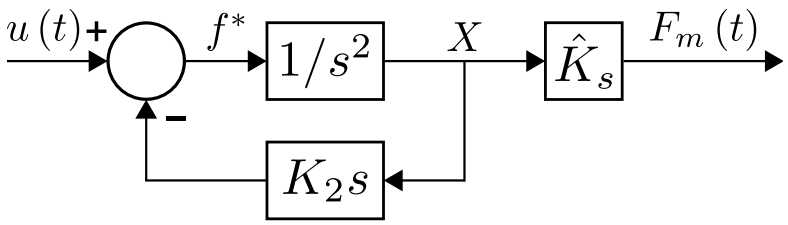

Figure 3.10: Global model of a one direction robot arm with the damping gain K_2 and the estimation of the environment stiffness $\hat{K}_s$.

measure, along each axis, interactions between the tool (manipulated by the robot) and its environment. The force sensor model is taken unitary: the measured force is equal to the force applied. Assuming then next hypothesis: no saturation effect, no drift effect due to temperature, infinite bandwidth, infinite range, etc.

Environment model The work context is focused on robotic assistance for beating heart surgery and especially autonomous compensation for physiological motions. To simulate a surgical environment, a simple interaction model is chosen: spring with a stiffness K_s. Environment model is integrated to the sub-system model to represent interaction force along one axis.

Global model The estimation $\hat{K}_s$ of the environment model represented by a stiffness K_s is included in the one axis robot arm model (sub-system model). A damping feedback loop is added to the system with K_2 the damping gain. This damping loop assures a damped Cartesian position response. The figure 3.10 represents one axis robot arm model $G_{ol}(s)$ composed of a sub-system with a damping loop and the environment model. The command input $u(t)$ is equivalent to a force or a Cartesian acceleration and the output $F_m(t)$ is the force applied by the sub-system on the environment along one axis. The transfer function of a sub-system interacting with its environment is given by

$$G_{ol} = \frac{\hat{K}_s\, e^{-sT_d}}{s(s + K_2\, e^{-sT_d})}\,. \tag{3.18}$$

For small T_d,

$$G_{ol} \approx \frac{\hat{K}_s\, e^{-sT_d}}{s(s + K_2)}\,. \tag{3.19}$$

Its equivalent temporal representation is

$$\ddot{y}(t) + K_2\dot{y}(t) = \hat{K}_s u(t - T_d), \tag{3.20}$$

where the system output $y(t)$ is the force applied F_m by the system on its environment along one axis and $v(t)$ the delayed command vector. Defining two state variables $x_1(t) = y(t)$ and $x_2(t) = \dot{y}(t)$, the state space representation of 3.20 is give by

$$\begin{bmatrix} \dot{x}_1(t) \\ \dot{x}_2(t) \end{bmatrix} = \begin{bmatrix} 0 & 1 \\ 0 & -K_2 \end{bmatrix} \begin{bmatrix} x_1(t) \\ x_2(t) \end{bmatrix} + \begin{bmatrix} 0 \\ \hat{K}_s \end{bmatrix} u(t - T_d). \tag{3.21}$$

This dynamic system is a second order single input/output, with $x_1(t)$ and $x_2(t)$ as state variables representing respectively applied force and its derivative. Discretizing with sampling time T_s, the equivalent discrete time system is of form [1]

$$\begin{cases} x_{r,k} &= \Phi_r x_{r,k-1} + \Gamma_r u_{k-1} \\ y_k &= C_r x_{r,k} \end{cases} . \tag{3.22}$$

The states $x_{r,k}$ has dimension three. The first two states of the discretized system represent respectively the end-effector force and its derivative (only the force is measured). The other state is due to system delay $T_d = T_s$ and equal to u_{k-1}. 3.22 represent the discrete open-loop state space model of the WAM robotic system.

[1] See [Åström and Wittenmark, 1997] for further details on discrete matrices.

3.3 Evaluation protocol

Force control architectures presented in this chapter are evaluated in the context of robotic assistance for beating heart surgery. The robotic platform used in the experiments is presented in Fig. 3.11. It is composed of a lightweight 7 DoF WAM robot used as a tool holder. The robot environment is simulated and it represents a virtual wall all around the robot end-effector. The virtual wall is a spring with a stiffness K_s. Force controllers described in the next sections are implemented on a 2.1 GHz Intel Core 2 processor running Xenomai-Linux. The communication to the WAM robot is performed by CAN bus. Integrity of the system is checked through real-time protection functions, such as maximum velocity, workspace limitation. The control sampling time T_s is set to 1 [ms]. The study is organized as follows. First, force control architectures are presented and analyzed. Then, command law assessments are performed based on physiological motion compensation capabilities and environment stiffness mismatches. Finally, a result synthesis and a conclusion are performed.

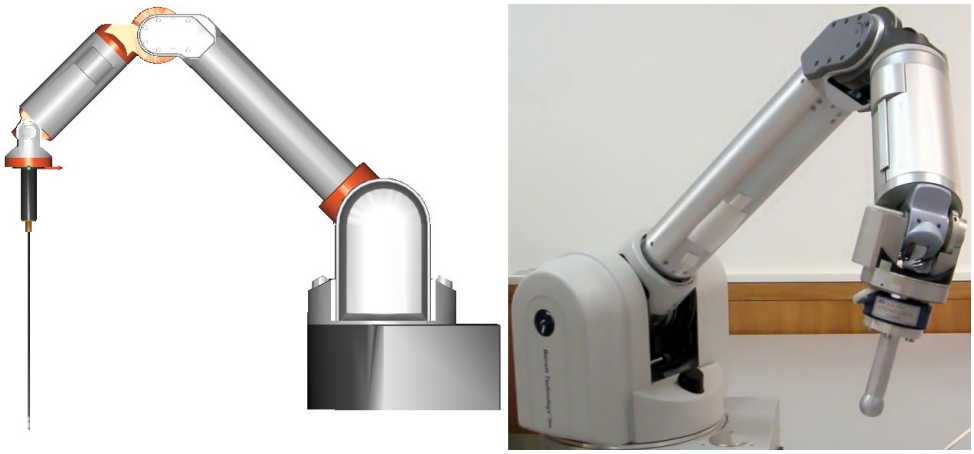

Figure 3.11: Two views of the WAM robot arm. A lightweight 7 DoF robot arm from Barrett Technology.

Mathematical analysis A mathematical description of the control design is performed, giving an overview of implementation and setup procedures.

Rejection evaluation The environment stiffness K_s set to its nominal value, the rejection capability of the controller is evaluated. Respiration and heartbeats involve organ motions, introducing external system disturbances. To evaluate compensation capabilities, external perturbations representing physiological motions are added to the system. Physiological motion data have been recorded during *in vivo* experiments on a pig's heart [Sauvée et al., 2007], representing cardiac and breathing motions along three axes (shown in Fig. 3.12). During the first two seconds the system reaches the force references. Then, physiological motions are introduced along three directions. The control compensation is enabled only after 15.2 [s].

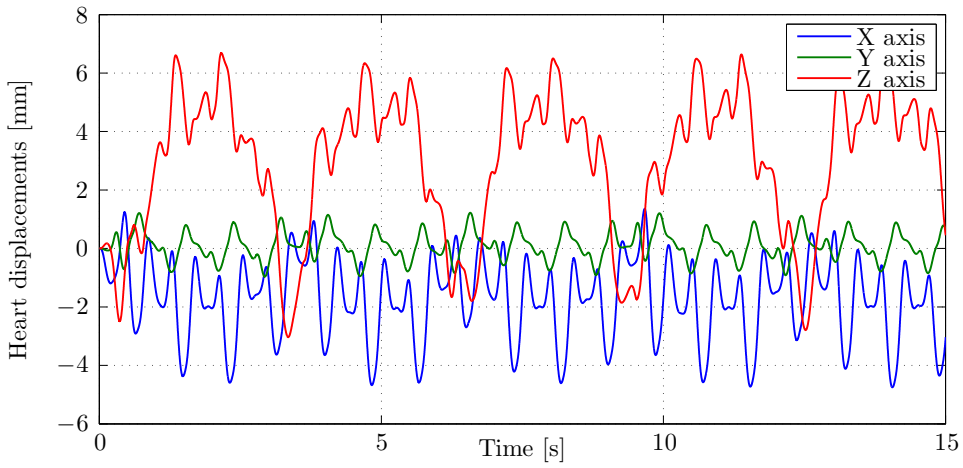

Figure 3.12: Physiological motion data recorded during *in vivo* experiments on a pig's heart along three directions: blue, green and red curves for X, Y and Z axis.

Robustness evaluation Robustness to stiffness mismatches of the control architecture is evaluated. The heart surface is composed of different tissues, such as fat, muscle, and arteries. During surgery the surgeon may interact not only with these tissues but also with surgical tools. Typical stiffness values for fat tissues are 300 [N/m]. The cardiac muscle (myocardium) ranges from 600 [N/m] to 1200 [N/m], and surgical tools (e.g., needle, stabilizer) have more than 1600 [N/m]. To assess robustness capabilities of each control architecture, the environment stiffness K_s is deviated from its nominal[2] value. Three step response simulations are realized alternatively: with a nominal environment stiffness corresponding to the myocardium $K_s = 900$ [N/m], with a environment stiffness set to 200 [N/m] and set to 2000 [N/m]. Time responses are merged to a graphic, highlighting internal disturbance effects on system behavior.

Synthesis Experimental results with virtual environment are analyzed highlighting advantages and drawbacks of the evaluated controller.

[2]In this context, "nominal" means the value used in control design ($\hat{K}_s$).

3.4 Active observer

The active observer approach reformulates the Kalman filter to achieve model reference adaptive control where an extra state is introduced to compensate system disturbances referred to the system input.

3.4.1 AOB architecture

Based on the state space representation of the open-loop system plant G_{ol}, state feedback control by Ackermann's method is used to imposed a desired dynamic and system behavior in closed-loop [Ogata, 2002]. We defined the desired closed-loop model G_{cl} by

$$G_{cl} = \frac{1}{(1 + T_{cl}s)^2} e^{-sT_d}, \tag{3.23}$$

which corresponds to a critically damped system with time constant T_{cl}. Assuming the system (3.22) is completely state controllable, the control command is given by

$$u_{k-1} = r_{k-1} - L_r x_{r,k-1} \tag{3.24}$$

with r_k the control reference and L_r the state feedback gain. The closed-loop system is given by

$$\begin{cases} x_{r,k} &= (\Phi_r - \Gamma_r L_r)\, x_{r,k-1} + \Gamma_r r_{k-1} \\ y_k &= C_r x_{r,k} \end{cases} \tag{3.25}$$

The state feedback gain L_r obtained by Ackermann's formula achieves a desired closed-loop behavior

$$L_r = \begin{bmatrix} L_1 & L_2 & \cdots & L_M \end{bmatrix} = \begin{bmatrix} 0 & \cdots & 0 & 1 \end{bmatrix} W_c^{-1} P(\Phi_r) \tag{3.26}$$

where W_c is the controllability matrix

$$W_c = \begin{bmatrix} \Gamma_r & \Phi_r\Gamma_r & \cdots & \Phi_r^n\Gamma_r \end{bmatrix} \tag{3.27}$$

and $P(\Phi_r)$ the characteristic polynomial to Φ_r

$$P(\Phi_r) = \left(\Phi_r^n + \cdots + a_{n-1}\Phi_r^1 + a_n\right). \tag{3.28}$$

To obtain a unitary static gain of the closed-loop, the reference F_d (force desired) is multiplied by the first element of the L_r vector

$$r_k = L_1 F_d. \tag{3.29}$$

The state feedback control strategy requires a completely observable system state. A Kalman filter is added into the architecture to estimate the system state. Based on the open-loop system (3.22), the system state estimation is given by

$$\hat{x}_{r,k} = \Phi_r \hat{x}_{r,k-1} + \Gamma_r u_{k-1} + E\left(y_k - \hat{y}_k\right) \tag{3.30}$$

with

$$\hat{y}_k = C_r\left(\Phi_r \hat{x}_{r,k-1} + \Gamma_r u_{k-1}\right) \tag{3.31}$$

and E the estimation gain. Introducing modeling errors $e_{r,k}$ and using the state estimation $\hat{x}_{r,k}$, the control command (3.24) becomes

$$u_{k-1} = r_{k-1} - L_r \hat{x}_{r,k-1} + L_r e_{r,k-1}. \tag{3.32}$$

The space state representation of the closed-loop system becomes

$$\left\{ \begin{array}{rcl} x_{r,k} & = & \left(\Phi_r - \Gamma_r L_r\right) x_{r,k-1} + \Gamma_r r_{k-1} + \Gamma_r L_r e_{k-1} \\ y_k & = & C_r x_{r,k-1} \end{array} \right. . \tag{3.33}$$

The control architecture schema is represented in the figure 3.13.

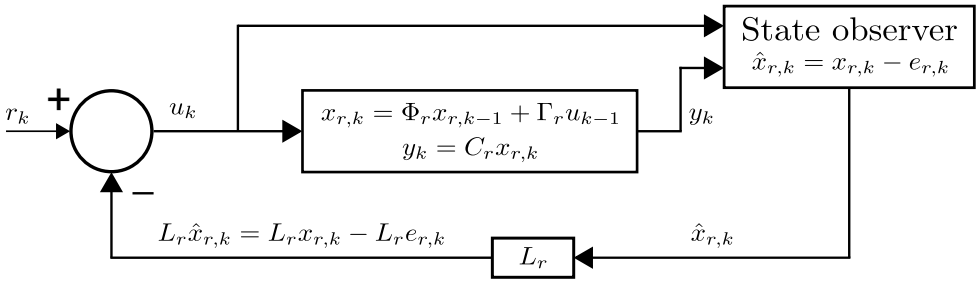

Figure 3.13: State feedback control coupled with a Kalman filter. r_k is the reference, $x_{k,r}$ the system state vector, y_k the system output, u_k the command system input, $\hat{x}_{k,r}$ the estimated system state vector and L_r the state feedback gain.

The Kalman filter is reformulated to introduce an extra state p_k, called active state, which describes system disturbances due to modeling errors referred to the system input. Its estimate $\hat{p}_k$ is reinjected to the control command to perform a compensation action. The control architecture schema is represented in the figure 3.14. The active state p_k is describe by

$$p_k = \sum_{j=1}^{N} (-1)^{j+1} \frac{N!}{j!(N-j)!} p_{k-j} + ^{N-1} \xi_{p_k}. \tag{3.34}$$

The stochastic equation (3.34) says that the N^{th}-order derivative of p_k is randomly distributed. ${}^{N-1}\xi_{p_k}$ is a Gaussian variable with zero-mean. If

$$ {}^{N-1}\xi_{p_k} = 0, \tag{3.35}$$

(3.34) is a deterministic model for any disturbance p_k that has its N^{th} derivative equal to zero. Its state space representation is given by

$$ {}^{N}p_k = \Phi_{2,2} \ {}^{N}p_{k-1} + \ \xi_{{}^{N}p_k}, \tag{3.36}$$

with

$$ {}^{N}p_k = \left[\begin{array}{ccccc} p_{k-(N-1)} & p_{k-(N-2)} & \cdots & p_{k-1} & p_k \end{array} \right]^T, \tag{3.37}$$

$$ \Phi_{2,2} = \left[\begin{array}{ccccc} 0 & 1 & 0 & \cdots & 0 \\ 0 & 0 & 1 & \cdots & 0 \\ \vdots & \vdots & \vdots & \ddots & \vdots \\ 0 & 0 & 0 & \cdots & 1 \\ a_N & a_{N-1} & a_{N-2} & \cdots & a_1 \end{array} \right], \tag{3.38}$$

$$ a_i = (-1)^{i+1} \frac{N!}{i!(N-i)!}, \ i = [1 \ \cdots \ N] \tag{3.39}$$

and

$$ \xi_{{}^{N}p_k} = \left[\begin{array}{ccccc} 0 & 0 & \cdots & 0 & {}^{N-1}\xi_{p_k} \end{array} \right]. \tag{3.40}$$

Eliminating the influence of p_k in $x_{r,k}$ through its perfect estimation and compensation, the closed-loop becomes

$$ \left[\begin{array}{c} \hat{x}_{r,k} \\ {}^{N}\hat{p}_k \end{array} \right] = \left[\begin{array}{cc} \Phi_r - \Gamma_r L_r & 0 \\ 0 & \Phi_{2,2} \end{array} \right] \left[\begin{array}{c} \hat{x}_{r,k-1} \\ {}^{N}\hat{p}_{k-1} \end{array} \right] + \left[\begin{array}{c} \Gamma_r \\ 0 \end{array} \right] r_{k-1} + K_k \left(y_k - \hat{y}_k \right) \tag{3.41}$$

with

$$ \hat{y}_k = C \left(\left[\begin{array}{cc} \Phi_r - \Gamma_r L_r & 0 \\ 0 & \Phi_{2,2} \end{array} \right] \left[\begin{array}{c} \hat{x}_{r,k-1} \\ {}^{N}\hat{p}_{k-1} \end{array} \right] + \left[\begin{array}{c} \Gamma_r \\ 0 \end{array} \right] r_{k-1} \right), \tag{3.42}$$

$$ L_r = \left[\begin{array}{cccc} L_1 & L_2 & \cdots & L_M \end{array} \right], \tag{3.43}$$

the measurement matrix C

$$ C = \left[\begin{array}{cc} C_r & 0 \end{array} \right], \tag{3.44}$$

and r_k the control reference. The Kalman gain K_k reflects uncertainties associated to the system state $\left[\begin{array}{cc} \hat{x}_r(k) & {}^{N}\hat{p}(k) \end{array} \right]^T$

$$ K_k = P_{1k} C^T \left[C \, P_{1k} \, C^T + R_k \right]^{-1}, \tag{3.45}$$

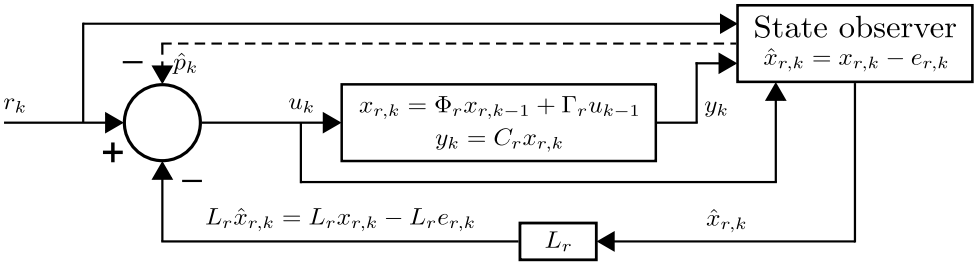

Figure 3.14: Active observer control architecture. The active observer introduces an extra state p_k describing internal disturbances. Re-injecting this extra state $\hat{p}_k$ to the control loop, attempts to compensate theses disturbances.

with

$$P_{1k} = \Phi_n \, P_{k-1} \, \Phi_n^T + Q_k \tag{3.46}$$

and

$$P_k = P_{1k} - K_k \, C \, P_{1k}. \tag{3.47}$$

Φ_n is the augmented open-loop matrix used in the design

$$\Phi_n = \begin{bmatrix} \Phi_{r,n} & \Phi_{1,2} \\ 0 & \Phi_{2,2} \end{bmatrix}, \tag{3.48}$$

with

$$\Phi_{1,2} = \begin{bmatrix} 0 & \cdots & 0 \\ \vdots & \ddots & \vdots \\ 0 & \cdots & 1 \end{bmatrix}, \tag{3.49}$$

and where $\Phi_{r,n}$ is the nominal system matrix of Φ_r (i.e., it represents the values of Φ_r used in the control design). K_k depends on the noise matrices on the system state (Q_k) and measurement (R_k). Q_k is of form

$$Q_k = \begin{bmatrix} Q_{x_{r,k}} & 0 \\ 0 & Q_{^N p_k} \end{bmatrix}. \tag{3.50}$$

Merging modeling errors into the active state makes it more uncertain than the other states, which is reflected in the Q_k stochastic parameters. The absolute values of R_k and Q_k are not important. Only the relative relation between Q_k and R_k is relevant for the Kalman gain [Cortesão, 2007].

3.4.2 AOB design

State feedback gain

State feedback control by Ackermann's method allows to imposed a desired dynamic and system behavior in closed-loop through its state

feedback gain L_r. Equation 3.26 gives the relation between the feedback gain and the characteristic polynomial which describes the desired dynamic behavior

$$P(z) = z^2 + b_1 z + b_2 \tag{3.51}$$

with

$$b_1 = -2e^{\zeta w_n Ts} cos\left(\sqrt{1-\zeta^2} w_n Ts\right) \tag{3.52}$$

and

$$a_2 = e^{\zeta w_n Ts}, \tag{3.53}$$

ζ, w_n and Ts are respectively the damping factor, cut-off frequency (system bandwidth) and the sampling time.

Kalman gain

Noise matrices Q_k and R_k, respectively on the system state and on the measurement, influence the Kalman gain K_k. Their absolute values are not important, only their relative relation is relevant for the Kalman gain [Cortesão, 2007]. R_k is set to 1. Decreasing Q_k makes the system more sensor-based and more sensitive to noise. Increasing it makes the system more model-based.

Extra state

The AOB order N is directly related to the controller ability to track non-linear disturbances. It defined for the force loop the number of state used to describe p_k. A first order AOB ($N = 1$) has shown good performance for force control [Cortesão et al., 2006]. ${}^N p_k$ is equal to

$${}^1 p_k = p_{k-1} + {}^0 \xi_{p_k} \tag{3.54}$$

and

$$\Phi_{2,2} = 1. \tag{3.55}$$

The space state representation of the system is

$$\begin{bmatrix} \hat{x}_{r,k} \\ {}^1\hat{p}_k \end{bmatrix} = \begin{bmatrix} \Phi_r - \Gamma_r L_r & 0 \\ 0 & 1 \end{bmatrix} \begin{bmatrix} \hat{x}_{r,k-1} \\ \hat{p}_{k-1} \end{bmatrix} + \begin{bmatrix} \Gamma_r \\ 0 \end{bmatrix} r_{k-1} + K_k (y_k - \hat{y}_k) \tag{3.56}$$

with

$$\hat{y}_k = C\left(\begin{bmatrix} \Phi_r - \Gamma_r L_r & 0 \\ 0 & 1 \end{bmatrix} \begin{bmatrix} \hat{x}_r(k-1) \\ \hat{p}(k-1) \end{bmatrix} + \begin{bmatrix} \Gamma_r \\ 0 \end{bmatrix} r_{k-1}\right). \tag{3.57}$$

3.4.3 Experimental evaluation

This section assesses experimental results based on heart motion compensation capabilities and environment stiffness mismatches. The AOB control architecture and the virtual environment are implemented on our experimental platform, the lightweight 7 DOF WAM arm. Parameter settings of the control architecture are given. Then experimental tests are presented and discussed. A conclusion highlights strong and weak points of the control architecture.

Parameter settings

The state feedback gain and stochastic parameters of the AOB approach are tuned according to the AOB design section.

State feedback control Critically damped behaviors are appropriate for force-based tasks, since they represent the fastest response without overshoot. Desired closed-loop dynamics for the force assigns the state feedback gain L_r,

$$L_r = \begin{bmatrix} 2,656 & 0,09816 & 0,08759 \end{bmatrix}. \tag{3.58}$$

Force control The stochastic parameters reflect the model reference adaptive control strategy. R_k is set to 1 and Q_k is given by

$$Q_{x_{r,k}} = \begin{bmatrix} 10^{-10} & 0 & 0 \\ 0 & 10^{-12} & 0 \\ 0 & 0 & 10^{-12} \end{bmatrix} \tag{3.59}$$

and

$$Q_{1p_k} = 1. \tag{3.60}$$

The AOB Kalman gain $K_{k,f}$ is equal to

$$K_{k,f} = \begin{bmatrix} 0.9999 & 35.3 & 0.9832 & 0.9832 \end{bmatrix}^T. \tag{3.61}$$

3D Physiological motion compensation

Environment stiffness is set to its nominal value ($K_s = 900$ [N/m]), the rejection capability of the controller is evaluated. Respiration and heartbeat signals along three axes are added to the system. 3D motion compensation results are shown in Fig. 3.15 for AOB approach. System force responses along three directions are represented separately. Blue, green and red curves represent compensation along X, Y and Z axis, respectively. During the first two seconds the system reaches the force references. Then, physiological motions are introduced along three directions. The control compensation is enabled only after 15.2 [s].

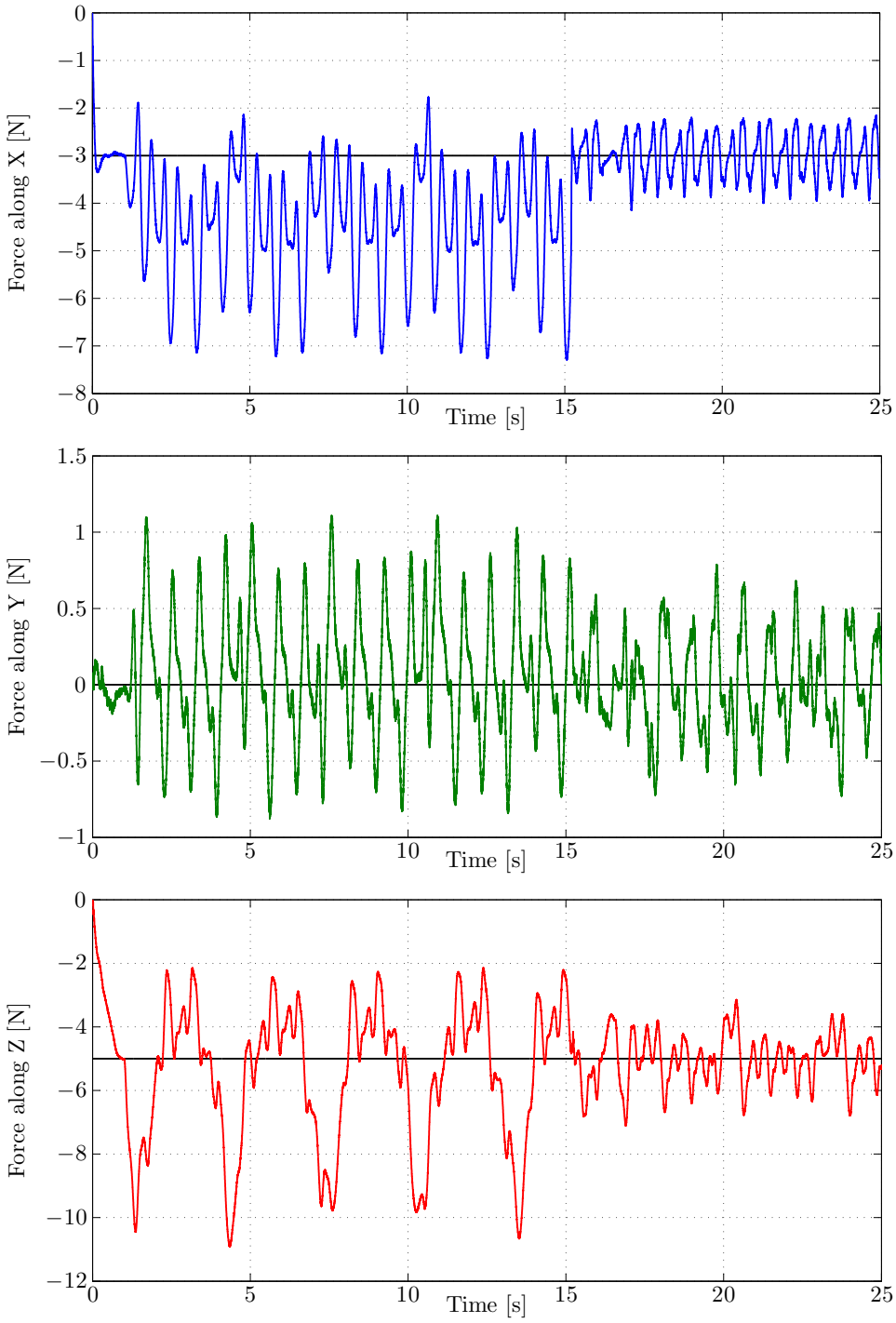

Figure 3.15: Experimental results for 3D heart motion compensation. AOB approach. Forces applied (along X, Y and Z directions) on an moving target for constant desired forces (-3 [N] for X axis, 0 [N] for Y axis and -5 [N] for Z axis).

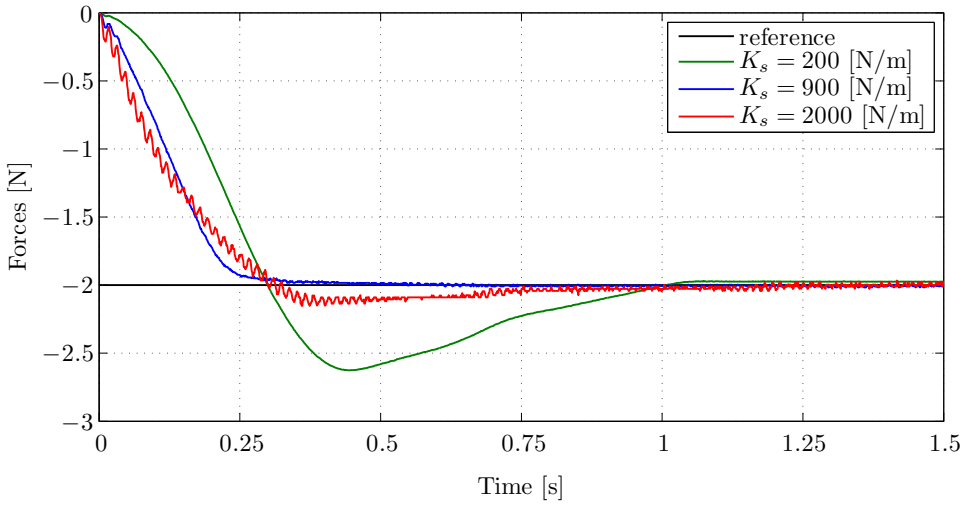

Figure 3.16: Experimental results for stiffness mismatches. AOB controller. System responses for a reference equal to -2 [N] with different environment stiffnesses K_s.

Robustness

To assess robustness capabilities of each control architecture, the environment stiffness K_s is deviated from its nominal[3] value. The figure 3.16 represents robustness experiments for the AOB approach. K_s is alternatively set to 200 [N/m] for soft contact, 900 [N/m] for myocardium contact and 2000 [N/m] for stiff contact, while the nominal stiffness remains constant and equal to 900 [N/m]. The force reference (black curves) is set to -2 [N]. Blue curves represent force responses for the matching case (i.e., $K_s = 900$ [N/m]). Green curves represent force responses for a soft environment (i.e., $K_s = 200$ [N/m]). Red curves represent force response for a stiff environment (i.e., $K_s = 2000$ [N/m]).

Synthesis

Force responses under physiological motions (Fig. 3.15) show good motion compensation performances. Disturbance maximal amplitudes are reduced by 65% for X axis, 25% for Y axis and 55% for Z axis. Y axis low compensation ratio is explained by the physiological motion peak to peak amplitude which is less than 2 [N]. Corresponding position errors can be easily compute from these results. The environment model is a spring with a stiffness equal to K_s. Dividing forces responses by the stiffness $K_s = 900$ [N/m] gives position errors equivalence. Force

[3]In this context, "nominal" means the value used in control design ($\hat{K}_s$).

responses for stiffness mismatch cases (Fig. 3.16) show high frequency components, in the AOB force response. It indicates a system behavior close to instability.

3.4.4 AOB Conclusion

The AOB approach has shown good performances for force control under external disturbances. However residual force amplitudes, around 2 [N], 1.5 [N] and 3 [N] for X, Y and Z axis respectively, are too high to consider these control architectures without further improvements. The robustness analysis has been performed for soft and hard environment stiffness mismatch scenarios. Experimental results highlight robustness capabilities of the AOB approach. High frequency components, in the AOB force response, indicate a system behavior close to instability with 220% environment stiffness mismatch, corresponding to a contact with a bone or a surgical tool.

3.5 Model predictive control

Model predictive control is a model based control architecture developed around a finite receding horizon strategy. It uses an explicit model of the system to predict its outputs along an horizon. The future control signal is computed by minimizing an objective function. The first element of the control sequence is applied to the system. Then the prediction horizon is displaced toward the future and the algorithm is repeated.

3.5.1 MPC architecture

Based on the state space representation of the open-loop system plant G_{ol} which can be represented by

$$\begin{cases} x_k = Ax_{k-1} + Bu_{k-1} \\ y_k = Cx_k \end{cases}, \tag{3.62}$$

where the small system delay T_d can be neglected for the MPC approach [Maciejowski, 2002]. Therefore, x_k has dimension two representing the end-effector force and its derivative. y_k is the applied force and u_k is the input command. From (3.62), the x_k prediction i samples ahead, $\tilde{x}_{k+i}$, is based on u_{k-1}, y_k, $\tilde{u}_{k+i}$ and $\hat{x}_k$, where $\hat{x}_k$ is a state estimation of (3.62). At each sampling time k and along the prediction horizon H_p, the future control sequence $\tilde{u}_{k+i}$ is computed by minimizing a cost function W_k to keep the predicted output $\tilde{y}_{k+i}$ as close as possible to the predicted desired force $\tilde{F}_{d,k}$. Only the first element of the computed control sequence, $\tilde{u}_{k+1}$, is sent to the system plant. As the prediction horizon is displaced towards the future, new output predictions $\tilde{y}_{k+i}$ and new control sequences $\tilde{u}_{k+i}$ are computed at each sampling time.

Strategy

The methodology of the MPC is characterized by the following strategy:

- The finite time horizon H_p defines the slot where predicted outputs $\tilde{y}_{k+i}$ should follow $\tilde{F}_{d,k}$. H_p is bigger than the G_{ol} rise time, and its length greatly influences control tracking capabilities. Extending H_p improves performance, but increases computational time.

- At each time k, based on (3.62), the future outputs $\tilde{y}_{k+i}$ are predicted along H_p, where $i \in [1, H_p]$. $\tilde{y}_{k+i}$ depends on $\hat{x}_k$, u_{k-1}, y_k and $\tilde{u}_{k+i}$.

- The command vector $\tilde{u}_{k+i}$ ($i \in [0, H_p - 1]$) is computed to minimize the cost function W_k, which is a quadratic function of the predicted

errors between $\tilde{y}_{k+i}$ and $\tilde{F}_{d,k}$. W_k also includes predicted control efforts. Two diagonal matrices λ and δ are associated to control efforts and tracking errors, respectively. Increasing λ w.r.t. δ has the effect of reducing control activity, entailing slow response to disturbances. Decreasing λ w.r.t. δ increases control dynamics and tracking performance. Therefore, the relation between λ and δ defines the aggressiveness of the controller in recovering from disturbances [Maciejowski, 2002].

- A control horizon $H_u \leq H_p$ is introduced to reduce computation time. H_u defines the time slot along which the control command $\tilde{u}_{k+i}$ is active (for $H_u \leq i < H_p$, $\tilde{u}_{k+i}$ is kept constant). Although $H_u = 1$ has acceptable performance for stable plants, increasing H_u makes the control more active up to a limit where any further increase in H_u has little effect. For high-performance a larger value of H_u is desirable. When H_u and H_p approach infinity, the prediction controller becomes the well-known linear quadratic regulator (LQR) problem [Camacho and Bordons, 2004].

- Once $\tilde{u}_{k+i}$ has been computed, only the first element $\tilde{u}_{k+i|i=0}$ is applied to system. The whole cycle of output measurement y_k, output predictions $\tilde{y}_{k+i}$, and control sequence $\tilde{u}_{k+i}$ computation is repeated and updated at each sampling time.

The overall MPC strategy is depicted in Fig. 3.17. Since the desired force is not known in advance, $\tilde{F}_{d,k}$ is constant during the entire time horizon H_p and equal to the desired force known at instant k. The MPC control signals $\tilde{u}_{k+i}$ are computed based on the system model and cost function W_k. A good control performance can be achieved with $H_u < H_p$, entailing good tracking capabilities between F_d and y_k.

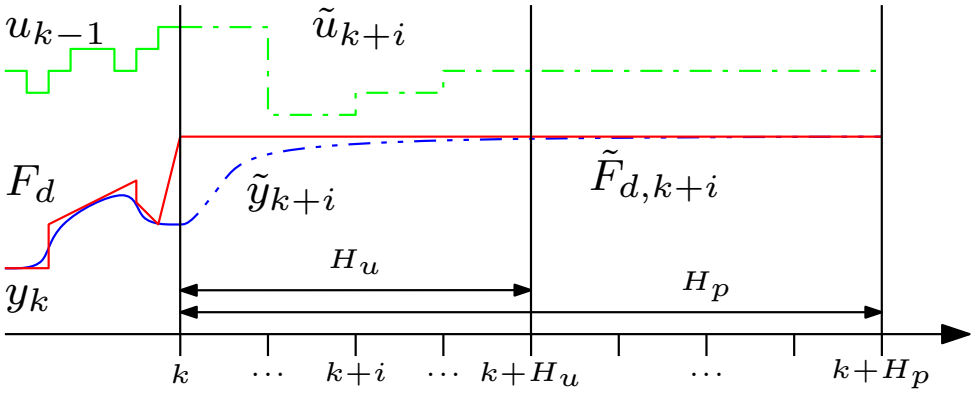

Figure 3.17: Model predictive control strategy. Based on G_{ol}, predicted outputs $\tilde{y}_{k+i}$ (blue dash-dot-dotted curve) are computed along H_p. The reference $\tilde{F}_{d,k+i}$ is the desired force (red curve). Optimal control commands $\tilde{u}_{k+i}$ (green dash-dotted curve) are computed to minimize the cost function W_k. $\tilde{u}_{k+i}$ only changes along H_u.

Formulation

From (3.62) and defining

$$\tilde{u}_k = \Delta\tilde{u}_k + u_{k-1} \tag{3.63}$$

the following state predictions are obtained,

$$\begin{aligned}
\tilde{x}_{k+1} &= Ax_k + B\tilde{u}_k \\
\tilde{x}_{k+2} &= A\tilde{x}_{k+1} + B\tilde{u}_{k+1} \\
&= A^2x_k + AB\tilde{u}_k + B\tilde{u}_{k+1} \\
&\vdots \qquad\qquad \vdots \\
\tilde{x}_{k+H_p} &= A\tilde{x}_{k+H_p-1} + B\tilde{u}_{k+H_p-1} \\
&= A^{H_p}x_k + A^{H_p-1}B\tilde{u}_k + \cdots + B\tilde{u}_{k+H_p-1}\,.
\end{aligned} \tag{3.64}$$

We define a control horizon H_u as $H_u \leq H_p$. Assuming the input command $\tilde{u}_k$ changes only along the control horizon H_u and is kept constant for $H_u \leq i < H_p$, $\tilde{u}_k$ can be represented by (3.65), where $\Delta\tilde{u}_{k+i} = 0$ for $i \geq H_u$ and $\tilde{u}_{k+i} = \tilde{u}_{k+H_u-1}$ for $i \geq H_u$.

$$\begin{aligned}
\tilde{u}_k &= \Delta\tilde{u}_k + u_{k-1} \\
\tilde{u}_{k+1} &= \Delta\tilde{u}_{k+1} + \Delta\tilde{u}_k + u_{k-1} \\
&\vdots \qquad\qquad \vdots \\
\tilde{u}_{k+H_u-1} &= \Delta\tilde{u}_{k+H_u-1} + \cdots + \Delta\tilde{u}_k + u_{k-1}\,.
\end{aligned} \tag{3.65}$$

Merging (3.64) and (3.65) we obtain

$$\begin{aligned}
\tilde{x}_{k+1} &= Ax_k + B\left[\Delta\tilde{u}_k + u_{k-1}\right] \\
\tilde{x}_{k+2} &= A^2x_k + B\left[\Delta\tilde{u}_{k+1} + \Delta\tilde{u}_k + u_{k-1}\right] + AB\left[\Delta\tilde{u}_k + u_{k-1}\right] \\
&= A^2x_k + (A+I)\,B\Delta\tilde{u}_k + (A+I)\,Bu_{k-1} + B\Delta\tilde{u}_{k+1} \\
&\vdots \qquad\qquad\qquad\qquad \vdots \\
\tilde{x}_{k+H_u} &= A^{H_u}x_k + \left(A^{H_u-1} + \cdots + A + I\right) B\Delta\tilde{u}_k \\
&\quad + \left(A^{H_u-1} + \cdots + A + I\right) Bu_{k-1} \\
&\quad + \; B\Delta\tilde{u}\,(k + H_u - 1) \\
\tilde{x}_{k+H_u+1} &= A^{H_u+1}x_k + \left(A^{H_u} + \cdots + A + I\right) B\Delta\tilde{u}_k \\
&\quad + \left(A^{H_u} + \cdots + A + I\right) Bu_{k-1} \\
&\quad + \; (A+I)\,B\Delta\tilde{u}\,(k + H_u - 1) \\
&\vdots \qquad\qquad\qquad\qquad \vdots \\
\tilde{x}_{k+H_p} &= A^{H_p}x_k + \left(A^{H_p-1} + \cdots + A + I\right) B\Delta\tilde{u}_k \\
&\quad + \left(A^{H_p-H_u} + \cdots + A + I\right) B\Delta\tilde{u}\,(k + H_u - 1) \\
&\quad + \left(A^{H_p-1} + \cdots + A + I\right) Bu_{k-1}\,.
\end{aligned} \tag{3.66}$$

Finally (3.66) is written in matrix-vector form

$$\tilde{X_k} = \underbrace{\Psi\hat{x}_k + \Upsilon u_{k-1}}_{\text{past}} + \underbrace{\Theta\,\Delta\tilde{U_k}}_{\text{future}}, \tag{3.67}$$

with

$$\tilde{X_k} = \left[\begin{array}{cccccc} \tilde{x}_{k+1} & \cdots & \tilde{x}_{k+i} & \cdots & \tilde{x}_{k+H_p} \end{array}\right]^T, \tag{3.68}$$

$$\Delta\tilde{U_k} = \left[\begin{array}{ccc} \Delta\tilde{u}_k & \cdots & \Delta\tilde{u}_{k+H_u-1} \end{array}\right]^T, \tag{3.69}$$

$$\Psi = \left[\begin{array}{cccccc} A & \cdots & A^{H_u} & A^{H_u+1} & \cdots & A^{H_p} \end{array}\right]^T, \tag{3.70}$$

$$\Upsilon = \begin{bmatrix} B \\ \vdots \\ \sum_{i=0}^{H_u-1} A^iB \\ \sum_{i=0}^{H_u} A^iB \\ \vdots \\ \sum_{i=0}^{H_p-1} A^iB \end{bmatrix} \tag{3.71}$$

and

$$\Theta = \begin{bmatrix} B & \cdots & 0 \\ AB+B & \cdots & 0 \\ \vdots & \ddots & \vdots \\ \sum_{i=0}^{H_u-1} A^i B & \cdots & B \\ \sum_{i=0}^{H_u} A^i B & \cdots & AB+B \\ \vdots & \ddots & \vdots \\ \sum_{i=0}^{H_p-1} A^i B & \cdots & \sum_{i=0}^{H_p-H_u} A^i B \end{bmatrix}. \tag{3.72}$$

Equation (3.67) is composed of three terms. Ψ, Υ and Θ only depend on A and B matrices, and can be computed off-line. Along the prediction horizon, the first two terms represent the *free response* and the last term is the forced one. The control increment vector $\Delta\tilde{U}_k$ is computed by minimizing the cost function

$$W_k = (\tilde{Y}_k - \tilde{F}_{d,k})^T \delta (\tilde{Y}_k - \tilde{F}_{d,k}) + \Delta\tilde{U}_k{}^T \lambda \Delta\tilde{U}_k, \tag{3.73}$$

with

$$\tilde{Y}_k = \begin{bmatrix} C\tilde{x}_{k+1} & \cdots & C\tilde{x}_{k+i} & \cdots & C\tilde{x}_{k+H_p} \end{bmatrix}^T, \tag{3.74}$$

and

$$\tilde{F}_{d,k} = \begin{bmatrix} F_{d,k+1} & \cdots & F_{d,k+i} & \cdots & F_{d,k+H_p} \end{bmatrix}^T. \tag{3.75}$$

Defining the prediction error $\tilde{E}_k$ as the difference between $\tilde{F}_{d,k}$ and the *free response* of the system,

$$\tilde{E}_k = \tilde{F}_{d,k} - \mathrm{diag}(C)\left[\Psi\hat{x}_k + \Upsilon u_{k-1}\right], \tag{3.76}$$

the cost function (3.73) can be written as

$$W_k = (\Theta\Delta\tilde{U}_k - \tilde{E}_k)^T \delta (\Theta\Delta\tilde{U}_k - \tilde{E}_k) + \Delta\tilde{U}_k{}^T \lambda \Delta\tilde{U}_k\,. \tag{3.77}$$

From (3.77),

$$W_k = \tilde{E}_k^T \delta \tilde{E}_k - 2\Delta\tilde{U}_k{}^T \Theta^T \delta \tilde{E}_k + \Delta\tilde{U}_k{}^T (\Theta^T \delta \Theta + \lambda)\Delta\tilde{U}_k\,. \tag{3.78}$$

Computing the gradient of (3.78) and setting it to zero entails

$$\frac{\partial W_k}{\partial \Delta\tilde{U}_k} = -2\Theta^T \delta \tilde{E}_k + 2\left(\Theta^T \delta \Theta + \lambda\right)\Delta\tilde{U}_k = 0\,. \tag{3.79}$$

The optimal and unique solution $\Delta\tilde{U}_k$ is therefore equal to

$$\Delta\tilde{U}_k = (\Theta^T \delta \Theta + \lambda)^{-1} \Theta^T \delta \tilde{E}_k\,. \tag{3.80}$$

To guarantee that (3.80) gives the minimum of the cost function (3.77), the Hessian of (3.77) is compute

$$\frac{\partial^2 W_k}{\partial \Delta \tilde{U}_k{}^2} = 2\left(\Theta^T \delta \Theta + \lambda\right) . \tag{3.81}$$

Assuming that $\delta \geq 0$ ensure that $\Theta^T \delta \Theta \geq 0$. Imposing $\lambda > 0$ assures an Hessian positive-definite, which is enough to guarantee that (3.80) is the minimum of (3.77). According to the MPC strategy previously described and represented in Fig. 3.18, the first element $\Delta \tilde{u}_{k+i|i=0}$ of the optimal increment sequence (3.80) is added to the previous command u_{k-1} and sent to the plant as u_k. Then all the computation is repeated at each sampling time.

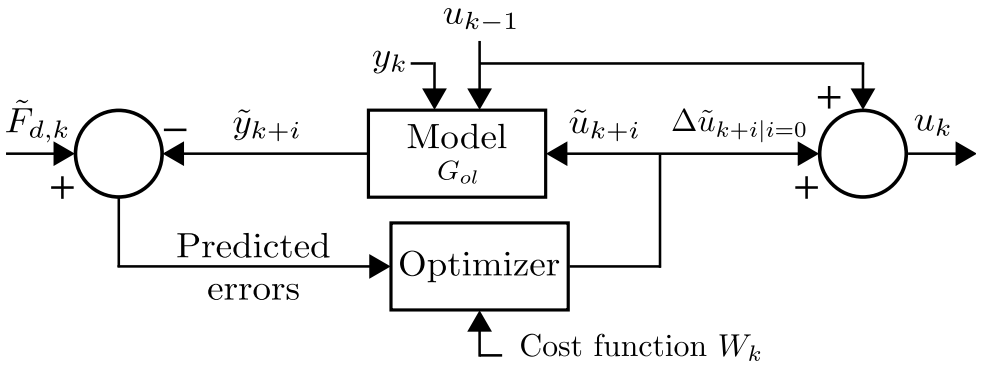

Figure 3.18: Model predictive control architecture. Based on the inner-loop model G_{ol} and on the system data u_{k-1} and y_k, the predictions $\tilde{y}_{k+i}$ are computed for the time horizon H_p. Optimal control commands $\tilde{u}_{k+i}$ are computed minimizing the cost function W_k, which is a quadratic function of predicted errors between $\tilde{y}_{k+i}$ and $\tilde{F}_{d,k}$.

Dimensions of matrices and vectors involved in computing the optimal control command vector follow theses rules (see Tab. 3.5.1):

- Θ has as many rows as there are elements in $\tilde{X}_k$ (deducted from from (3.67)). There are m controlled outputs and prediction are computed for H_p steps, then Θ rows equal $m(H_p + 1)$. Its columns number is the same as the number of elements in $\Delta \tilde{U}_k$, which is $l(H_u)$ where l is the number of plant inputs.
- Knowing Θ dimensions δ has $m(H_p+1)$ rows and columns (deducted from (3.80)).
- Since $\Theta^T \delta \Theta$ is square with $l(H_u)$ rows and columns, then λ is square too with same dimensions (deducted from (3.80).

Matrix	Dimensions	
	Row	Column
δ	$m(H_p+1)$	$m(H_p+1)$
λ	$l(H_u)$	$l(H_u)$
Ψ	$m(H_p+1)$	n
Υ	$m(H_p+1)$	l
Θ	$m(H_p+1)$	
$\tilde{E}_k$	$m(H_p+1)$	1

Table 3.1: Dimensions of MPC algorithm matrices and vectors. The system plant has l inputs, n states and m controlled outputs.

3.5.2 MPC tuning

The length of the prediction horizon H_p greatly influences reference tracking capability. Extending the horizon, a more accurate system is achieved but the computational time increases. Only the relative difference between δ and λ is significant. An accurate system with $\delta > \lambda$ implies a high control effort.

3.5.3 MPC computational problems

A long prediction horizon H_p involves large values of i. Computing the prediction equation (3.67) requires to calculate A^i. This can lead to numerical problems. With an unstable plant some elements of the matrices Ψ, Υ and Θ may become extremely large relative to others, especially for high values of i. Similar problems can occur with a stable plant, some elements of A^i may become extremely small relative to others. A solution is to compute predictions from an iteration algorithm, one step at the time.

The optimal solution (3.80) requires the computation of the inverse of $(\Theta^T\delta\Theta + \lambda)$ matrix. Since the Θ matrix is often ill-conditioned, it is relatively important to pay attention to the numerical algorithm involved in finding the optimal solution. A solution is to compute the optimal solution matrix by solving it as a "least-squares" problem.

3.5.4 Experimental evaluation

This section assesses experimental results based on heart motion compensation capabilities and environment stiffness mismatches. The MPC control architecture and the virtual environment are implemented on our experimental platform, the lightweight 7 DOF WAM arm. Parameter settings of the control architecture are given. Then experimental tests are presented and discussed. A conclusion highlights strong and weak points of the control architecture.

Parameter settings

According to the MPC tuning section, MPC parameters are tuned. Depending on the control loop sampling period ($T_s = 1$ [ms]), a good trade-off for the prediction horizon value appears to be $H_p = 30\,T_s$. To impose a null steady-state error, ϕ^i has to be closed to zero for $i = H_p$, $T_{ref} = 6\,T_s$. Since the *free response* is based on the unstable system plant G_{ol} and the previous control command $u_{k-1} \neq 0$, the increment sequence $\Delta\tilde{U}_k$ has to be defined all over H_p, to maintain the system *free response* under "control". Therefore H_u is set equal to H_p. A large control horizon implies high dynamic control actions and increases computation time. As a consequence, H_p has to be decreased which affects tracking performance.

3D Physiological motion compensation

Environment stiffness is set to its nominal value ($K_s = 900$ [N/m]), the rejection capability of the controller is evaluated. Respiration and heartbeat signals along three axes are added to the system. 3D motion compensation results are shown in Fig. 3.19 for MPC approach. System force responses along three directions are represented separately. Blue, green and red curves represent compensation along X, Y and Z axis, respectively. During the first two seconds the system reaches the force references. Then, physiological motions are introduced along three directions. The control compensation is enabled only after 15.2 [s].

Robustness

To assess robustness of the control architecture, the environment stiffness K_s is deviated from its nominal[4] value.

To simulate the contact with different environment (fat tissues, bones or tools), the contact stiffness value represented by K_s is deviated from its nominal value 900 [N/m]. The figure 3.20 represents time responses

[4]In this context, "nominal" means the value used in control design ($\hat{K}_s$).

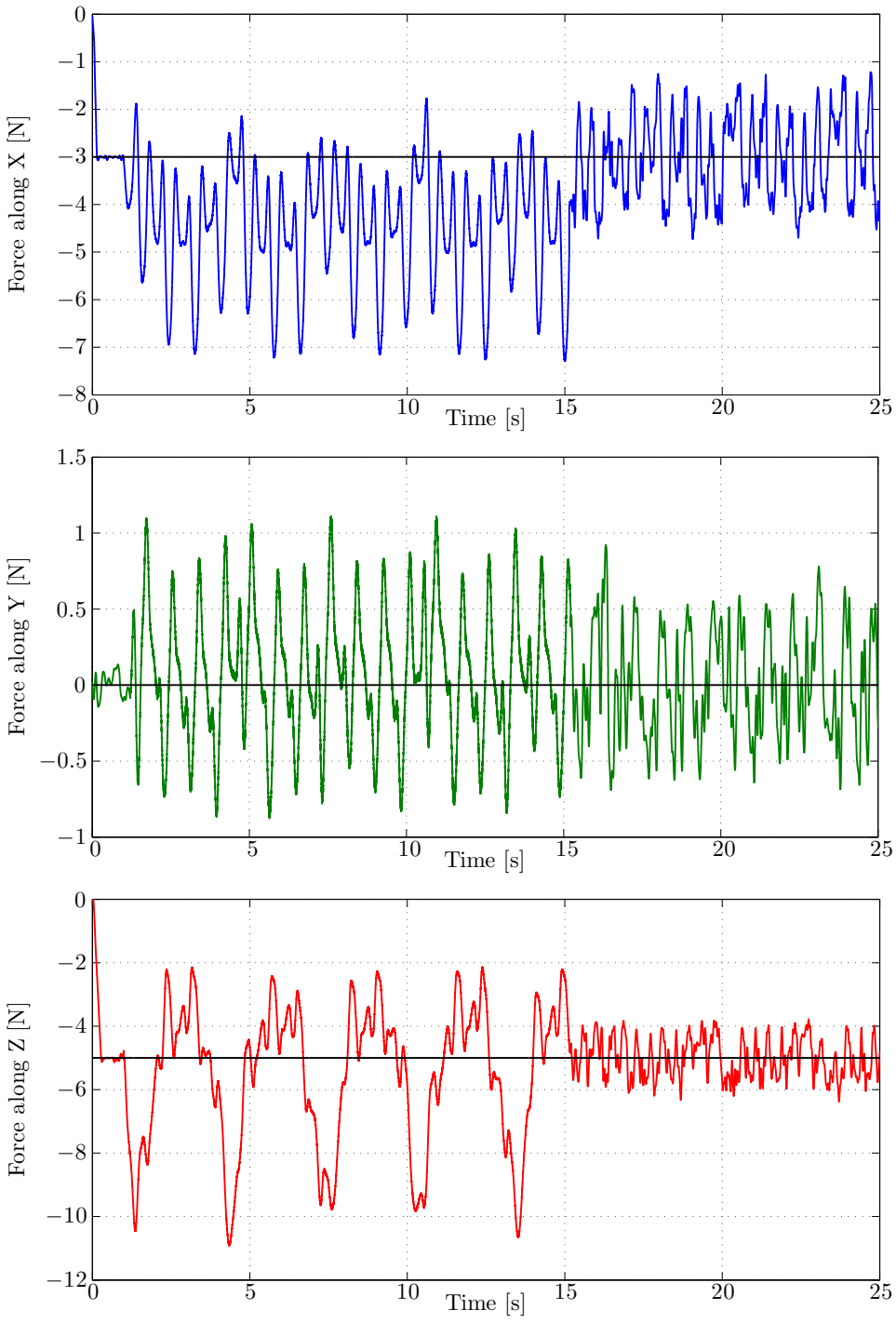

Figure 3.19: Experimental results for 3D heart motion compensation. MPC approach. Forces applied (along X, Y and Z directions) on an moving target for constant desired forces (-3 [N] for X axis, 0 [N] for Y axis and -5 [N] for Z axis).

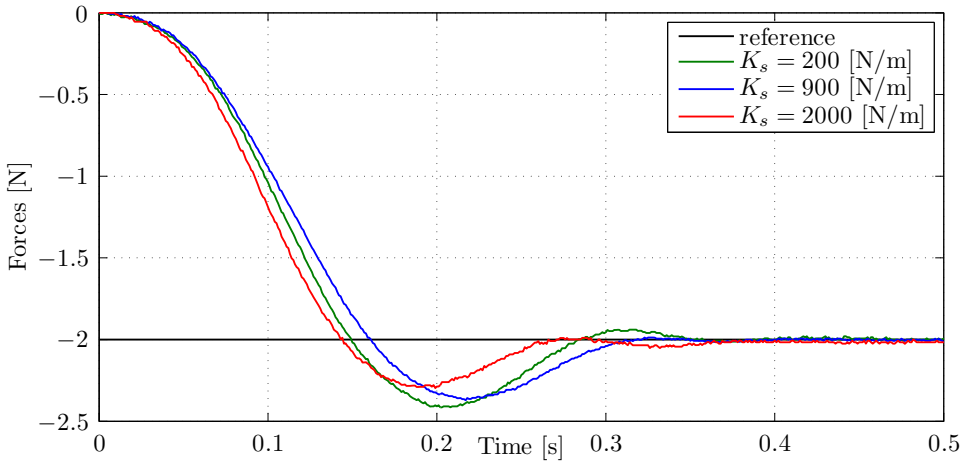

Figure 3.20: Experimental results for stiffness mismatches. MPC controller. System responses for a reference equal to -2 [N] with different environment stiffnesses K_s.

of the regulated system under internal disturbances. Black curve is the reference r_k, blue curve corresponds to the nominal system response (environment stiffness K_s equal to 900 [N/m]). Red and green curves are the system response with respectively an environment stiffness set alternatively to = 2000 [N/m] and to 200 [N/m].

Synthesis

Force responses under physiological motions (Fig. 3.19) show good motion compensation performances. Disturbance maximal amplitudes are reduced by 60% for X axis, 25% for Y axis and 72% for Z axis. Y axis low compensation ratio is explained by the physiological motion peak to peak amplitude which is less than 2 [N]. Corresponding position errors can be easily compute from these results. The environment model is a spring with a stiffness equal to K_s. Dividing forces responses by the stiffness $K_s = 900$ [N/m] gives position errors equivalence. The MPC approach deals perfectly with internal disturbances (Fig. 3.20). Force responses for stiffness mismatch cases (green and red curves) are closed to the nominal response (blue curve). Therefore, the control performance is slightly affected by environment interactions with different stiffnesses.

3.5.5 MPC conclusion

MPC approach has shown good complex motion compensation capabilities. However residual force amplitudes, around 4 [N], 1.5 [N] and 2 [N] for X, Y and Z axis respectively, are too high to consider this control architecture without further improvements. The robustness analysis has been performed for soft and hard environment stiffness mismatch scenarios. Experimental results highlight robustness capabilities of the MPC approach. The system is still stable with 220% environment stiffness mismatch, corresponding to a contact with a bone or a surgical tool.

3.6 Conclusion for AOB and MPC architectures

This chapter has presented a comparative study of two force control architectures for physiological motion compensation. According to the application domain (beating-heart surgery), physiological motion compensation capabilities and robustness of both controllers have been evaluated. The AOB and MPC approaches have shown good robustness and complex motion compensation capabilities. However, residual force amplitudes are too high to consider these control architectures without further improvements. All numerical results are summarized in the table (3.2).

The predictive control formulation is based on pulse response model. This approach requires an asymptotically stable plant. An internal loop will be included to stabilize the system. For the AOB approach, changing the stochastic design or increasing the AOB order, would improve compensation ratios. However, this introduces undesired behavior in the state estimate making it more sensor-based and more sensitive to noise. Introducing a second AOB to deal exclusively with external disturbances will allow to decouple motion compensation and control design [Cortesão and Poignet, 2009].

		AOB (F_d constant)	MPC (F_d constant)
X	*maximal [N]*	1.15	1.89
	RMS [N]	0.47	0.45
Y	*maximal [N]*	0.79	0.75
	RMS [N]	0.31	0.38
Z	*maximal [N]*	2.12	1.14
	RMS [N]	0.77	0.31

Table 3.2: Residual forces for AOB and MPC control architectures under physiological motions.

Chapter 4

Cascade force controllers in *ex vivo* environment

Contents

The whole is more than the sum of its parts.

Aristotle

Experimental results presented in the previous chapter have shown AOB and MPC architecture limits as independent controllers. For both approaches residual force amplitudes are too high and motion compensation capabilities can not be improve without affecting system stability or introducing undesired system behavior. Adding an extra loop to cope with external disturbances while the main loop deal with internal perturbations will allow to decouple motion compensation tuning from system robustness. From this idea we developed two cascade control architectures based on model predictive control and active observer techniques. Both dAOB (double AOB) and MPC-AOB controllers are built around an AOB main loop to deal with system disturbances due to modeling errors. A second loop is added to cope exclusively with heart motion perturbations. This extra loop is based on AOB design for dAOB approach and based on MPC method for MPC-AOB architecture.

We propose in this chapter an experimental comparative study of two cascade control architectures. The context of this study is cardiac surgery, especially compensation for external perturbations due to physiological motions (breathing and heartbeat). We focus our work on force control, to ensure that all efforts, due to the interaction between robot end-effector and its environment, are under control and needed.

Both dAOB and MPC-AOB cascade control approaches are presented. Their architectures detailed and designs explained. Then experimental evaluation results are presented. Experimental assessments of both cascade controllers are done with real environmental interactions.

4.1 Evaluation protocol

Force control architectures presented in this chapter are evaluated in the context of robotic assistance for beating heart surgery. The robotic platform used in the experiments is presented in Fig. 4.1. It is composed of a lightweight 4 DoF WAM robot used as a tool holder, a Heartbox and a 6 DoF JR3 force sensor (only the 3D Cartesian force is measured and filtered by a Kalman filter). The Heartbox is a 3 DoF robot used to reproduce 3D heart motion, where objects can be attached and used as targets. Cascade force controllers described in next sections are implemented on a 2.1 GHz Intel Core 2 processor running Xenomai-Linux. The communication to the WAM robot is performed by CAN bus. Integrity of the system is checked through real-time protection functions, such as maximum velocity, workspace limitation and maximum applied forces. The control sampling time T_s is set to 1 [ms]. The study is organized as follows. First, the force control architecture is presented and analyzed. Then, command law assessments are performed based on physiological motion compensation capabilities and environment stiffness mismatches. Finally, a result synthesis and a conclusion are performed.

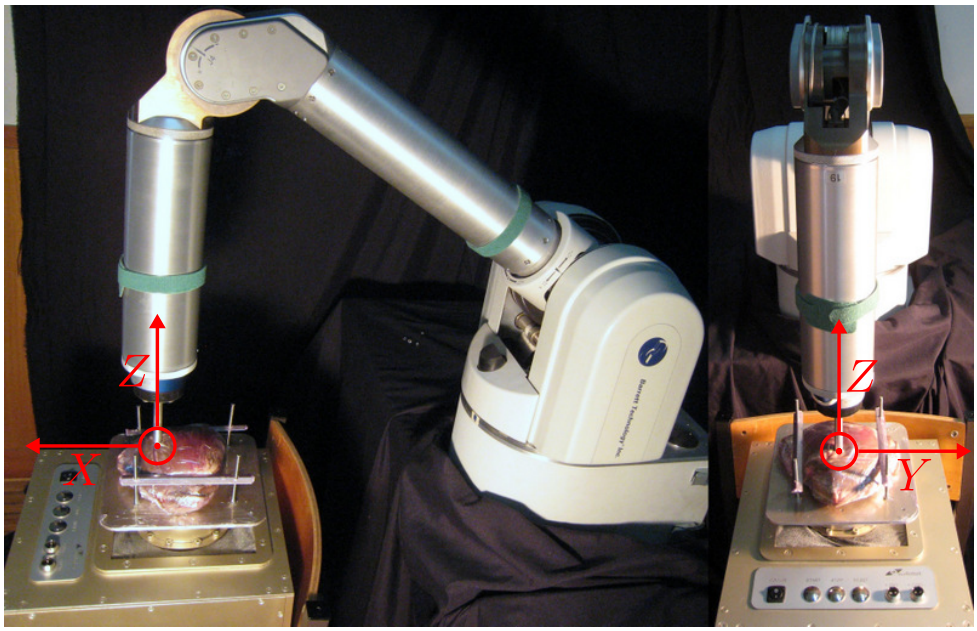

Figure 4.1: Two views of the experimental setup. A lightweight 4 DoF WAM robot from Barrett Technology equipped with a 6 DoF JR3 force sensor interacts with a 3 DoF robot (called Heartbox) that generates 3D beating heart motion. An *ex vivo* heart is attached to the Heartbox and used as target for the WAM robot.

Mathematical analysis A mathematical description of the control design is performed, giving an overview of implementation and setup procedures.

Rejection evaluation Respiration and heartbeats involve organ motions, introducing external system disturbances. To evaluate compensation capabilities, external perturbations representing physiological motions along three axes are generated by the Heartbox. Since pig and human cardiovascular systems are remarkably similar, including anatomic and physiologic characteristics [Swindle and Smith, 2008], Heartbox signals are based on physiological motion data recorded during *in vivo* experiments on a pig's heart [Sauvée et al., 2007] (shown in Fig. 3.12). The WAM robot applies surgical forces (desired forces) on the moving heart attached to the Heartbox, and the goal is to track them. The force references are constant and equal to 0 [N] for X and Y. For Z it is composed of positive and negative ramps followed by a sinusoid with increasing frequency from 0.2 [Hz] to 1 [Hz].

Robustness evaluation Robustness to stiffness mismatches of the control architecture is evaluated. The heart surface is composed of different tissues, such as fat, muscle, and arteries. During surgery the surgeon may interact not only with these tissues but also with surgical tools. Typical stiffness values for fat tissues are 300 [N/m]. The cardiac muscle (myocardium) ranges from 600 [N/m] to 1200 [N/m], and surgical tools (e.g., needle, stabilizer) have more than 1600 [N/m]. To assess robustness of the controller, the heart attached to the Heartbox is replaced by other objects, such as pillow and sponge. Off-line analysis have shown that pillow, heart and sponge stiffnesses are 375 [N/m], 810 [N/m] and 1900 [N/m], respectively.

Synthesis Experimental results with *ex vivo* environment are analyzed highlighting advantages and drawbacks of the evaluated controller.

4.2 Double active observer

Based on [Cortesão, 2003], [Cortesão et al., 2006] and [Cortesão, 2007] the active observer approach reformulates the Kalman filter to achieve a model reference adaptive control. An extra state is introduced to compensate system disturbances referred to the system input. A second AOB is added to the loop to exclusively deal with external disturbances. This dAOB architecture allows to decouple motion compensation and force control design. The first AOB guarantees desired closed-loop dynamics for the force, and the second AOB performs control actions to compensate physiological motions.

4.2.1 dAOB architecture

The AOB control architecture described in the previous chapter (see 3.4) has poor rejection capabilities under persistent physiological motions. Changing the stochastic design or increasing the AOB order, would improve rejection ratios, having however undesired implications in the state estimate, making it more sensor-based and more sensitive to noise. This fact motivated the insertion of an extra AOB to cope with physiological motions. The whole control architecture is shown in the figure 4.2.

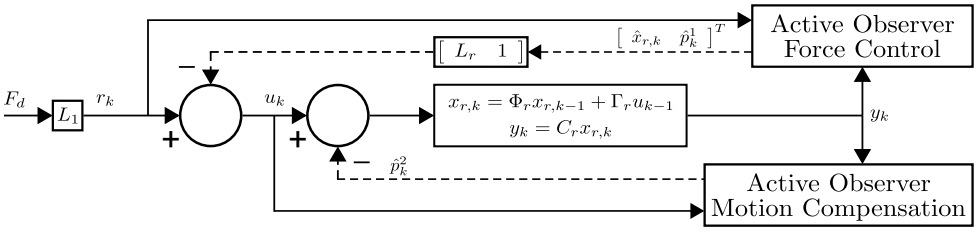

Figure 4.2: Double AOB control architecture. The estimated active states $\hat{p}_k^1$ and $\hat{p}_k^2$ enter as additional inputs to compensate respectively system disturbances and environment motions.

AOB for force control

As presented in section 3.4, from the open-loop system plant 3.19 and the desired closed-loop model 3.23, a state feedback control by Ackermann's method is used to imposed a desired dynamic and system behavior. The state feedback control strategy requires a completely observable system state. A Kalman filter is added into the architecture to estimate the system state. The Kalman filter is reformulated to introduce an extra state, called active state, which describes system disturbances due to

modeling errors referred to the system input. Its estimate is reinjected to the control command to perform a compensation action.

AOB for motion compensation

A second AOB is introduced into the loop to deal with external disturbances. Adding an AOB to exclusively deal with external disturbances allows to decouple motion compensation and control design. The AOB for motion compensation has no control actions besides the active state feedback p_k^2. The desired closed and open-loop dynamics are the same. Therefore, the control gains L_r for this AOB are zero. Physiological motions are often of periodic nature, being well described by second-order functions. A second-order AOB has been used ($N = 2$), entailing two states for the p_k^2 dynamics.

4.2.2 dAOB Design

A two-step procedure is used to tune both AOB parameters. In the first step, the AOB for force control loop is designed to guarantee a robust stable plant, assuring good force tracking performance. Then, the second AOB for motion compensation is tuned to compensate external force disturbances due to heart motion.

State feedback gain

State feedback control by Ackermann's method allows to imposed a desired dynamic and system behavior in closed-loop through its state feedback gain L_r. Equation 3.26 gives the relation between the feedback gain and the characteristic polynomial which describes the desired dynamic behavior

$$P\left(z\right) = z^2 + b_1 z + b_2 \tag{4.1}$$

with

$$b_1 = -2e^{\zeta w_n Ts} cos\left(\sqrt{1-\zeta^2} w_n Ts\right) \tag{4.2}$$

and

$$b_2 = e^{\zeta w_n Ts}, \tag{4.3}$$

ζ, w_n and Ts are respectively the damping factor, cut-off frequency (system bandwidth) and the sampling time.

AOB for force control

Noise matrices Q_k^1 and R_k^1, respectively on the system state and on the measurement, influence the Kalman Gain K_k^1. Their absolute values are

not important, only their relative relation is relevant for the Kalman gain. R_k^1 is set to 1. Decreasing Q_k^1 makes the system more sensor-based and more sensitive to noise. Increasing it makes the system more model-based.

Increasing the AOB order N allows the system to track non-linear disturbances but it decreases robustness to stiffness mismatches. A first order AOB ($N = 1$) gives good results for force control. p_k^1 is equal to

$$ {}^1p_k^1 = p_{k-1}^1 + {}^0\,\xi_{p_k^1} \tag{4.4} $$

and

$$ \Phi_{2,2} = 1. \tag{4.5} $$

The space state representation of the system is

$$ \begin{bmatrix} \hat{x}_{r,k} \\ {}^1\hat{p}_k^1 \end{bmatrix} = \begin{bmatrix} \Phi_r - \Gamma_r L_r & 0 \\ 0 & 1 \end{bmatrix} \begin{bmatrix} \hat{x}_{r,k-1} \\ \hat{p}_{k-1}^1 \end{bmatrix} + \begin{bmatrix} \Gamma_r \\ 0 \end{bmatrix} r_{k-1} + K_k^1 \left(y_k - \hat{y}_k \right) \tag{4.6} $$

with

$$ \hat{y}_k = C \left(\begin{bmatrix} \Phi_r - \Gamma_r L_r & 0 \\ 0 & 1 \end{bmatrix} \begin{bmatrix} \hat{x}_r \left(k-1 \right) \\ \hat{p}^1 \left(k-1 \right) \end{bmatrix} + \begin{bmatrix} \Gamma_r \\ 0 \end{bmatrix} r_{k-1} \right). \tag{4.7} $$

AOB for motion compensation

Same rules are used to tune noise matrices Q_k^2 and R_k^2 of the second AOB. Physiological motions are often of periodic nature, being well described by second-order functions. A second-order AOB has been used ($N = 2$), entailing two states for the p_k^2 dynamics

$$ {}^2p_k^2 = 2p_{k-1}^2 - p_{k-2}^2 + {}^1\,\xi_{p_k^2} \tag{4.8} $$

and

$$ \Phi_{2,2} = \begin{bmatrix} 0 & 1 \\ -1 & 1 \end{bmatrix}. \tag{4.9} $$

The space state representation of the whole system is

$$ \begin{bmatrix} \hat{x}_{r,k} \\ {}^2\hat{p}_k^2 \end{bmatrix} = \begin{bmatrix} \Phi_r - \Gamma_r L_r & 0 & 0 \\ 0 & 0 & 1 \\ 0 & -1 & 1 \end{bmatrix} \begin{bmatrix} \hat{x}_{r,k-1} \\ \hat{p}_{k-2}^2 \\ \hat{p}_{k-1}^2 \end{bmatrix} + \begin{bmatrix} \Gamma_r \\ 0 \\ 0 \end{bmatrix} r_{k-1} + K_k^2 \left(y_k - \hat{y}_k \right) \tag{4.10} $$

with

$$ \hat{y}_k = C \left(\begin{bmatrix} \Phi_r - \Gamma_r L_r & 0 & 0 \\ 0 & 0 & 1 \\ 0 & -1 & 1 \end{bmatrix} \begin{bmatrix} \hat{x}_r \left(k-1 \right) \\ \hat{p}^2 \left(k-2 \right) \\ \hat{p}^2 \left(k-1 \right) \end{bmatrix} + \begin{bmatrix} \Gamma_r \\ 0 \\ 0 \end{bmatrix} r \left(k-1 \right) \right). \tag{4.11} $$

4.2.3 Experimental evaluation

This section assesses experimental results based on heart motion compensation capabilities and environment stiffness mismatches. The dAOB control architecture is implemented on our experimental platform which is composed of the Heartbox robot equipped with an *ex vivo* heart reproducing heart motion and the WAM robot arm (tool holder) generating desired surgical forces on the moving heart. Parameter settings of the control architecture are given. Then experimental tests are presented and discussed. A conclusion highlights strong and weak points of the control architecture.

Parameter settings

The state feedback gain and stochastic parameters of the dAOB approach are tuned according to the dAOB design section.

State feedback control Critically damped behaviors are appropriate for force-based tasks, since they represent the fastest response without overshoot. Desired closed-loop dynamics for the force assigns the state feedback gain L_r

$$L_r = \begin{bmatrix} 161.5 & 1.189 & 0.557 \end{bmatrix}, \tag{4.12}$$

Force control The stochastic parameters reflect the model reference adaptive control strategy. R_k^1 is set to 1 and Q_k^1 (see (3.50)) is equal to

$$Q_{x_{r,k}}^1 = \begin{bmatrix} 10^{-10} & 0 & 0 \\ 0 & 10^{-12} & 0 \\ 0 & 0 & 10^{-12} \end{bmatrix} \tag{4.13}$$

and

$$Q_{1_{p_k}} = 0.5. \tag{4.14}$$

This design entails the AOB Kalman gain

$$K_{k,f} = \begin{bmatrix} 0.1236 & 8.145 & 0.662 & 0.662 \end{bmatrix}^T. \tag{4.15}$$

Motion compensation Noise matrices $Q_{x_{r,k}}^2$ and R_k^2 are equal to $Q_{x_{r,k}}^1$ and R_k^1, $Q_{2_{p_k}}^2$ is equal to

$$Q^2{}_{2_{p_k}} = \begin{bmatrix} 0 & 0 \\ 0 & 5 \end{bmatrix}. \tag{4.16}$$

This stochastic design entails the following Kalman gain

$$K_{k,m} = \begin{bmatrix} 0.3738 & 87.08 & 26.25 & 26.25 & 28.02 \end{bmatrix}^T. \tag{4.17}$$

3D Physiological motion compensation

To evaluate compensation capabilities of the dAOB architecture, respiration and heartbeat signals along three axes are generated by the Heartbox. The WAM robot applies forces on the moving heart attached to the Heartbox, and the goal is to track desired forces. 3D motion compensation results are shown in Fig. 4.3 for X, Y and Z. Blue, green and red curves in Fig 4.3(a) represent Heartbox motion seen by the WAM robot. The heart signals start at 5 [s] and are repeated around 20 [s] after a one second pause. Fig 4.3(b) shows desired (black curve) and applied forces (blue, green and red curves). The desired force is constant and equal to 0 [N] for X and Y, and for Z it is composed of positive and negative ramps followed by a sinusoid with increasing frequency from 0.2 [Hz] to 1 [Hz]. Residual forces are presented in Figs. 4.3(c), 4.3(d) and 4.3(e). Black curves in Figs. 4.3(c), 4.3(d) and 4.3(e) represent residual forces with the Heartbox turned off. A spectral analysis through the power spectral density (PSD) of both disturbance and residual force is presented in Fig 4.4. From the disturbance PSD Fig 4.4(a) the two main sources of perturbation can be identified: breathing and heartbeat. The first two peaks represent respiration and its harmonic (0.34 [Hz] and 0.72 [Hz]), corresponding to 20 breathing cycles per minute. The last five peaks are due to heartbeats (1.25 [Hz], 2.53 [Hz], 3.78 [Hz], 5.08 [Hz] and 6.32 [Hz]), which correspond to 75 heartbeats per minute.

Robustness

Our dAOB control architecture requires an approximate knowledge of the environment stiffness. We chose to set $\hat{K}_s = 900$ [N/m], which is the typical value of the myocardium stiffness.To assess robustness of the controller, the heart attached to the Heartbox is replaced by other objects, such as pillow and sponge. Off-line analysis have shown that pillow, heart and sponge stiffnesses are 290 [N/m], 980 [N/m] and 1900 [N/m], respectively. Fig 4.5 shows experimental results for stiffness mismatches under physiological motions for 3D constant reference forces. After reaching the references 0 [N] for X and Y, and -5.0 [N] for Z (around 1 [s]), the Heartbox is turned on. Blue, green and red curves represent force responses along X, Y and Z, respectively.

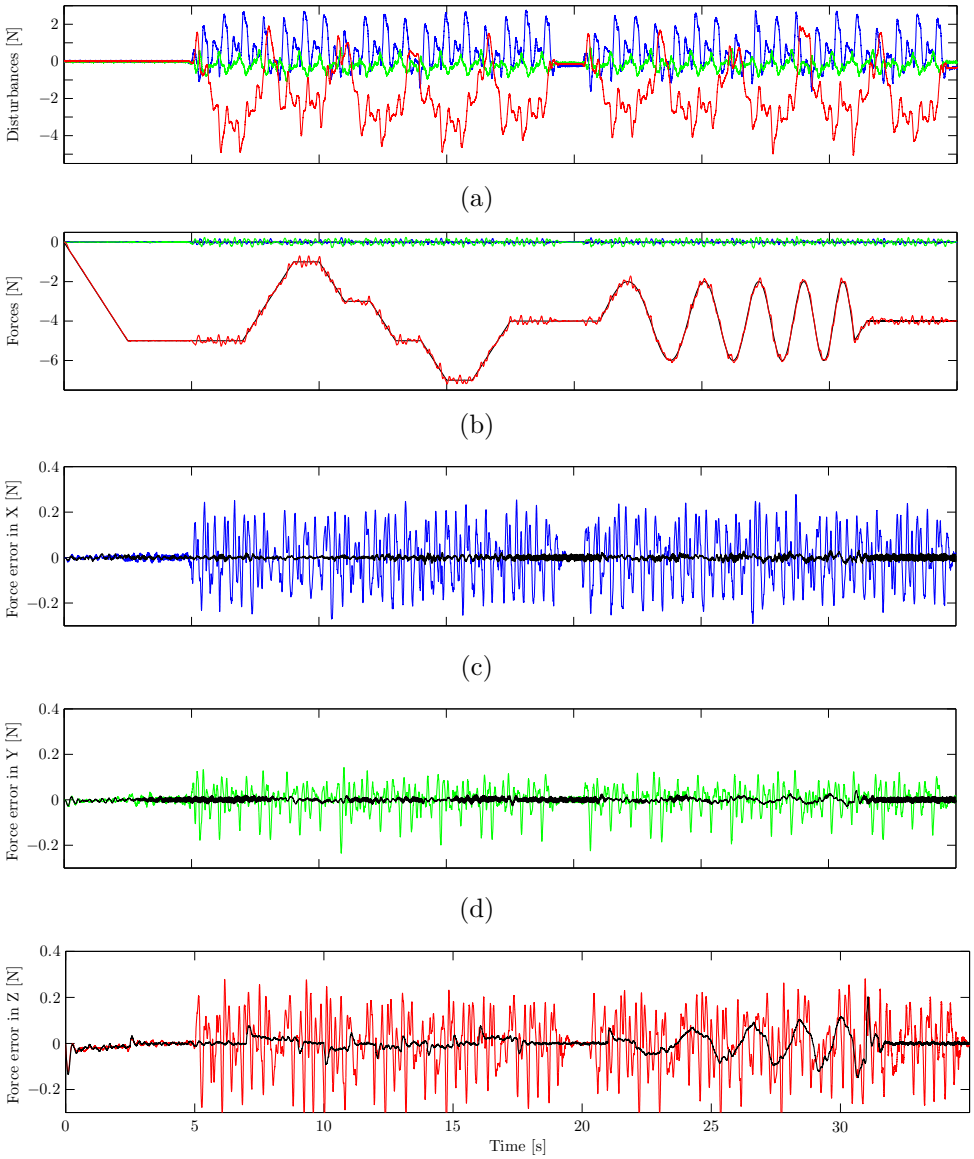

Figure 4.3: Experimental results for 3D heart motion compensation. dAOB approach. Blue, green and red curves represent, respectively X, Y and Z directions. (a) represents force disturbances induced by heart motion. (b) shows desired (black curves) and applied forces (colored curves). (c), (d) and (e) depict residual forces with the Heartbox turned on and off.

Synthesis

Force responses under physiological motions (Fig. 4.3) show excellent motion compensation performances. Disturbance maximal amplitudes are reduced by 87% for X axis, 80% for Y axis and 91% for Z axis. Maximal amplitudes of residual forces are around 0.30 [N] and the RMS values are around 0.09 [N] for all axis, which correspond to a maximal residual motion in the order of 0.35 [mm], considering a heart stiffness of 860 [N/m]. Comparing PSD signals of the cardiac disturbance (Fig. 4.4(a)) and the residual force (Fig. 4.4(b)), the compensation effect is obvious. Breathing and heartbeat spectral peaks are heavily reduced. Breathing and cardiac fundamental components are decreased by a factor of 140 and 14, respectively.

Stiffness mismatches degrade system performance, as expected, even though maximal and RMS amplitudes of the residual forces (pillow and sponge) are close to the nominal case (heart). Stronger high-frequency terms can be identified in force responses. Interacting with a stiffer environment (more than 1900 [N/m]) leads to instability. Decreasing the value of $Q_{p_k^2}$ improves system robustness and stability, but it degrades motion compensation capabilities.

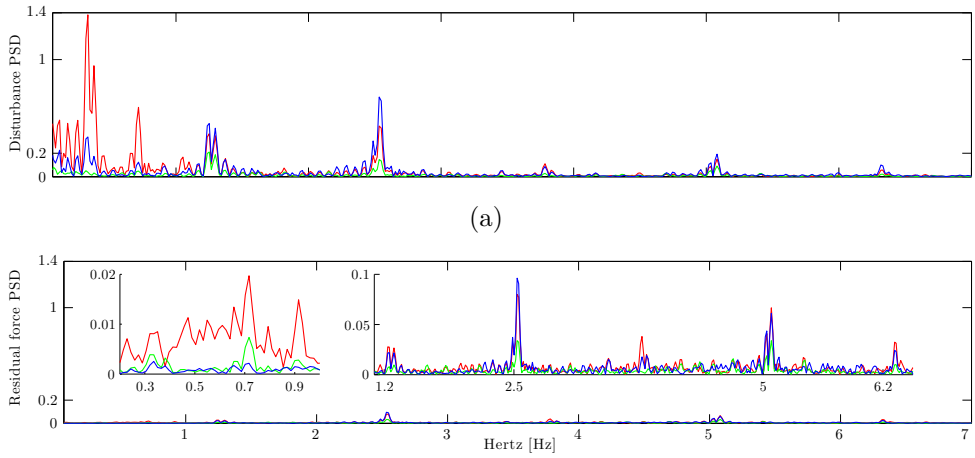

Figure 4.4: Power spectral density analysis of cardiac disturbance and residual force. Experimental results for dAOB approach. X, Y and Z directions are represented by blue, green and red curves, respectively. (a) represents PSD of the force disturbance seen by the WAM robot and induced by beating heart motion. (b) represents PSD of the residual force (i.e., force error). Two zoom views are shown highlighting major spectral peaks of the residual force.

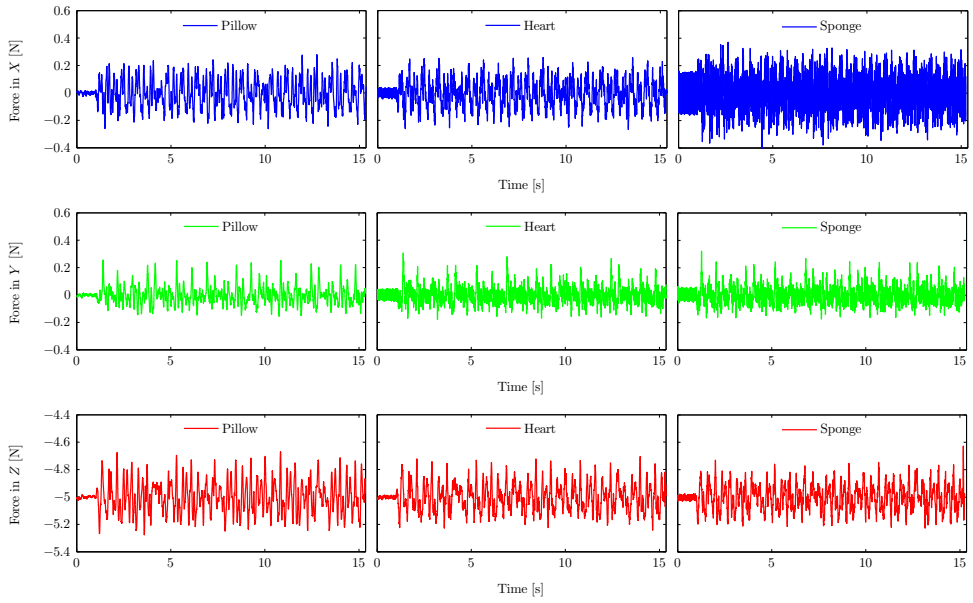

Figure 4.5: Experimental results for stiffness mismatches under physiological motions. dAOB controller. Force references are constant and equal to 0 [N] for X and Y, and -5.0 [N] for Z. Physiological motions are introduced at 1 [s] along the three Cartesian directions. Three experiments with environment stiffness equal to 290 [N/m], 980 [N/m] and 1900 [N/m] depending on the object fixed to the Heartbox: pillow, heart and sponge, respectively. In all experiments, the stiffness model of the control designed $\hat{K}_s = 900$ [N/m].

4.2.4 Conclusion

The single AOB approach presented in the chapter 3.4 has shown good performances for force control and good robustness capacities for modeling errors. But this approach is not able to compensate external perturbations [Dominici et al., 2011], residual force amplitudes are too high. Increasing AOB order or modifying the noise matrix $Q^1_{1_{p_k}}$ may improved the rejection at the expense of system stability. The dAOB approach adds a second AOB in the loop to exclusively deal with external disturbances. The motion compensation capabilities of the system are significantly increased. Maximal amplitudes of residual forces are 0.29 [N], 0.24 [N] and 0.36 [N] for X, Y and Z axis respectively. Considering a heart stiffness of 860 [N/m], corresponding residual motions are equal to 0.34 [mm], 0.28 [mm] and 0.42 [mm] for X, Y and Z axis respectively. Robustness analysis has been performed for under and over stiffness mismatches in the presence of heart motions. Results have shown good robustness capabilities, with stable behaviors up to 210% stiffness mismatches. But high frequency components in the force data indicate system behavior close to instability. Decreasing noise matrix $Q^2_{2_{p_k}}$ may improved the system stability at the expense of compensation capabilities. Therefore, an online stiffness adaptation of the $\hat{K}_s$ value is needed to have enough robustness to interact with hard contact.

4.3 Model predictive control - Active observer

Based on [Cortesão, 2007] the AOB approach reformulates the Kalman filter to achieve a model reference adaptive control. An extra state is introduced to compensate system disturbances referred to the system input. Applied to the robot system plant, the AOB loop guarantees desired closed-loop dynamics. The MPC structure described in [Dominici et al., 2009] is applied as a upper loop to this stable system loop. This MPC-AOB architecture allows to decouple motion compensation and robustness.

4.3.1 MPC-AOB architecture

The open-loop system plant $G_o l$ is an unstable system. Even if the MPC can deal with such plant, a stable plant is more robust to handle external disturbances (such as heart motion). Therefore the classical MPC approach is merged with the AOB design, described in the previous chapter (see section 3.4), into two cascade loops as shown in Fig. 4.6. An AOB inner-loop is designed to guarantee a well-defined stable plant. The MPC external loop, based on a model of this well-defined stable plant, predicts system behaviors and computes the control reference for the inner-loop. This cascade control architecture is called MPC-AOB.

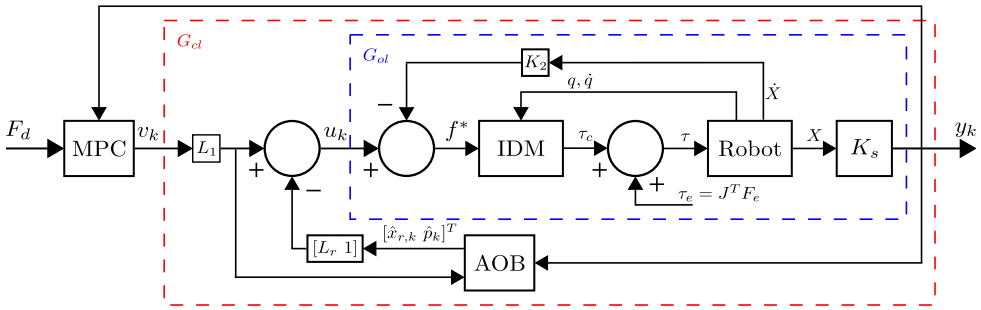

Figure 4.6: Cascade MPC-AOB force control architecture. Computed torque techniques linked with the robot inverse dynamics model (IDM) generate a decoupled and linearized system. The open-loop transfer function G_{ol} also takes into account a damping factor K_2 and the environment stiffness K_s. The desired closed-loop transfer function G_{cl} is obtained by the AOB architecture using the state-feedback gain L_r and the extra state $\hat{p}_k$. L_1 is the first element of L_r. The MPC generates a processed reference force v_k for AOB control, based on the desired force F_d, the measured force y_k and G_{cl}. The external torque τ_e is mainly due to beating heart disturbances.

AOB for stable plant

As presented in section 3.4, from the open-loop system plant G_{ol} (3.19) and the desired closed-loop model G_{cl} (3.23), a state feedback control by Ackermann's method is used to imposed a desired dynamic and system behavior. The state feedback control strategy requires a completely observable system state. A Kalman filter is added into the architecture to estimate the system state. The Kalman filter is reformulated to introduce an extra state, called active state, which describes system disturbances due to modeling errors referred to the system input. Its estimate is reinjected to the control command to perform a compensation action.

MPC for motion compensation

The MPC control loop described in section 3.5 is a applied to the G_cl loop as a master loop. Based on the model of this well-defined stable plant G_{cl}, MPC controller predicts system behaviors and computes the control reference for the AOB inner-loop.

4.3.2 Tuning

A two-step procedure is used to tune AOB and MPC parameters. In the first step, the AOB controller is designed to guarantee a robust stable plant, assuring good force tracking performance. Then, the MPC based on the model of this stable plant, is tuned to compensate external force disturbances due to heart motion.

4.3.3 Experimental evaluation

This section assesses experimental results based on heart motion compensation capabilities and environment stiffness mismatches. The MPC-AOB control architecture is implemented on our experimental platform which is composed of the Heartbox robot equipped with an *ex vivo* heart reproducing heart motion and the WAM robot arm (tool holder) generating desired surgical forces on the moving heart. Parameter settings of the control architecture are given. Then experimental tests are presented and discussed. A conclusion highlights strong and weak points of the control architecture.

Parameter settings

According to the MPC-AOB design section parameter tuning is a two-step procedure. First the state feedback gain and stochastic parameters

of the AOB loop. Then MPC parameters.

AOB Design Critically damped behaviors are appropriate for force-based tasks, since they represent the fastest response without overshoot. For a desired contact model $\hat{K}_s = 900$ [N/m], a damping $K_2 = 10$, and a desired G_{cl}[1] given by (3.23) with $T_{cl} = 3$ [ms], the following state feedback gain

$$L_r = \begin{bmatrix} 161.5 & 1.189 & 0.557 \end{bmatrix} \tag{4.18}$$

is obtained. This T_{cl} entails a control bandwidth of about 34 [Hz], which is more than enough to track cardiac disturbance. The stochastic parameters reflect the model reference adaptive control strategy, where the uncertainties are lumped in p_k. R_k is set to 1 and Q_k is given by

$$Q_{x_{r,k}} = \begin{bmatrix} 10^{-12} & 0 & 0 \\ 0 & 10^{-12} & 0 \\ 0 & 0 & 10^{-12} \end{bmatrix} \tag{4.19}$$

and

$$Q_{p_k} = 0.5 \ . \tag{4.20}$$

This stochastic design entails the AOB Kalman gain

$$K_{k,f} = \begin{bmatrix} 0.1236 & 8.145 & 0.662 & 0.662 \end{bmatrix}^T . \tag{4.21}$$

MPC Design The length of the prediction horizon H_p greatly influences control tracking capabilities. Extending H_p, a more accurate system is achieved but the computational time increases. Since our control sampling time is $T_s = 1$ [ms], a good trade-off is achieved with $H_p = 30$ and $H_u = 5$. The optimal command $\Delta\tilde{u}_{k+i|i=0}$ is computed by minimizing the cost function W, with

$$\lambda = 0.1 I_u \tag{4.22}$$

and

$$\delta = 0.9 I_p, \tag{4.23}$$

where I_u and I_p are identity matrices of size H_u and H_p, respectively.

3D Physiological motion compensation

To evaluate compensation capabilities of the MPC-AOB architecture, respiration and heartbeat signals along three axes are generated by the Heartbox. The WAM robot applies forces on the moving heart attached

[1] Time delay has been neglected

to the Heartbox, and the goal is to track desired forces. 3D motion compensation results are shown in Fig. 4.7 for X, Y and Z. Blue, green and red curves in Fig 4.7(a) represent Heartbox motion seen by the WAM robot. The heart signals start at 5 [s] and are repeated for around 20 [s] after a one second pause. Fig 4.7(b) shows desired (black curve) and applied forces (blue, green and red curves). The desired force is constant and equal to 0 [N] for X and Y, and for Z it is composed of positive and negative ramps followed by a sinusoid with increasing frequency from 0.2 [Hz] to 1 [Hz]. Residual forces are presented in Figs. 4.7(c), 4.7(d) and 4.7(e).Black curves in Figs. 4.7(c), 4.7(d) and 4.7(e) represent residual forces with the Heartbox turned off. A spectral analysis through the power spectral density (PSD) of both disturbance and residual force is presented in Fig 4.8. From the disturbance PSD Fig 4.8(a) the two main sources of perturbation can be identified: breathing and heartbeat. The first two peaks represent respiration and its harmonic (0.34 [Hz] and 0.72 [Hz]), corresponding to 20 breathing cycles per minute. The last five peaks are due to heartbeats (1.25 [Hz], 2.53 [Hz], 3.78 [Hz], 5.08 [Hz] and 6.32 [Hz]), which correspond to 75 heartbeats per minute.

Robustness

Our cascade MPC-AOB control architecture requires an approximate knowledge of the myocardium stiffness (see $\hat{K}_s$ in (3.19)), which is set to $\hat{K}_s = 900$ [N/m]. To assess robustness of the controller, the heart attached to the Heartbox is replaced by other objects, such as pillow and sponge. Off-line analysis have shown that pillow, heart and sponge stiffnesses are 375 [N/m], 900 [N/m] and 1800 [N/m], respectively. Fig 4.9 shows experimental results for stiffness mismatches under physiological motions for 3D constant force references. After reaching the references 0 [N] for X and Y, and -5.0 [N] for Z (around 1 [s]), the Heartbox is turned on. Blue, green and red curves represent force responses along X, Y and Z, respectively.

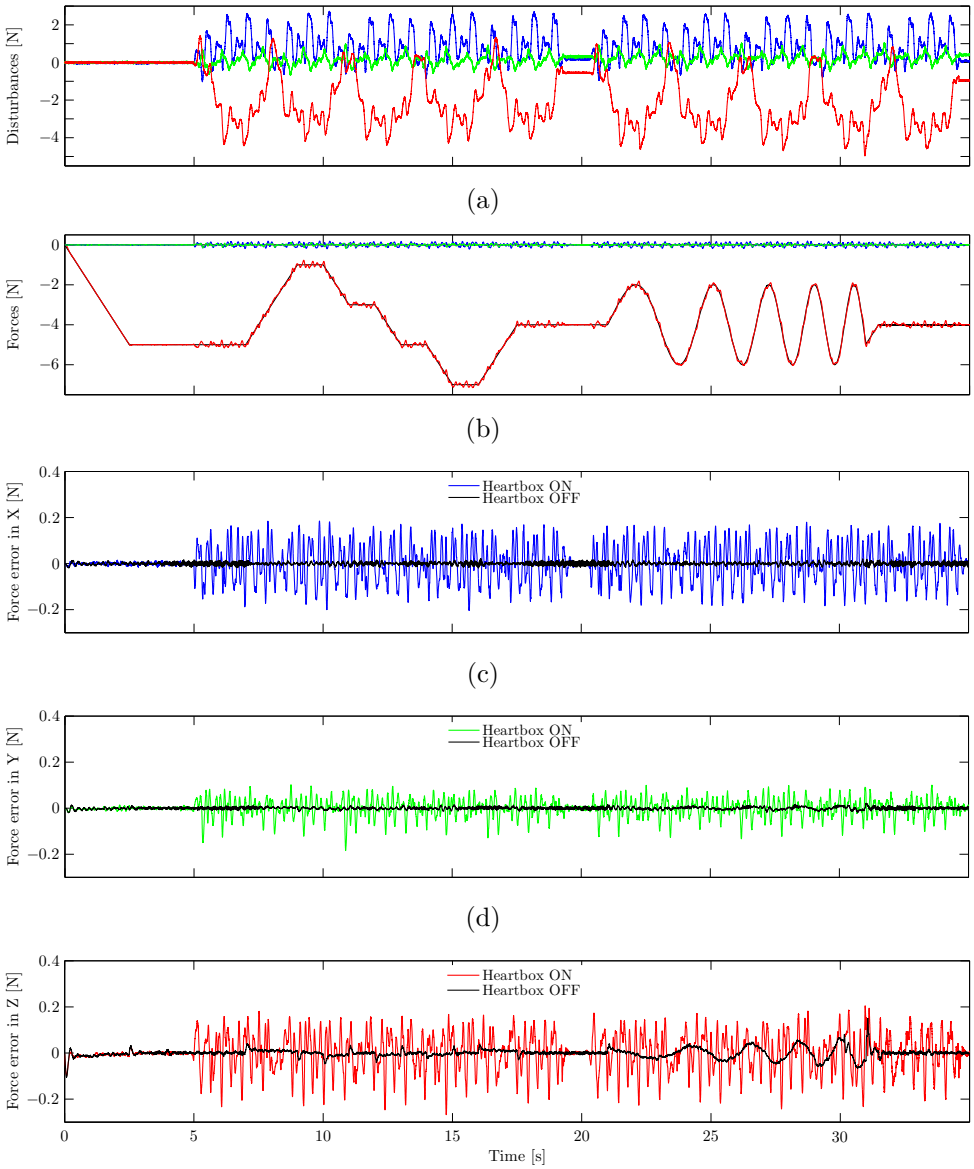

Figure 4.7: Experimental results for 3D heart motion compensation. MPC-AOB approach. Blue, green and red curves represent, respectively X, Y and Z directions. (a) represents force disturbances induced by heart motion. (b) shows desired (black curves) and applied forces (colored curves). (c), (d) and (e) depict residual forces with the Heartbox turned on and off.

Synthesis

Force responses under physiological motions (Fig. 4.7) show excellent motion compensation performances. Disturbance maximal amplitudes are reduced by 90% for X axis, 84% for Y axis and 93% for Z axis. Maximal amplitudes of residual forces are around 0.22 [N] and the RMS values are around 0.06 [N] for all axis, which correspond to residual motions in the order of 0.27 [mm], considering a heart stiffness of 810 [N/m]. Comparing PSD signals of the cardiac disturbance (Fig. 4.8(a)) and the residual force (Fig. 4.8(b)), the compensation effect is obvious. Breathing and heartbeat spectral peaks are heavily reduced. Breathing and cardiac fundamental components are decreased by a factor of 200 and 20, respectively.

Maximal amplitudes of the residual forces and corresponding RMS values are not really affected by stiffness mismatches, but the increase of high frequency terms for the stiffer case can be clearly seen at the beginning (see Fig 4.9 during the first second, before turning on the Heartbox). Stiffer environments get unstable. Decreasing the value of δ improves system robustness and stability, but it degrades motion compensation capabilities.

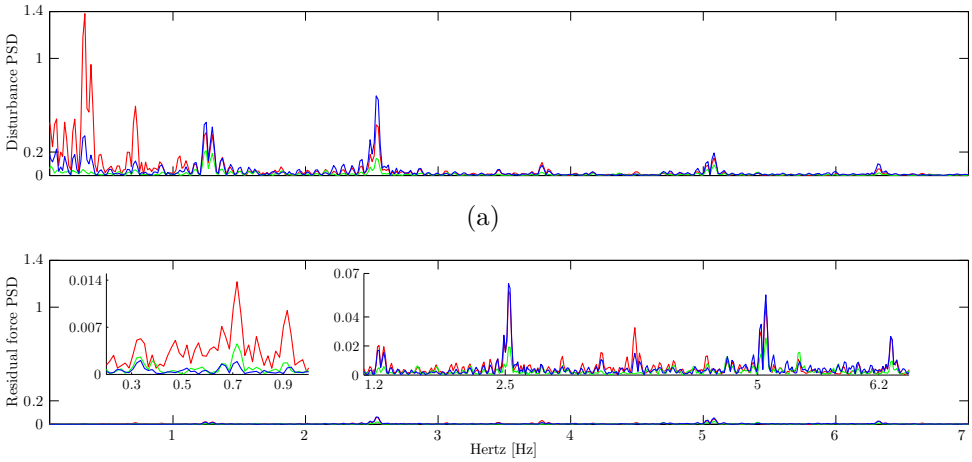

Figure 4.8: Power spectral density analysis of cardiac disturbance and residual force. Experimental results for MPC-AOB approach. X, Y and Z directions are represented by blue, green and red curves, respectively. (a) represents PSD of the force disturbance seen by the WAM robot and induced by beating heart motion. (b) represents PSD of the residual force (i.e., force error). Two zoom views are shown highlighting major spectral peaks of the residual force.

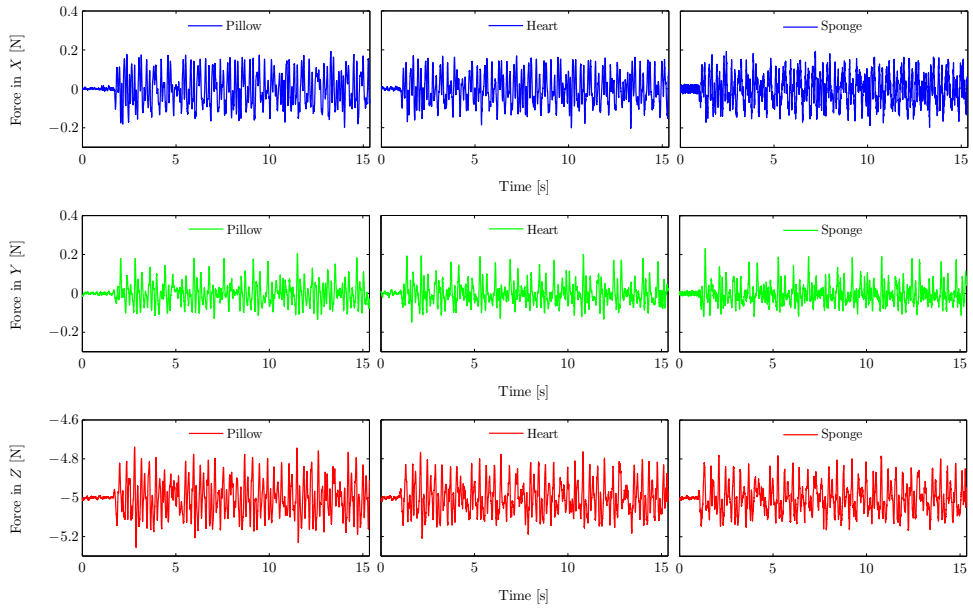

Figure 4.9: [Experimental results for stiffness mismatches under physiological motions. MPC-AOB controller]. Force references are constant and equal to 0 [N] for X and Y, and -5.0 [N] for Z. Physiological motions are introduced at 1 [s] along the three Cartesian directions. Three experiments with environment stiffness equal to 375 [N/m], 900 [N/m] and 1800 [N/m] depending on the object fixed to the Heartbox: pillow, heart and sponge, respectively. In all experiments, the control design assumes a stiffness of $\hat{K}_s = 900$ [N/m].

4.3.4 Conclusion

The MPC approach presented in the chapter 3.5 has shown good performances for motion compensation and good robustness capacities for modeling errors. But residual force amplitudes are too high this approach to consider this control architecture without improvements [Dominici et al., 2011]. Since the system plant is asymptotically unstable an AOB loop is introduced as inner-loop to imposes stable closed-loop dynamics. Then the MPC controller drives the AOB loop by generating force references. The motion compensation capabilities of the system are significantly increased. Maximal amplitudes of residual forces are 0.20 [N], 0.18 [N] and 0.27 [N] for X, Y and Z axis respectively. Considering a heart stiffness of 810 [N/m], corresponding residual motions are equal to 0.25 [mm], 0.22 [mm] and 0.33 [mm] for X, Y and Z axis respectively. Robustness analysis has been performed for under and over stiffness mismatches in the presence of heart motions. Results have shown excellent robustness capabilities, with stable behaviors up to 200% stiffness mismatches. But high frequency components in the force data indicate system behavior closed to instability. Decreasing the value of δ improves system robustness and stability, but it degrades motion compensation capabilities. Therefore, an online stiffness adaptation of the $\hat{K}_s$ value is needed to have enough robustness to interact with hard contact.

4.4 Conclusion for cascade controllers

This chapter has presented a comparative study of two cascade force control architectures for physiological motion compensation. According to the application domain (beating heart surgery), physiological motion compensation capabilities and robustness of both controllers have been evaluated. Decoupling system robustness from the compensation functionality greatly increase overall performances. All numerical results are summarized in tables (4.1), (4.2) and (4.3). Both cascade dAOB and MPC-AOB control architectures have shown excellent complex motion compensation capabilities even under high stiffness mismatches. However high frequency components in the force response of both controllers indicate a system behavior close to instability. Stability can be increased at the expense of motion compensation performances. Therefore, an online stiffness adaptation of the $\hat{K}_s$ value is needed to have enough robustness to interact with hard contact.

		dAOB (F_d variable)	MPC-AOB (F_d variable)
X	*maximal [N]*	0.29	0.20
	RMS [N]	0.10	0.07
Y	*maximal [N]*	0.24	0.18
	RMS [N]	0.05	0.04
Z	*maximal [N]*	0.36	0.27
	RMS [N]	0.11	0.08

Table 4.1: Residual forces for dAOB and MPC-AOB control architectures under physiological motions.

dAOB (F_d constant)		Pillow (290 [N/m])	Heart (980 [N/m])	Foam (1900 [N/m])
X	*maximal [N]*	0.28	0.27	0.40
	RMS [N]	0.11	0.10	0.14
Y	*maximal [N]*	0.25	0.31	0.32
	RMS [N]	0.07	0.07	0.07
Z	*maximal [N]*	0.33	0.29	0.37
	RMS [N]	0.12	0.10	0.09

Table 4.2: Residual forces for dAOB control architecture under physiological motions and stiffness mismatches.

MPC-AOB (F_d constant)		Pillow (375 [N/m])	Heart (900 [N/m])	Foam (1800 [N/m])
X	*maximal [N]*	0.20	0.20	0.20
	RMS [N]	0.08	0.08	0.07
Y	*maximal [N]*	0.20	0.20	0.23
	RMS [N]	0.06	0.056	0.05
Z	*maximal [N]*	0.26	0.24	0.22
	RMS [N]	0.09	0.08	0.08

Table 4.3: Residual forces for MPC-AOB control architecture under physiological motions and stiffness mismatches.

Chapter 5

Conclusion

Contents

Un homme sage ne croit que la moitié de ce qu'il lit. Plus sage encore, il sait laquelle

Unkown

Cardiovascular diseases are the first cause of mortality in the world. To reduce patient's risk of death, heart surgeries are common procedures. Most of surgical interventions require a cardiopulmonary bypass, where heart and lung functionalities are performed by an extracorporeal machine. Complications and post-operatory mortality involved by the use of heart-lung machine have motivated the beating heart surgery. Heartbeats and respiration are the two main sources of disturbances during off-pump surgeries. Respiration yields large cyclic displacements and heartbeat motions involve high acceleration displacements. The sum of both is very disturbing for the surgeon and manual tracking cannot be achieved. Robotic assistance has the potential to offer significant improvements to the medical practice in terms of precision, safety and comfort. The *da Vinci* surgical system, the most popular and sophisticated surgical platform, has considerably improved dexterity, precision and safety. But this robotic system does not provide solutions for restoring tactile feedback to the surgeon and physiological motions still need to be manually compensated by the surgeon.

The work presented in this thesis was focused on autonomous motion compensation. New control architectures have been designed based on force feedback and evaluated through *ex vivo* experiments. This chapter is divided in two sections. First an overall conclusion highlights performances and capabilities of our cascade control architectures. Then in second time, future works is presented.

5.1 General conclusion

The work presented was focused on the problem of autonomous motion compensation for robotic assistance in beating heart surgery. Two advanced control designs based on AOB and MPC techniques have been presented and analyzed. Heart motion compensation capabilities and robustness to stiffness mismatches have been evaluated through experimental assessments. Both controllers have shown good performances for force control under external perturbations. However residual force amplitudes were too high to consider these control architectures without improvements. The robustness analysis performed for soft and hard environment stiffness mismatch scenarios has highlighted robustness capabilities of both approaches. Nevertheless high frequency components, in AOB controller force responses, has indicated a system behavior close to instability for a contact with a bone or a surgical tool.

Since motion compensation performances of both controllers could not be improved without introducing system instability, we developed two new cascade control architectures: the dAOB and the MPC-AOB. The idea was to decouple robustness to internal disturbances due to modeling errors from compensation of external perturbations. The dAOB and MPC-AOB controllers have been built around an AOB main loop to deal with system disturbances. A second loop has been added to cope exclusively with heart motion perturbations. This extra loop is based on AOB design for the dAOB approach and based on MPC method for the MPC-AOB architecture. Both cascade control approaches have been presented, their architectures detailed and their designs explained. Experimental assessments have been performed through a realistic scenario. A Heartbox robot equipped with an *ex vivo* heart reproduces heart motion and a robot arm generates desired surgical forces on the moving heart. Additionally, robustness analysis has been performed for several stiffness mismatches, by using sponge and pillow as targets, in the presence of heart motions.

High quality results have been achieved. Both cascade dAOB and MPC-AOB control architectures have shown excellent complex motion compensation capabilities even under high stiffness mismatches. Residual forces are smaller than any results in the scientific literature and have been attained without *a priori* knowledge of heart motion.

5.2 Perspectives

The main goal of this work was to develop a force control architecture which have autonomous 3D compensation capabilities of disturbances due to cardiac and breathing motions, while tracking time varying surgical force references. The challenge was to use no *a priori* information about these disturbances, relying the control actions on measured forces and on a generic/ simple contact model. Two force control architectures have been developed and experimentally evaluated through realistic scenarios. Physiological motion compensation performances of both controllers are far away better than any results in the literature.

Assessments to stiffness mismatches have shown a high quality robustness to internal disturbances. However high frequency components in the force response for both controllers indicate a system behavior closed to instability for a contact with a bone or a surgical tool. This is a first improvement which can be done in a future work, an online stiffness adaptation of the $\hat{K}_s$ value to allow interaction with hard target.

Both control architectures are based on force feedback and they require a permanent contact with the target. Such an assumption is problematic and can not be respected during the whole surgical act: during free-space phase, for example, the system can not achieve motion compensation. Adding to the experimental platform a vision system could feedback the control system with another source of data and allow motion compensation without contact. This is a second improvement which could be done.

Desired forces used for experimental tests, realized in this work, were generated by some mathematical functions. A third improvement could be to complete the experimental setup with a phantom device which is a manipulation interface for the surgeon. From surgeon's gestures force trajectory references can be generated and interaction forces could provide the haptic feedback for him.

Merging autonomous motion compensation techniques with a hybrid force/vision controller, an haptic feedback and an online stiffness estimation could provide a fully operational teleoperated surgical platform.

Bibliography

[Bachta et al., 2011] Bachta, W., Renaud, P., Laroche, E., Forgione, A., and Gangloff, J. (2011). Active stabilization for robotized beating heart surgery. *IEEE Transactions on Robotics*, 27(4):757–768.

[Bebek and Çavuşoğlu, 2007] Bebek, O. and Çavuşoğlu, M. C. (2007). Intelligent control algorithms for robotic assisted beating heart surgery. *IEEE Transactions on Robotics*, 23:468–480.

[Berdat et al., 2004] Berdat, P. A., Muller, J. S. K., Kipfer, B., Eckstein, F., Immer, F. F., and Carrel, T. (2004). Totally arterial off-pump vs. on-pump coronary revascularization : comparison of early outcome. *Interactive Cardiovascular and Thoracic Surgery*, 3:176–181.

[Bowthorpe and Tavakoli, 2016] Bowthorpe, M. and Tavakoli, M. (2016). Physiological organ motion prediction and compensation based on multi-rate, delayed, and unregistered measurements in robot-assisted surgery and therapy. *IEEE/ASME Transactions on Mechatronics*.

[Boyd et al., 1999] Boyd, W. D., Desai, N. D., Rizzo, D. F. D., Novick, R. J., McKenzie, F. N., and Menkis, A. H. (1999). Off-pump surgery decreases post-operative complications and resource utilization in the elderly. In *Annals of Thoracic Surgery*, volume 68, pages 1490–1493.

[Cagneau et al., 2007] Cagneau, B., Zemiti, N., Bellot, D., and Morel, G. (2007). Physiological motion compensation in robotized surgery using force feedback control. In *Proc. of the IEEE Int. Conf. on Robotics and Automation (ICRA)*, pages 1881–1886, Roma, Italy.

[Camacho and Bordons, 2004] Camacho, E. F. and Bordons, C. (2004). *Model predictive control*. Springer-Verlag, first edition.

[Choi et al., 2001] Choi, S., Lee, S., and Won, S. (2001). Development of a new variable remote center compliance using stiffness adjusters. In *Proc. of the IEEE Int. Conf. on Intelligent Robots and Systems (IROS)*, volume 4, pages 1860–1863, Maui, USA.

[Cortesão, 2003] Cortesão, R. (2003). *Kalman Techniques for Intelligent Control Systems: Theory and Robotic Experiments*. Phd thesis, University of Coimbra, Coimbra, Portugal.

[Cortesão, 2007] Cortesão, R. (2007). On kalman active observers. *Journal of Intelligent and Robotic Systems*, 48:131–155.

[Cortesão et al., 2006] Cortesão, R., Park, J., and Khatib, O. (2006). Real time adaptive control for haptic telemanipulation with kalman active observers. *IEEE Transactions on Robotics*, 22(5):987–999.

[Cortesão and Poignet, 2009] Cortesão, R. and Poignet, P. (2009). Motion compensation for robotic-assisted surgery with force feedback. In *Proc. of the IEEE Int. Conf. on Robotics and Automation (ICRA)*, pages 3464,3469, Kobe, Japan.

[Cuvillon et al., 2005] Cuvillon, L., Gangloff, J., de Mathelin, M., and Forgione, A. (2005). Toward robotized beating heart tecabg : assessment of the heart dynamics using high-speed vision. In *Proc. of the Int. Conf. on Medical Image Computing and Computer-Assisted Intervention (MICCAI)*, Palm Springs, USA.

[de Schutter and van Brussel, 1988] de Schutter, J. and van Brussel, H. (1988). Compliant robot motion ii. a control approach based on external control loops. *The Int. J. of Robotics Research*, 7:18–33.

[Dominici and Cortesão, 2014a] Dominici, M. and Cortesão, R. (2014a). Cascade robot force control architecture for autonomous beating heart motion compensation with model predictive control and active observer. In *Proc. of the IEEE Int. Conf. on Biomedical Robotics and Biomechatronics (BIOROB)*, pages 745–751, São Paulo, Brazil.

[Dominici and Cortesão, 2014b] Dominici, M. and Cortesão, R. (2014b). Model predictive control architectures with force feedback for robotic-assisted beating heart surgery. In *Proc. of the IEEE Int. Conf. on Robotics and Automation (ICRA)*, pages 2276 – 2282, São Paulo, Brazil.

[Dominici and Cortesão, 2015] Dominici, M. and Cortesão, R. (2015). Cascade force control for autonomous beating heart motion compensation. *Control Engineering Practice*, 37:80 – 88.

[Dominici et al., 2011] Dominici, M., Cortesão, R., and Sousa, C. (2011). Heart motion compensation for robotic-assisted surgery predictive approach vs. active observer. In *Proc. of the IEEE Int. Conf. on Robotics and Automation (ICRA)*, pages 6252–6257, Shanghai, China.

[Dominici et al., 2009] Dominici, M., Poignet, P., Cortesão, R., Dombre, E., and Tempier, O. (2009). Compensation for 3D physiological motion in robotic-assisted surgery using a predictive force controller. experimental results. In *Proc. of the IEEE Int. Conf. on Intelligent Robots and Systems (IROS)*, pages 2634–2639, St Louis, USA.

[Dominici et al., 2008] Dominici, M., Poignet, P., and Dombre, E. (2008). Compensation of physiological motion using linear predictive force control. In *Proc. of the IEEE Int. Conf. on Intelligent Robots and Systems (IROS)*, pages 1173–1178, Nice, France.

[Dzwonczyk et al., 2005] Dzwonczyk, R., del Rio, C., Sun, B., Michler, R., and Howie, M. (2005). Devices used to expose the posterior coronary artery in opcabg surgery may cause ischemia. In *Proceedings of the 31th Bioengineering conference*, volume 2-3, pages 148–149.

[Eagle and Guyton, 2004] Eagle, K. A. and Guyton, R. A. (2004). Acc/aha 2004 guideline update for coronary artery bypass graft surgery. Reseach report, American College of Cardiology/American Heart Association.

[Falk, 2002] Falk, V. (2002). Manual control and tracking-a human factor analysis relevant for beating heart surgery. *The Annals of Thoracic Surgery*, 74:624–628.

[Fisher and Mujtaba, 1992] Fisher, W. D. and Mujtaba, M. S. (1992). Hybrid position/force control: a correct formulation. *Int. J. Rob. Res.*, 11(4):299–311.

[Gagne et al., 2012] Gagne, J., Laroche, E., Piccin, O., and Gangloff, J. (2012). Gyrolock: Stabilizing the heart with control moment gyroscope (cmg) - from concept to first in vivo assessments. *IEEE Transactions on Robotics*, 28(4):942–954.

[Ginhoux et al., 2005] Ginhoux, R., Gangloff, J., de Mathelin, M., Soler, L., Sanchez, M. M. A., and Marescaux, J. (2005). Active filtering of physiological motion in robotized surgery using predictive control. *IEEE Transactions on Robotics*, 21(1):67–79.

[Hogan, 1985] Hogan, N. (1985). Impedance control - an approach to manipulation. i - theory. ii - implementation. iii - applications. *Trans. of the ASME, J. of Dynamic Systems, Measurement, and Control*, 107:1–24.

[Jacobs et al., 2003] Jacobs, S., Holzhey, D., Mohr, F. W., and Falk, V. (2003). Limitations for manual and telemanipulator-assisted motion

tracking and dexterity for endoscopic surgery. In *Proc. of the Int. Conf. on Computer Assisted Radiology and Surgery (CARS)*, pages 673–677.

[Kappert et al., 2001] Kappert, U., Cichon, R., Schneider, J., Gulielmos, V., Ahmadzade, T., Nicolai, J., Tugtekin, S.-M., and Schueler, S. (2001). Technique of closed chest coronary artery surgery on the beating heart. *European Journal of Cardio-Thoracic Surgery*, 20:765–769.

[Kesner and Howe, 2014] Kesner, S. and Howe, R. (2014). Robotic catheter cardiac ablation combining ultrasound guidance and force control. *The International Journal of Robotics Research*, 33(4):631–644.

[Khalil, 1978] Khalil, W. (1978). *Contribution à la commande automatique des manipulateurs avec l'aide d'un modèle mathématique des mécanismes*. Thèse d'etat, Université des Sciences et Techniques du Languedoc, Montpellier, France.

[Khalil and Dombre, 1999] Khalil, W. and Dombre, E. (1999). *Modélisation identification et commande des robots*. Hermes Science Publications, deuxième edition.

[Khatib, 1987] Khatib, O. (1987). A unified approach for motion and force control of robot manipulators: The operational space formulation. *IEEE Journal of Robotics and Automation*, 3(1):43–53.

[Khoshnam and Patel, 2014] Khoshnam, M. and Patel, R. (2014). Robotics-assisted catheter manipulation for improving cardiac ablation efficiency. In *Proc. of the IEEE Int. Conf. on Biomedical Robotics and Biomechatronics (BIOROB)*, pages 308–313, São Paulo, Brazil.

[Kitagawa et al., 2002] Kitagawa, M., Okamura, A., Bethea, B., Gott, V., and Baumgartner, W. (2002). Analysis of suture manipulation forces for teleoperation with force feedback. In *Proc. of the Int. Conf. on Medical Image Computing and Computer-Assisted Intervention (MICCAI)*, pages 155–162, Tokyo, Japan.

[Klesius et al., 2004] Klesius, A. A., Dzemali, O., Simon, A., Kleine, P., Abdel-Rahman, U., Herzog, C., Wimmer-Greinecker, G., and Moritz, A. (2004). Successful treatment of deep sternal infections following open heart surgery by bilateral pectoralis major flaps. *European Journal of Cardio-thoracic Surgery*, 25:218–223.

[Kwoh et al., 1988] Kwoh, Y. S., Hou, J., and Jonckheere, E. A. (1988). A robot with improved absolute positioning accuracy for ct guided stereotactic brain surgery. *IEEE Transactions on Biomedical Engineering*, 35(2):153–160.

[Lawrence, 1988] Lawrence, D. A. (1988). Impedance control stability properties in common implementations. In *Proc. of the IEEE Int. Conf. on Robotics and Automation*, pages 1185–1190, Philadelphia, USA.

[Lemma et al., 2005] Lemma, M., Mangini, A., Redaelli, A., and Acocella, F. (2005). Do cardiac stabilizers really stabilize? experimental quantitative analysis of mechanical stabilization. *Interactive CardioVascular and Thoracic Surgery*, 4:222–226.

[Liang et al., 2014] Liang, W., Gao, W., Chen, S., and Tan, K. K. (2014). Stabilization for an ear surgical device using force feedback and vision-based motion compensation. In *IEEE/ASME International Conference on Advanced Intelligent Mechatronics (AIM)*, pages 943–948, Besançon, France.

[Longman, 2000] Longman, R. W. (2000). Iterative learning control and repetitive control for engineering practice. *Internationnal Journal of Control*, 73(10):930–954.

[Maciejowski, 2002] Maciejowski, J. M. (2002). *Predictive control with constraints*. Prentice Hall.

[Mayer et al., 2007] Mayer, H., Nagy, I., Knoll, A., Braun, E., Bauernschmitt, R., and Lange, R. (2007). Haptic feedback in a telepresence system for endoscopic heart surgery. *Presence*, 16(5):459–470.

[Naik et al., 2003] Naik, M. J., Abu-Omar, Y., Alvi, A., Wright, N., Henderson, A., Channon, K., Forfar, J. C., and Taggart, D. P. (2003). Total arterial revascularisation as a primary strategy for coronary artery bypass grafting. *Postgraduate Medical Journal*, 79:43–48.

[Nakamura and Kishi, 2001] Nakamura, Y. and Kishi, K. (2001). Robotic stabilisation assisting cardiac surgery on beating hearts. *Minimally Invasive Therapy & Allied Technologies*, 10(4-5):205–208.

[Nakamura et al., 2001] Nakamura, Y., Kishi, K., and Kawakami, H. (2001). Heartbeat synchronization for robotic cardiac surgery. In *Proc. of the IEEE Int. Conf. on Robotics and Automation (ICRA)*, volume 2, pages 2014–2019, Seoul, Korea.

[Newman et al., 1991] Newman, M. F., Kirchner, J. L., Phillips-Bute, B., Gaver, V., Grocott, H., and Jones, R. H. (1991). Longitudinal assessment of neurocognitive function after coronary-artery bypass surgery. *The New England Journal of Medicine*, 344(6):395–402.

[Ogata, 2002] Ogata, K. (2002). *Modern Control Engineering*. Prentice Hall, 4 edition. (International Edition).

[Okamura, 2004] Okamura, A. M. (2004). Methods for haptic feedback in teleoperated robot-assisted surgery. *Ind Rob.*, 31(6):499–508.

[Patel et al., 2002] Patel, N. C., Deodhar, A. P., Grayson, A. D., Pullan, D. M., Keenan, D. J. M., Hasan, R., and Fabri, B. M. (2002). Neurological outcomes in coronary surgery : Independent effect of avoiding cardiopulmonary bypass. In *Annals of Thoracic Surgery*, volume 74, pages 400–406.

[Patronik, 2008] Patronik, N. (2008). *A Miniature Mobile Robot for Precise and Stable Access to the Beating Heart*. Phd thesis, The Robotics Institute Carnegie Mellon University, Pittsburgh, USA.

[Patronik et al., 2012] Patronik, N., Ota, T., Zenati, M. A., and Riviere, C. (2012). Synchronization of epicardial crawling robot with heartbeat and respiration for improved safety and efficiency of locomotion. *International Journal of Medical Robotics and Computer Assisted Surgery*, 8(1):97–106.

[Perdereau, 1991] Perdereau, V. (1991). *Contribution à la commande hybride force-position*. Thèse de doctorat, Université Pierre et Marie Curie, Paris, France.

[Pujas, 1995] Pujas, A. (1995). *étude de la robustesse de schéma de commande position/force pour robots à deux bras,*. Thèse de doctorat, Université Montpellier II, Montpellier, France.

[Raibert and Craig, 1981] Raibert, M. H. and Craig, J. J. (1981). Hybrid position/force control of manipulators. *Trans. of the ASME, J. of Dynamic Systems, Measurement and Control*, 103:163–133.

[Åström and Wittenmark, 1997] Åström, K. J. and Wittenmark, B. (1997). *Computer controlled systems: theory and design*. Prentice Hall, 2 edition.

[Richa et al., 2010] Richa, R., Bó, A. P. L., and Poignet, P. (2010). Beating heart motion prediction for robust visual tracking. In *Proceedings of IEEE Conference on Robotics and Automation (ICRA '10)*, pages 4579–4584, Anchorage, USA.

[Riviere et al., 2006] Riviere, C. N., Gangloff, J., and de Mathelin, M. (2006). Robotic compensation of biological motion to enhance surgical accuracy. *Proceedings of the IEEE*, 94(9):1705–1716.

[Ruszkowski et al., 2015] Ruszkowski, A., Mohareri, O., Lichtenstein, S., Cook, R., and Salcudean, S. (2015). On the feasibility of heart motion compensation on the *da Vinci* surgical robot for coronary artery bypass surgery: Implementation and user studies. In *Proc. of the IEEE Int. Conf. on Robotics and Automation (ICRA)*, pages 4432–4439, Seattle, WA.

[Salisbury, 1980] Salisbury, J. K. (1980). Active stiffness control of a manipulator in cartesian coordinates. In *Proc. of the IEEE Int. Conf. on Decision and Control*, pages 95–100, Albuquerque, Etats-Unis.

[Sauvée et al., 2007] Sauvée, M., Noce, A., Poignet, P., Triboulet, J., and Dombre, E. (2007). Three-dimensional heart motion estimation using endoscopic monocular vision system: From artificial landmarks to texture analysis. *Biomedical Signal Processing and Control*, 2(3):199–207.

[Sciavicco and Siciliano, 2002] Sciavicco, L. and Siciliano, B. (2002). *Modelling and control of robot manipulators*. Springer-Verlag, seconde edition.

[Shekar, 2006] Shekar, P. S. (2006). On-pump and off-pump coronary artery bypass grafting. *Circulation*, 113:51–52.

[Sousa and Cortesão, 2014] Sousa, C. D. and Cortesão, R. (2014). Physical feasibility of robot base inertial parameter identification: A linear matrix inequality approach. *The International Journal of Robotics Research*, 33(6):931–944.

[Swindle and Smith, 2008] Swindle, M. M. and Smith, A. C. (2008). Swine in biomedical research. In *Swine in Biomedical Research*, pages 233–239. Humana Press.

[Trejos et al., 1999] Trejos, A. L., Sulcudean, S. E., Sassani, F., and Lichtenstein, S. (1999). On the feasibility of a moving support for surgery on the beating heart. In *Proc. of the Second Int. Conf. on Medical Image Computing and Computer-Assisted Intervention (MICCAI)*, pages 1088–1097, London, UK. Springer-Verlag.

[Volpe and Khosla, 1995] Volpe, R. and Khosla, P. (1995). The equivalence of a second-order impedance control and proportionnal gain explicit force control. *The International Journal of Robotics Research*, 14(6):574–589.

[Whitney, 1985] Whitney, D. E. (1985). Historical perspective and state of the art in robot force control. In *Proc. of the IEEE Int. Conf. on Robotics and Automation*, pages 262–268, St Louis, USA.

[Whitney and Nevins, 1979] Whitney, D. E. and Nevins, J. L. (1979). What is the remote center compliance (rcc) and what can it do ? In *Proc. of the Int. Symp. on Industrial Robots*, pages 135–152, Washington, USA.

[WHO, 2009] WHO (2009). World health organization. `http://www.who.int/en/`.

[Yuen et al., 2010] Yuen, S. G., Perrin, D. P., Vasilyev, N. V., del Nido, P. J., and Howe, R. D. (2010). Force tracking with feed-forward motion estimation for beating heart surgery. *IEEE Transactions on Robotics*, 26(5):888–896.

[Yuen et al., 2009] Yuen, S. G., Yip, M. G., Vasilyev, N. V., Perrin, D. P., del Nido, P. J., and Howe, R. D. (2009). Robotic force stabilization for beating heart intracardiac surgery. In *Medical Image Computing and Computer-Assisted Intervention (MICCAI '09)*, volume 5761 of *Lecture Notes in Computer Science (LNCS)*, pages 26–33, London, UK. Springer.

[Zarrouk et al., 2013] Zarrouk, Z., Chemori, A., and Poignet, P. (2013). Force feedback control for compensation of physiological motions in beating heart surgery with real-time experiments. In *Systems and Control (ICSC), 2013 3rd International Conference on*, pages 956–961.